UMONS
Université de Mons

Faculté
des Sciences

Modeling of parity-time symmetry in photonic designs with multiple modes

Nicolas Rivolta

Thesis presented in fulfilment of the requirements for the degree of
Doctor of Sciences

Thesis supervisor
Bjorn MAES

University of Mons
Faculty of Sciences
Micro- and Nanophotonic Materials Group

Academic year
2016-2017

ISBN 978-2-87325-101-7

Supervisor

Prof. Bjorn Maes	University of Mons (MMNP)

Jury members

Prof. Henri Benisty	Institut d'Optique Graduate School (France)
Prof. Michel Voué	University of Mons (LPMO)
Prof. Nicolas Le Thomas	Ghent University (Belgium)
Dr. Branko Kolaric	University of Mons (MMNP)
Dr. Christophe Caucheteur	University of Mons (FPMs)

University of Mons
Faculty of Sciences

Micro- and Nanophotonic Materials Group (MMNP)
Place du Parc 20
7000 Mons
Belgium

Tel.: +32-65/37.33.85
http://www.umons.ac.be/nanophot

This thesis was carried out in the context of a doctoral fellowship from the Fonds National de Recherche Scientifique (FRS-FNRS) - Wallonia (Belgium)

Remerciements

Je tiens à remercier toutes les personnes qui ont contribuées scientifiquement ou humainement, de près ou de loin, au travail présenté dans cette thèse de doctorat.

Mes premiers remerciements vont à mon promoteur, le Prof. Bjorn Maes, pour m'avoir donné l'opportunité de réaliser une thèse dans son service. Tout au long de ces quatre années, il s'est montré particulièrement disponible et patient. Lors de nos nombreuses réunions, il m'a donné de précieux conseils et m'a permis d'être plus efficace dans mon travail. Il a aussi régulièrement relu mes écrits à l'orthographe parfois défaillante.

Je remercie ensuite les membres de mon comité d'accompagnement, Prof. Michel Voué et Dr. Christophe Caucheteur, pour leur temps et leur bienveillance, leur intérêt pour mon travail ainsi que pour leurs questions pertinentes.

Je ne saurais trop remercier le Prof. Henri Benisty, pour son accueil chaleureux lors de mon séjour scientifique à l'Institut d'Optique. Ces deux mois à Palaiseau ont élargi mes horizons scientifiques et ont été riches en rencontres humaines.

Je remercie également les doctorants/docteurs/chercheurs du bureau et surtout amis : Galaad Altares, Fabio Vaianella, Dr. Gilles Rosolen, Mathieu Stock et Corentin Guyot. Les belotes, lancés de balles, frites, anniversaires, montages photos, blagues, sifflements musicaux, ... m'ont donné du mal pour convaincre les personnes extérieures que le travail scientifique demandait de la rigueur et du sérieux.

Je remercie aussi toutes les autres personnes présentent dans le couloir pour la bonne ambiance qui y règne : Sabrina Devouge, Dr. Evelyne Daubie, Dr. Joseph Hanton, Dr. Georges Kohnen, Francis Lequeux, Dr. Branko Kolaric.

'last but not least', je remercie énormément mes parents sans qui rien ne serait possible. Je remercie ma moitié qui me supporte dans tous les sens du terme. Et je remercie ma famille, Chacalots, le BC Mons UTD (plezier), ainsi que toutes les autres personnes sans qui la vie serait bien triste.

Et merci à toi qui lis ces lignes !

Summary

Parity-Time ($\mathcal{PT}$) symmetry emerged in quantum mechanics as a weaker alternative to hermiticity, a condition to ensure Hamiltonians have real eigenvalues. The similarities between the equations of quantum mechanics and optics have naturally led to the latter becoming a testbed for this new paradigm. In practice in optics, $\mathcal{PT}$ symmetry is introduced by adding balanced gain and loss to the structure. One of the main interests of these devices is the existence of two phases ($\mathcal{PT}$-symmetric and broken) separated by exceptional points. Our goal was to exploit and control these characteristics and modes for novel photonic components.

In this thesis we demonstrate the switching capabilities of a $\mathcal{PT}$ symmetrical grating between its two diffraction orders. Furthermore, we discover a symmetry recovery phenomenon in a linear system. Usually the system only goes from the symmetric to the broken phase when gain and loss increases. However, by playing with the coupling constants in a multi-modal structure, a symmetric phase revival becomes possible. Next, we investigate the unidirectional invisibility phenomenon, leading to zero reflection from one side only. Originally introduced in Bragg gratings, we investigate a different structure with side-coupled resonators, and find that unidirectional invisibility can be broadband. Finally, we associate $\mathcal{PT}$ symmetry with topological features in a quasi-periodic structure. A rich mixing between the topological edge modes and band modes is uncovered, leading to the potential of laser resonance engineering.

Contents

1

Introduction

1.1 Introduction

Thanks to science and innovation, the world is moving faster than ever. Every month we witness the release of new technologies or devices: smartphones, autonomous cars, connected houses... All these innovations that make life easier or consumption more efficient rely on the existence of a giant and fast data network. The improvement of this communication network really started with the replacement of the old copper cables by optical fibers. Nowadays we continue this network upgrade with smaller and faster integrated devices.

For this purpose, over the past decades, photonics has been widely investigated. With an increasing control of materials down to the nanoscale, we try to tailor the flow of light over an increased path length for diverse functionalities. Apart from telecommunications and information processing, photonic applications are numerous: lighting, displays, solar cells, detectors, microscopy, lasers, spectroscopy etc. A major problem for routing applications is often the inherent loss of the materials. Thus, up to now, loss is an unwanted features and scientists try to avoid it as much as possible.

In this context, originating from fundamental studies in quantum mechanics, Parity-Time ($\mathcal{PT}$) symmetry is a new paradigm that can change our mindset. Instead of avoiding loss, it judiciously combines loss with gain [1] so that new and interesting properties emerge stemming from novel symmetries [2].

In 1998 Bender and Boettcher [3] introduced the concept of $\mathcal{PT}$ symmetry in quantum mechanics. To properly represent a physical system, an Hamiltonian must, among other things, possess real eigenvalues. Usually this condition is fulfilled due to the hermiticity of the operator. However, hermiticity is the only axiom used by quantum mechanics that is defined without any physical meaning.

The initial goal of the space-time reflection operator is to replace hermiticity and ensure real eigenvalues, while it provides a physical meaning. This leads to the construction of a new formalism for quantum mechanics. However, the $\mathcal{PT}$ symmetry operator ensures real eigenvalues only if it shares a common set of eigenvectors with the Hamiltonian. If not, the eigenvalues are not necessarily real. This property gives rise to the existence of two phases, the unbroken $\mathcal{PT}$ symmetry phase and the broken one, separated by so-called exceptional points.

A decade later [4], the similarity between the equations of quantum mechanics and optics allowed one to apply the concepts of $\mathcal{PT}$ symmetry towards optical devices [5]. Briefly, $\mathcal{PT}$ symmetry requires that the refractive index of the optical structures has an even real part and an odd imaginary part. The real part of the refractive index defines the guiding properties of the structure, while the imaginary part defines the amplification (gain) or absorption (loss) of light. An odd imaginary part signifies that the structure supports the same amount of gain and loss. Thus loss becomes a crucial element of the devices and not simply an unwanted feature [6]. In this context many optical devices have been revisited, trying to take advantage of the special features offered by $\mathcal{PT}$ symmetry [7]: the traditional directional coupler [8–13], switching devices [14, 15], plasmonic structures [16], Bragg reflectors with unidirectional invisibility [17–19], micro-ring resonators and microdisks with single-mode laser operation [20–23], gratings [24–29] and others [30–38].

One of the most salient properties of these structures is the spontaneous symmetry breaking at a certain loss/gain level, marking a clear transition via the exceptional point between the broken and unbroken $\mathcal{PT}$ phases with very different behaviours. All these new possibilities are obtained thanks to the presence of the inherent loss of the materials.

This thesis draws its inspiration from known 'passive' optical structures, which we adapt within the $\mathcal{PT}$ context. These problems are approached by rigorous theoretical and numerical calculations, and are further described by more intuitive semi-analytical approaches. In the following section we describe the various subjects addressed in this work.

1.2 Outline

This thesis is structured as follows. Chapter 2 is devoted to the basic description of $\mathcal{PT}$ symmetry. We first explain the origins of this paradigm from quantum mechanics and its ability to replace hermiticity. We briefly recall the properties of Hamiltonians and their requirement to possess real eigenvalues. The parity and time operators and their actions are presented. Then one of the principal interests of $\mathcal{PT}$ symmetry is discussed: a phase transition (or symmetry breaking) that induces the existence of different behaviours of the system. Subsequently, we introduce $\mathcal{PT}$ symmetry into optics and define a condition for the structure to be $\mathcal{PT}$-symmetric. A typical example is used to clearly expose the $\mathcal{PT}$ properties. Finally, various representative results from the literature are exposed to demonstrate the potential uses of $\mathcal{PT}$ symmetry and its capability to control the modes.

Chapter 3 addresses the background theoretical concepts relevant for the thesis. Starting from Maxwell's equations, we derive the Helmholtz equation to extract

the modes of light, we present boundary conditions and Fresnel coefficients. Then, cavities and their resonances are considered together with the mathematical tools to describe them: Fabry-Pérot cavities and coupled mode theory. We give an overview of the eigenmode expansion method that is used in the numerical simulation program CAMFR [39]. We introduce the scattering matrix and transfer matrix formalisms for the description of 1D single-mode structures. And finally, periodic structures and the Bloch theorem are addressed.

The switching capability by $\mathcal{PT}$ symmetry is one of the main promises in optics. Chapter 4 is devoted to the study of the diffraction and switching properties of a parity-time ($\mathcal{PT}$) symmetric transmission grating, and exposes the work published in [14]. This grating operates through a limited number of guiding modes and the resulting interference excites the various existing transmission orders. This interferometric operation is altered by the introduction of balanced gain and loss, leading to efficient switching around the spontaneous symmetry breaking point. Furthermore, we investigate the influence of the longitudinal reflections, which are not common in previously studied $\mathcal{PT}$ structures. In addition, we separately tailor the periodicities of gain and loss, so that the device remains $\mathcal{PT}$ symmetric. However, this gives a new way to control the mode merging phenomenon, as we obtain interactions between previously distinct modes.

Chapter 5 is focused on the broken and unbroken $\mathcal{PT}$ phases and the exceptional points, this work is published in [8]. The Typical $\mathcal{PT}$-symmetric structures switch from the unbroken to the broken phase when gain/loss increases through an exceptional point. In contrast, we demonstrate a system with the unusual, reverse behaviour, where the symmetric phase is recovered after a broken phase. We study this phenomenon analytically and numerically in the simplest possible system, consisting of four coupled modes, and we present potential dielectric and plasmonic implementations. The complex mode merging scheme, with two distinct unbroken $\mathcal{PT}$ phases encompassing a broken one, appears for a specific proportion range of the coupling constants. This regime with 'inverse' exceptional points is interesting for the design of novel $\mathcal{PT}$ devices.

Typical one-dimensional $\mathcal{PT}$ structures exhibit unidirectional invisibility (also called anisotropic transmission resonances), meaning unity-transmission and zero-reflection for incidence from one direction. In Chapter 6 we expose the work published in [40]: an analysis of the scattering properties of a $\mathcal{PT}$-symmetric structure made of a waveguide and a finite chain of side-coupled resonators. The side-coupled nature of this structure provides unidirectional invisibility as well, but with different characteristics than the traditional tight-binding chain. We explore these properties in detail with numerical and analytical approaches for various chain lengths and geometries. As an interesting feature, we can achieve a broadband unidirectional invisibility with only two resonators. Furthermore, we observe rich dispersions for these anisotropic transmission resonances with four resonators, which can be carefully tuned.

Finally Chapter 7 mixes topology and $\mathcal{PT}$ symmetry features in a 1D photonic quasi-crystal. Via the scattering characteristics we analyze various properties of a particular mirrored structure, which supports topological edge modes in its bandgaps. These interface modes display a non-trivial dependence on the quasi-periodic geometry, even in a passive system. Subsequently, the tailored addition

of gain and loss generates curious $\mathcal{PT}$-like features. The quasi-crystal high density of modes leads to complicated mode-merging behaviours between edge and band modes, such as the symmetry recovery phenomenon. Furthermore, unidirectional invisibility is also present, but it displays richer patterns in comparison to previously studied periodic structures. Additionally, we examine lasing effects in detail, with numerics and a simple Fabry-Perot model. The large variety of mode-merging behaviours opens the way to laser resonance engineering.

1.3 Publications

1.3.1 Publications in international journals

Here follow the contributions published in international journals during the PhD work:

- **N. Rivolta** and B. Maes, Angle-specific transparent conducting electrodes with metallic gratings, *Journal of Applied Physics*, vol. 116, p. 053101, 2014
- **N. Rivolta** and B. Maes, Diffractive switching by interference in a tailored PT-symmetric grating, *Journal of Optical Society of America B*, vol. 32, pp. 1330-1337, 2015
- **N. Rivolta** and B. Maes, Symmetry recovery for coupled photonic modes with transversal PT symmetry, *Optics Letters*, vol. 40, pp. 3922-3925, 2015
- **N. Rivolta** and B. Maes, Side-coupled resonators with parity-time symmetry for broadband unidirectional invisibility, *Physical Review A*, vol. 94, p. 053854, 2016
- **N. Rivolta**, H. Benisty and B. Maes, Topological edge modes with PT symmetry in a quasi-periodic structure, *Physical Review A*, vol. 96, p. 023864, 2017

1.3.2 Contributions in international conferences

A list of our conference talks / proceedings contributions:

- N. Rivolta and B. Maes, *Angle-specific transparent electrodes*, Nanolight 2014, Benasque, Spain, 2014
- N. Rivolta and B. Maes, *Shaping sub-wavelength plasmonic funnels*, Annual symposium of the IEEE Photonics Society Benelux Chapter, Eindhoven, Netherlands, 2013
- N. Rivolta and B. Maes, *Switching of free space diffraction with a tailored PT symmetric grating*, Annual symposium of the IEEE Photonics Society Benelux Chapter, Twente, Netherlands, 2014

- N. Rivolta and B. Maes, *Diffraction properties of a tailored parity-time (PT) symmetric grating*, OWTNM XXIII (Optical Wave and waveguide Theory and Numerical Modelling), London, United Kingdom, 2015

- N. Rivolta and B. Maes, *Switching of free space diffraction with a tailored PT symmetric grating*, International School of Atomic and Molecular spectroscopy (nano-optics : principles enabling basic research and applications), Erice, Italy, 2015

- N. Rivolta and B. Maes, *Side-coupled resonators with parity-time symmetry for broadband unidirectional invisibility*, Meta'16 - 7th International Conference on Metamaterials, Photonic Crystals and Plasmonics, Malaga, Spain, 2016

- N. Rivolta and B. Maes, *Side-coupled resonators with parity-time symmetry for broadband unidirectional invisibility*, Annual symposium of the IEEE Photonics Society Benelux Chapter, Ghent, Belgium, 2016

- N. Rivolta, H. Benisty and B. Maes, *$\mathcal{PT}$ symmetry in a quasi-periodic structure with topological edge modes*, 11^{th} International Congress on Engineered Material Platforms for Novel Wave Phenomena - Metamaterials'2017, Marseille, France, 2017

1.3.3 Award

- Best oral presentation, N. Rivolta, *Diffraction properties of a tailored parity-time (PT) symmetric grating*, OWTNM XXIII (Optical Wave and waveguide Theory and Numerical Modelling), London, United Kingdom, 2015

2

$\mathcal{PT}$ symmetry

In this chapter we introduce the concept of $\mathcal{PT}$ symmetry. Sec. 2.1 exposes the theoretical origins of this concept in quantum mechanics and one of its major properties: the existence of an unbroken and a broken $\mathcal{PT}$-symmetric phase. Afterwards, an introduction of this new paradigm in optics is provided in Sec. 2.2, which is followed by several interesting effects for photonic applications.

2.1 $\mathcal{PT}$ symmetry in quantum mechanics

The theory of quantum mechanics is nearly a century old. Well established by experiments and predictions, it has now been accepted as a reliable part of modern science. The foundations of this theory rely on several fundamental axioms [41]. Many of these axioms follow from physical requirements of a quantum system: the energy spectrum must be real, the time evolution must be unitary, etc... One axiom stands beside the others due to its mathematical requirement. It specifies that the Hamiltonian H, the operator expressing the dynamics of the quantum system, must be Hermitian:

$$H = H^{\dagger} \tag{2.1}$$

where † stands for the Dirac Hermitian conjugate. This conjugation is the combination of matrix transposition and complex conjugation, and it is difficult to find a physical meaning into these mathematical operations. However, Hermicity is very convenient because it ensures that the eigenvalues of H are real and that the time-evolution operator is unitary.

Hermitian Hamiltonians are the consequence of a paradigm in which all the processes are reversible in time, and time is considered as just another dimension

[42]. At the beginning of the last century, this view was almost unanimously accepted. But the idea of irreversible processes already emerged in the 19th century with the introduction of the second law of thermodynamics, the law of increase of entropy. Time-oriented processes and their descriptions opened the way to non-Hermitian quantum mechanics.

Non-Hermitian Hamiltonians were traditionally used to describe dissipative or irreversible processes, such as transport in fluids [43, 44] or radioactive decay. The probability to find the particle decreases in time, and the Hamiltonian does not respect unitarity. Therefore, these Hamiltonians are only approximations, as the particle does not really vanish but transforms into another particle. Thus, these Hamiltonians cannot be regarded as fundamental.

In 1998, Bender and Boettcher [3] made a breakthrough in quantum mechanics, affirming that non-Hermitian but parity-time ($\mathcal{PT}$) symmetric Hamiltonians ensure a real energy spectrum and unitarity. Thus non-Hermitian Hamiltonians can properly describe quantum systems. The sufficient but not necessary mathematical condition of Hermiticity is here replaced by a weaker, physically transparent condition: space-time reflection, or $\mathcal{PT}$ symmetry. A weaker condition induces that the range of acceptable Hamiltonians or systems is opened wider, and one could access unknown phenomenona. However, the eigenstates of such an Hamiltonian are not always orthogonal, and constructing a self-consistent quantum mechanical theory based on such Hamiltonians requires redefining the scalar product and norm. This construction is outside the scope of this work but can be found with the full treatment of non-Hermitian Hamiltonians in [45].

In this section we briefly remind the role of the Hamiltonian in quantum mechanics (Sec. 2.1.1), we present the parity and time operators (Sec. 2.1.2), and we study when the eigenvalues of a $\mathcal{PT}$ Hamiltonian are real or not (Sec. 2.1.3).

2.1.1 Hamiltonian and quantum theory

The Hamiltonian operator defines a quantum system physically in three important ways.

Firstly, the Hamiltonian defines the energy levels E of the eigenstates ψ of the system. These energy levels are given by the time-independent Schrödinger eigenvalue problem:

$$H\psi = E\psi \tag{2.2}$$

Usually this equation takes the form of a differential equation that must be solved with boundary conditions for ψ. A quantum system is physically acceptable if the energy values of its Hamiltonian are real and bounded below.

Secondly, the Hamiltonian defines the evolution in time of the states and operators of a quantum theory. The time dependence of a state $\psi(t)$ is given by the time-dependent Schrödinger equation:

$$i\hbar\frac{\partial}{\partial t}\psi(t) = H\psi(t) \tag{2.3}$$

If H is time-independent, the solution of this differential equation is:

$$\psi(t) = e^{-i\hbar Ht}\psi(0) \tag{2.4}$$

with the time evolution operator $e^{-i\hbar Ht}$. If we inject (2.2) in (2.3), the modulus of ψ is conserved in time for any real E. In conventional quantum mechanics, the time evolution is unitary because H is Hermitian. As a result, the norm of the state $\psi(t)$ remains constant in time. As the norm squared of a state is equivalent to the probability to observe this state, it is logical that the norm must remain constant as that probability cannot grow or decay in time. $\mathcal{PT}$ symmetric Hamiltonians are not necessary Hermitian, but the norm/probability of the states are still time independent, if its eigenvalues are real.

Finally, the Hamiltonian gives a general scope of the symmetries of the system. As an example, if H commutes with a linear operator, then the eigenstates of H are also eigenstates of this operator [46]. If this linear operator defines a symmetry, its eigenstates possess this symmetry and thus also the eigenstates of H. Though a general state of H is a linear combination of the eigenstates of H and thus not necessarily possesses their symmetries.

2.1.2 $\mathcal{P}$ and $\mathcal{T}$ operators

The space-reflection operator or parity operator is denoted $\mathcal{P}$. In the quantum-mechanical point of view, it changes the sign of the coordinate operator $\hat{x}$ and the momentum operator $\hat{p}$:

$$\begin{aligned} \mathcal{P}\hat{x}\mathcal{P} &= -\hat{x} \\ \mathcal{P}\hat{p}\mathcal{P} &= -\hat{p} \end{aligned} \tag{2.5}$$

A system is called $\mathcal{P}$ invariant if its Hamiltonian is not affected by $\mathcal{P}$ i.e. it commutes with $\mathcal{P}$. We note that $\mathcal{P}$ leaves invariant the fundamental commutation relation of quantum mechanics:

$$\hat{x}\hat{p} - \hat{p}\hat{x} = i\hbar\mathbf{1} = \mathcal{P}(\hat{x}\hat{p} - \hat{p}\hat{x}) \tag{2.6}$$

with $\mathbf{1}$ the identity operator. This property defines $\mathcal{P}$ as a linear (or unitary) operator. The linearity of an operator ensures that the eigenstates of an Hamiltonian, which is invariant under this operator, present the symmetry specified by this operator [46].

The time reversal operator $\mathcal{T}$ changes the sign of $\hat{p}$, but does not affect $\hat{x}$:

$$\begin{aligned} \mathcal{T}\hat{x}\mathcal{T} &= \hat{x} \\ \mathcal{T}\hat{p}\mathcal{T} &= -\hat{p} \end{aligned} \tag{2.7}$$

Opposite to $\mathcal{P}$, $\mathcal{T}$ does not leave the commutation relation invariant, except if $\mathcal{T}$ is chosen to be antilinear (or antinuitary) i.e.:

$$\mathcal{T}i\mathcal{T} = -i \tag{2.8}$$

In mathematics, an antilinear or antiunitary operator U is a bijective mapping of a complex Hilbert space such that $\langle Ux, Uy\rangle = \langle x^*, y^*\rangle$ for all x, y in the Hilbert space and where * stands for the complex conjugation and $\langle ., .\rangle$ stands for the scalar product.

$\mathcal{P}$ and $\mathcal{T}$ are reflection operators, so a double application of one of them must be equivalent to unity:

$$\mathcal{P}^2 = \mathcal{T}^2 = \mathbf{1} \tag{2.9}$$

Finally $\mathcal{P}$ and $\mathcal{T}$ commute with one another:

$$\mathcal{PT} - \mathcal{TP} = 0 \tag{2.10}$$

A system is $\mathcal{PT}$ invariant if its Hamiltonian H commutes with the operator $(\mathcal{PT})$:

$$H = H^{\mathcal{PT}} = (\mathcal{PT})H(\mathcal{PT}) \tag{2.11}$$

where we use the commutation relation of $\mathcal{P}$ and $\mathcal{T}$ and with $H^{\mathcal{PT}}$ the space-time reflected Hamiltonian.

2.1.3 Broken and unbroken $\mathcal{PT}$ symmetry

A $\mathcal{PT}$ symmetric Hamiltonians H commutes with $\mathcal{PT}$. But as $\mathcal{PT}$ is not linear, the eigenstates of H are not necessarily eigenstates of $\mathcal{PT}$.

What happens if we impose ψ to be an eigenstate for both $\mathcal{PT}$ and H? With λ the eigenvalue, the eigenvalue condition for $\mathcal{PT}$ can be expressed as:

$$\mathcal{PT}\psi = \lambda\psi \tag{2.12}$$

If we multiply by $\mathcal{PT}$ on the left and with $(\mathcal{PT})^2 = \mathbf{1}$ (see (2.9)), we obtain:

$$\psi = (\mathcal{PT})\lambda(\mathcal{PT})^2\psi \tag{2.13}$$

As $\mathcal{T}$ is antilinear (2.8), we have $(\mathcal{PT})\lambda(\mathcal{PT}) = \lambda^*$ and we can write:

$$\psi = \lambda^*\lambda\psi = |\lambda|^2\psi \tag{2.14}$$

So $|\lambda|^2 = 1$ and λ can be expressed as a phase:

$$\lambda = e^{i\alpha} \tag{2.15}$$

Now if we multiply the eigenvalue equation (2.2) by $\mathcal{PT}$ on the left and again use $(\mathcal{PT})^2 = 1$, we have:

$$(\mathcal{PT})H\psi = (\mathcal{PT})E(\mathcal{PT})^2\psi \tag{2.16}$$

With (2.12) and the fact that H commutes with $\mathcal{PT}$, we deduce:

$$H\lambda\psi = (\mathcal{PT})E(\mathcal{PT})\lambda\psi \tag{2.17}$$

Then we use again the fact that $\mathcal{T}$ is antilinear:

$$E\lambda\psi = E^*\lambda\psi \tag{2.18}$$

Since $\lambda \neq 0$ we can conclude that $E = E^*$ and thus E is real.

This conclusion is very powerful. If every eigenstate of H is also an eigenstate of $\mathcal{PT}$, then their eigenvalues are real and we say that the $\mathcal{PT}$ symmetry of H is unbroken. Conversely, if some eigenstates of H are not eigenstates of $\mathcal{PT}$, then their eigenvalues are not necessarily real and we say that the $\mathcal{PT}$ symmetry of H is broken.

By tuning some parameters of H, we can go from one phase to the other. This phase transition between unbroken and broken phases is the origin of high hopes for discoveries in many fields. Obviously, if a system undergoes a phase transition from real eigenvalues to complex ones, the behaviour of the system changes drastically.

Most of the time in this work we will use a perturbative approach. We start from a Hermitian Hamiltonian that describes a well known system, and then we add a $\mathcal{PT}$ symmetric but non-Hermitian component tuned by a single parameter. The phase transition will generally occur when we increase this single parameter.

2.2 $\mathcal{PT}$ symmetry in optics

In this section we make the link between $\mathcal{PT}$ symmetry in quantum mechanics and in optics (Sec. 2.2.1). We apply this concept to a simple optical structure (Sec. 2.2.2), before exposing several interesting effects brought by $\mathcal{PT}$ symmetry (Sec. 2.2.3). The full understanding of this section relies on a basic knowledges of optics. The reader can find an introduction to these concepts in Chap. 3.

2.2.1 Link to optics

The Hamiltonian H of a particle with a mass m within a position dependent potential $V(\hat{r})$ is given by:

$$H = \frac{\hat{p}^2}{2m} + V(\hat{r}) \tag{2.19}$$

For H to be Hermitian it has to be invariant under complex conjugation. $\hat{p}^2$ is intrinsically invariant, but the potential has to satisfy $V(\hat{r}) = V^*(\hat{r})$. This implies that $V(\hat{r})$ can only be real for this Hamiltonian H to be Hermitian.

For $\mathcal{PT}$ symmetry instead of Hermiticity, similarly, the impulsion part is intrinsically invariant through the $\mathcal{PT}$ operation. But the potential has to satisfy the condition:

$$V(\hat{r}) = V^*(-\hat{r}) \tag{2.20}$$

The real part of the potential must be symmetric with respect to the symmetry defined by $\mathcal{P}$. The complex part of the potential can be different from zero, but must be antisymmetric with respect to $\mathcal{P}$.

In order to inject this potential into the time independent Schrödinger equation, we interpret the $\hat{p}$ and $\hat{r}$ operators into the position representation. In this representation, the position vector $\mathbf{r}$ is $\hat{r}\psi = \mathbf{r}\psi$. With the commutation relation between $\hat{r}$ and $\hat{p}$ one deduces that the impulsion operator is $\hat{p} = -i\hbar\nabla$. So if we inject the Hamiltonian H in the time independent Schrödinger equation in the

position representation, one finds:

$$\Delta\psi - \frac{2m(V(\mathbf{r}) - E)}{\hbar^2}\psi = 0 \tag{2.21}$$

The latter equation is similar to the stationary Helmholtz equation (see Chap. 3.1.2):

$$\Delta\mathbf{E}(\mathbf{r}) + \left(\frac{\omega}{c}\right)^2 \varepsilon(\mathbf{r})\mathbf{E}(\mathbf{r}) = 0 \tag{2.22}$$

with $\mathbf{E}(\mathbf{r})$ the electric field in this case. The similarity between the two equations has conducted optics to become the testbed of $\mathcal{PT}$ symmetry.

What we have deduced for the potential $V(\mathbf{r})$ is still valid for the optical potential i.e. the permittivity $\varepsilon(\mathbf{r})$. It must satisfy the same conditions (2.20):

$$\begin{aligned} \Re(\varepsilon(\mathbf{r})) &= \Re(\varepsilon(-\mathbf{r})) \\ \Im(\varepsilon(\mathbf{r})) &= -\Im(\varepsilon(-\mathbf{r})) \end{aligned} \tag{2.23}$$

The real part of the refractive index defines the geometry or the guidance properties. This part must be symmetric so the structures we study must possess a symmetry defined by $\mathcal{P}$. The imaginary part of the refractive index represents the gain or loss in the structure. As it must be antisymmetric, one part of the structure will experience gain and the other loss.

We stress that the symmetry is defined by $\mathcal{P}$. This symmetry is not necessarily point inversion, but it can also be reflection with respect to a mirror plane. Finally, these conditions can also be described with the refractive index instead of the permittivity as $\varepsilon(\mathbf{r}) = n^2(\mathbf{r})$.

2.2.2 Exemple of $\mathcal{PT}$-symmetric optical structure

To introduce the $\mathcal{PT}$ concepts in optics, we study a simple well-known optical structure, where we add $\mathcal{PT}$ symmetry. The directional coupler is a perfect structure to experiment with $\mathcal{PT}$ symmetry. It consists of two single-mode waveguides that couple with one another. To make it $\mathcal{PT}$ symmetrical, we must satisfy the condition (2.23) for the real part of the refractive index $\Re(n(x, y, z)) = n_r(x, y, z)$, which implies that the two guides must be identical ($n_r(x, y, z) = n_r(-x, y, z)$), if we take a mirror symmetry plane yz situated between the waveguides as sketched in Fig. 2.1. For the condition (2.23) concerning the imaginary part $\Im(n(x, y, z)) = n_i(x, y, z)$, one of the waveguides must experience gain when the other experiences the exact same amount of loss ($n_i(x, y, z) = -n_i(-x, y, z)$). Note that the passive system ($n_i(x, y, z) = 0$) is Hermitian and $\mathcal{PT}$ symmetrical, but when $n_i(x, y, z) \neq 0$ it only remains $\mathcal{PT}$ symmetrical.

The specific nature of the waveguides does not matter. We note for the unperturbed propagation constant of the single mode $\beta = n_e k_0$ (so without coupling and without gain/loss), with n_e the effective index, $k_0 = 2\pi/\lambda_0$, and λ_0 the vacuum wavelength. The injection of gain (positive imaginary part of the refractive index, see Chap. 3) or loss (negative imaginary part of the refractive index) inside the waveguides leads to a modal effective gain/loss parameter γ, and this leads to an imaginary part of the effective index $n_e \pm \gamma i$. γ is the gain/loss factor and tunes

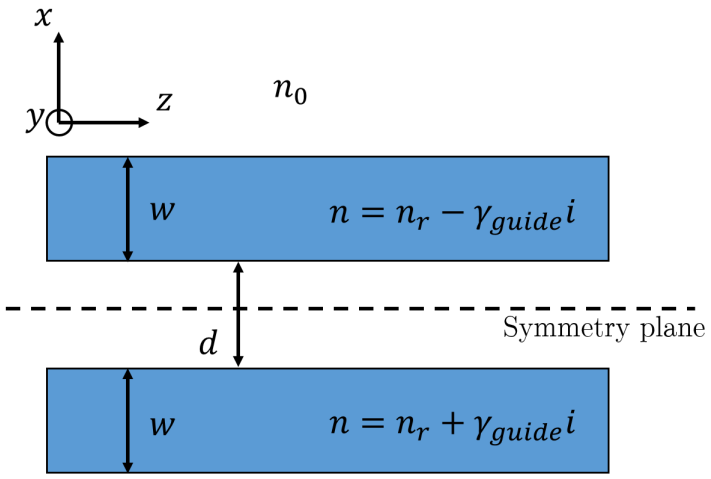

Figure 2.1: Schema of the directional coupler. Waveguides are infinite in z-direction.

the $\mathcal{PT}$ symmetrical part of our system. The coupling constant between the two waveguides κ depends on the distance d between the two waveguides, and can be obtained by overlap integrals of the field profiles of the unperturbed modes [47].

Such a symmetric and reciprocal system can be described by:

$$\frac{i}{k_0}\frac{d}{dz}\begin{pmatrix} c_1 \\ c_2 \end{pmatrix} = \begin{pmatrix} n_e - i\gamma & \kappa \\ \kappa & n_e + i\gamma \end{pmatrix}\begin{pmatrix} c_1 \\ c_2 \end{pmatrix} \tag{2.24}$$

with c_i the amplitude of the unperturbed mode in the ith waveguide. The coupling constant is determined via the lossless case. The coupling between the unperturbed modes of each waveguide mixes them and gives rise to two supermodes distributed across the whole structure. The matrix eigenvalues of (2.24) lead to the effective indices n_{coupled} of these two supermodes, with the analytical form:

$$n_{\text{coupled},1/2} = n_e \pm \sqrt{\kappa^2 - \gamma^2} \tag{2.25}$$

First, in the passive case when $\gamma = 0$, the effective indices of the two supermodes are real and on either side of n_e, their spacing is tuned by the coupling κ. The closer the waveguides get, the higher the coupling constant κ is, the more the supermodes deviate from the unperturbed modes.

Then, when the modal gain/loss factor γ increases from zero, this deviation tends to decrease. The effective indices of the two supermodes get closer, but are still purely real, we are in the unbroken $\mathcal{PT}$ symmetry phase. The boundary of this zone is $\gamma = \kappa$. This point is the exceptional point (or square root bifurcation) where the two eigenvalues are real and equal/degenerate. Then when $\gamma > \kappa$, we enter in the broken $\mathcal{PT}$ symmetric phase, where the eigenvalues become complex conjugates. The complex nature of the effective indices of the two supermodes indicates that one mode is amplified, while the other is absorbed during their propagation along z.

To illustrate, we calculate a real structure via numerical simulation (Camfr). We use two slab waveguides with a width w of 600 nm, a spacing d of 100 nm (see Fig. 2.1) and an excitation of $\lambda_0 = 1\mu$m. The cladding refractive index n_0 is equal

to 1 and the real part of the refractive index inside the waveguides is $n_r = 2$. The imaginary part of the refractive index inside the waveguides is $n_i = \pm\gamma_{\text{guide}}$ with the gain/loss factor γ_{guide}, leading to the modal gain/loss factor γ.

The numerical values of the effective indices of the two supermodes (Fig. 2.2) confirm the theoretical predictions. We begin at $\gamma_{\text{guide}} = 0$ with two different real values of the effective indices. Then when γ_{guide} increases, they remain real and approach each other until $\gamma_{\text{guide}} \approx 0.016$. At this exceptional point the effective indices are equal and degenerate. Beyond this point, they become complex conjugates in the broken zone.

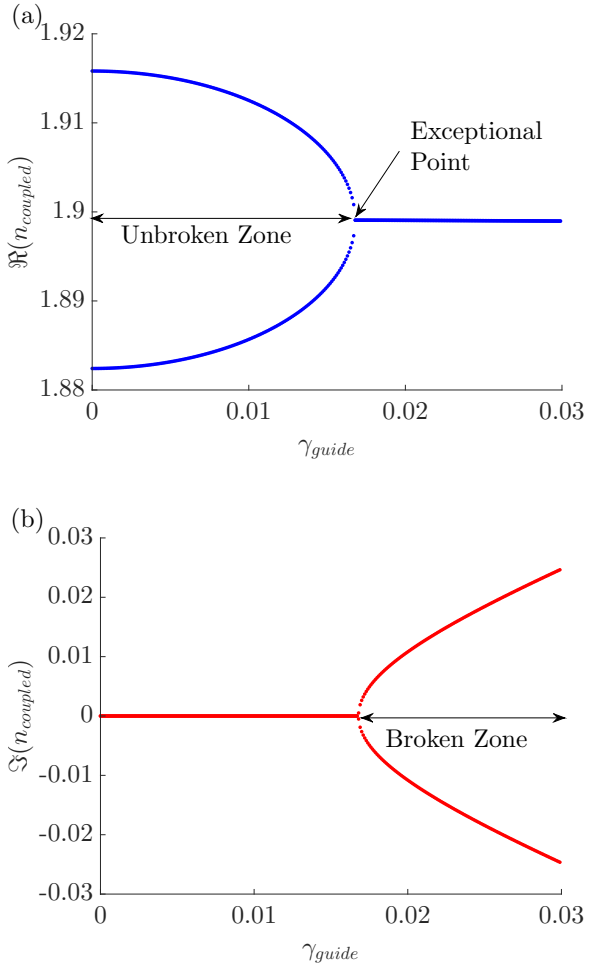

Figure 2.2: Evolution of the real (a) and imaginary (b) part of the effective indices of the two supermodes n_{coupled} as a function of the gain/loss factor γ_{guide}. We observe the exceptional point around $n_{\text{coupled}} \approx 0.016$ where one transits from the unbroken to the broken zone.

It is very enlightening to examine the field profiles of the two supermodes (Fig. 2.3). In the passive case (Fig. 2.3(a)), the profiles are symmetric or antisymmetric compared to the symmetry plane. These profiles are orthogonal to each other. When $\gamma_{\text{guide}} \neq 0$, but still in the unbroken zone, these profiles are slightly distorted (Fig. 2.3(b)) and they keep their orthogonality and symmetry. These two supermodes are equally present in the gain and in the lossy waveguide, leading to

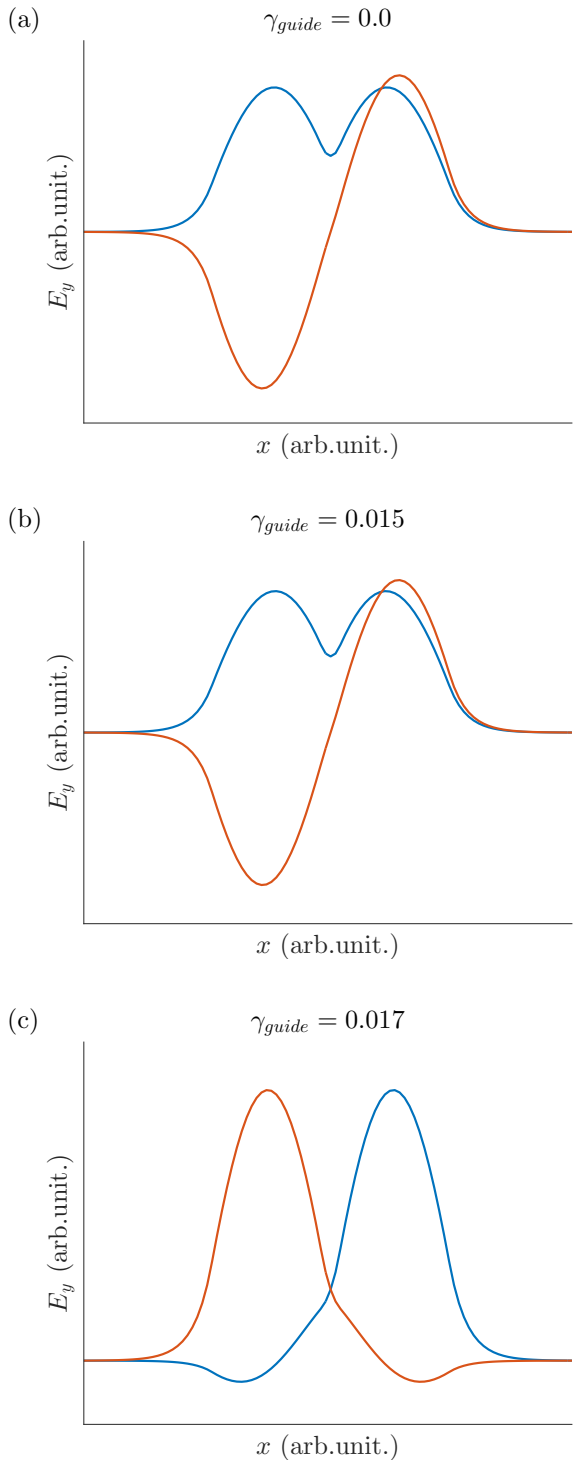

Figure 2.3: Field profiles of the two supermodes (orange and blue) in the passive case with $\gamma_{\text{guide}} = 0$ (a), in the $\mathcal{PT}$ symmetric phase with $\gamma_{\text{guide}} = 0.15$ (b) and just at the beginning of the broken zone with $\gamma_{\text{guide}} = 0.17$ (c). The initially symmetric or anti-symmetric profiles lose their symmetry and become mirror images from one another.

a cancellation of the amplification with the absorption. This explains why they

keep real effective indices even in the presence of gain or loss. Then, just after the exceptionnal point around $\gamma_{\text{guide}} \approx 0.016$, the profiles change completely (Fig. 2.3(c)). They are centered in one of the waveguides with only a small part in the other waveguide. The mode centered in the gain waveguide experiences gain, while the other is centered in the lossy waveguide and experiences loss. However, these profiles are symmetric with respect to one another, and so they are equally distributed concerning the real part of the refractive index. This explains why the effective indices of the associated supermodes have the same real part. Therefore the previous explains why the effective indices are complex conjugates. All these conclusions can be retrieved via the eigenvectors of the matrix (2.24), as they represent the distribution of the two supermodes over the waveguides.

$\mathcal{PT}$ symmetry allows for a modulation of the propagation constants that can be useful to transform our coupled waveguides in a simple switching structure. If we excite only the unperturbed mode of the upper waveguide (a combination of the two supermodes), this excitation will slowly flow to the other waveguide during its propagation along z. One defines the coupling length, the distance to have a total power exchange between the two waveguides, as $L_c = \frac{\pi}{k_0 \Re(n_{\text{coupled},1} - n_{coupled,2})}$. If our structure length is two times L_c, the output is the initial waveguide input (Fig. 2.4(a)). The coupling length is inversely proportional to the difference between the two propagation constants. Therefore, by increasing the gain/loss factor γ, this difference decreases and so the coupling length increases. So we can double this coupling length via the gain/loss factor and we can switch the output waveguide of our signal (see Fig. 2.4(b)). Note that we do not even have to reach the exceptional point and the broken $\mathcal{PT}$ symmetry zone for this switching application.

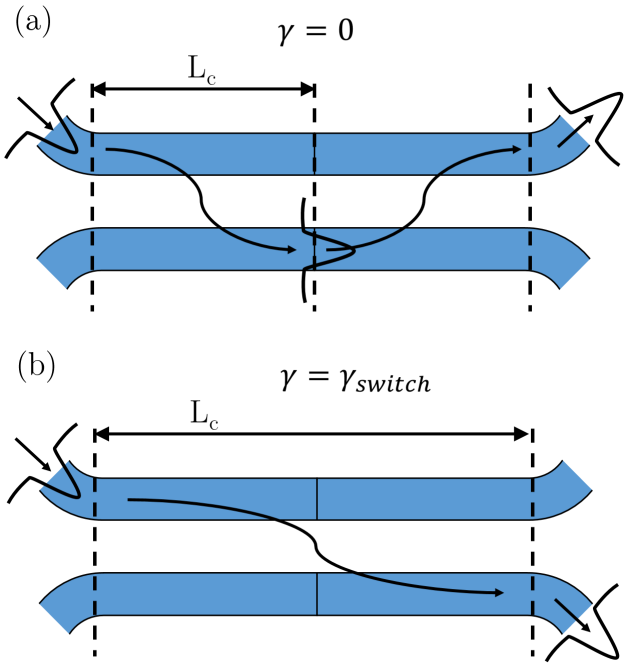

Figure 2.4: Design of a switching structure where the power stays in the original waveguide in the passive case (a) and switches to the other waveguide as the coupling length L_c is doubled due to the right choice of gain/factor.

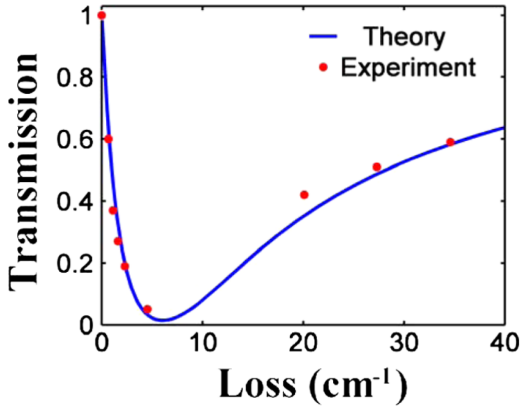

Figure 2.5: Transmission as function of the amount of loss present in one arm of a directional coupler (figure from [7]). The transmission decreases as the loss increases until the exceptional point.

2.2.3 State of the art

We shortly present in this subsection some counter intuitive or interesting effects brought by $\mathcal{PT}$ symmetry in photonics, without being exhaustive. For a more extensive review , we refer the reader to [48].

Loss induced transmission

A perfect gain and loss balance is difficult to reach. However, one of the advantages of $\mathcal{PT}$ symmetry is that some effects remain valid for the passive case with only loss. For example, we examine the transmission of a directional coupler with only loss in one of the waveguides (Fig. 2.5). As we can expect, at the beginning the transmission decreases as the loss increases. Surprisingly, at some point (around Loss equal to 6 cm^{-1}) the transmission reverses the trend and starts to increase as the loss still increases.

This unexpected behaviour can be understood via the analysis of the eigenmodes of the structure (Fig. 2.6). As we are not in a perfect $\mathcal{PT}$-symmetric case, our modes do not encounter a true exceptional point. Instead they encounter a 'pseudo' exceptional point, before which all supermodes of the structures are almost equally present in the two waveguides, leading to an absorption of power during the propagation. In contrast, beyond this 'pseudo' exceptional point, one of the supermodes is almost only present in the non-lossy waveguide. This less damped supermode leads to an increase of the transmission, while the other (situated in the lossy waveguide) is absorbed.

Single-mode lasing

Microring resonators are an important class of integrated structures that can be used to create laser resonances. Such structures support whispering gallery modes (WGMs) [49] with high quality factors and small footprint making them good candidates for on-chip integrated photonic components. However, a major drawback of this arrangement is that they support many modes closely spaced in frequency

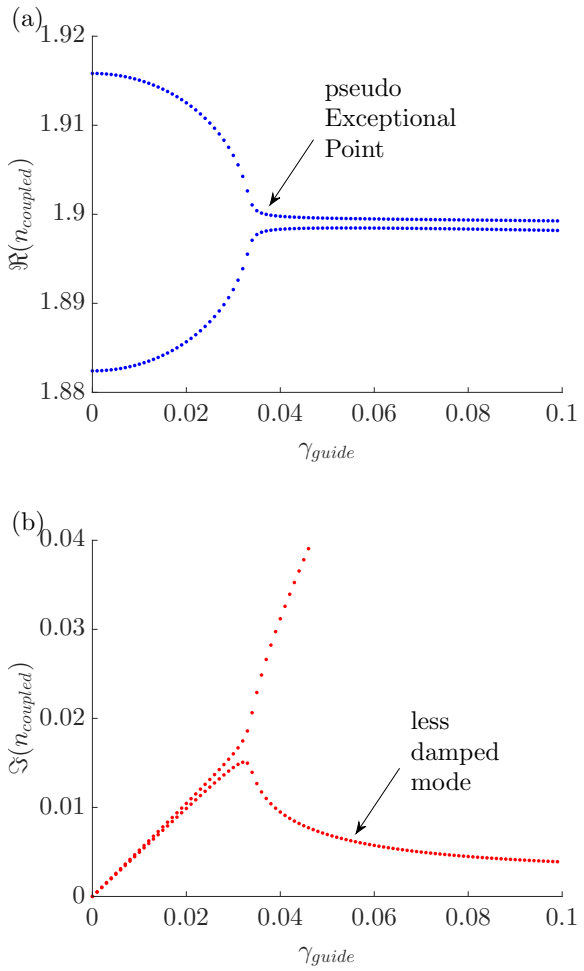

Figure 2.6: Evolution of the real (a) and imaginary (b) part of the effective indices of the two supermodes n_{coupled} as a function of the loss present in only one waveguide γ_{guide}. We observe a 'pseudo' exceptional point around $n_{\text{coupled}} \approx 0.035$ whereafter the real parts of the eigenmodes become close, but not equal, and the imaginary parts split.

with different azimuthal order. All the competing modes in the gain bandwidth can create laser resonances. This inherently multi-modal operation is detrimental to the spatial and temporal stability of the emitted radiation. Thus, mode selection strategies are implemented to achieve the desired single-mode operation. It turns out that $\mathcal{PT}$ symmetry can be useful for this selection due to mode control. We present here two different $\mathcal{PT}$-techniques, which depend on the gain/loss pattern, to achieve single-mode operation.

A first possibility is to add an alternation of gain and loss in the longitudinal direction of the microring structure [20]. The absence of modulation of the real part of the refractive index in the longitudinal direction induces a continuous rotational symmetry in the passive case. This symmetry implies that, for each azimuthal order, there are two modes that are degenerate in frequency. Adding gain and loss with a certain azimuthal order will break this degeneracy (in the complex plane) of the two modes with the same order. One is more present in the

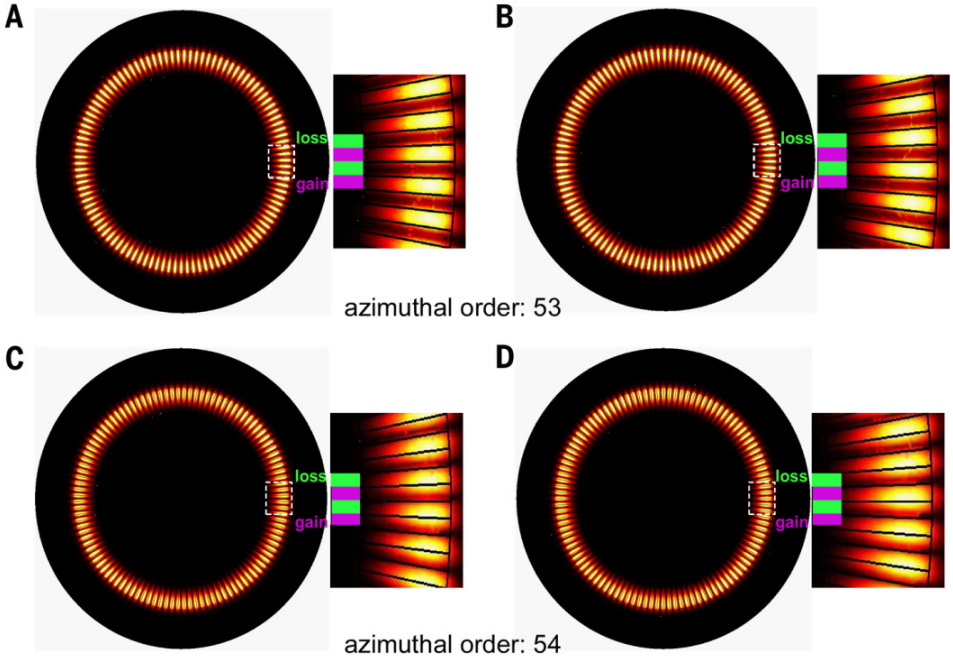

Figure 2.7: Electric field intensity of two WGMs with the same azimuthal order than the gain/loss pattern (A,B) or a different one (C,D) (figure from [20]).

gain parts (see Fig. 2.7(a)): it will give rise to laser resonance, but its frequency does not change. The other (previously degenerate) mode is more present in the lossy parts (see Fig. 2.7(b)): it will be absorbed, at the same frequency. All the other modes with different azimuthal orders are equally present in the gain and loss regions, and are thus neither amplified nor absorbed (see Fig. 2.7(c,d)). This choice of gain/loss pattern makes the two chosen modes enter the broken $\mathcal{PT}$ zone as soon as gain and loss is added. All the other modes need more gain and loss to be broken. So the azimuthal order of the gain/loss pattern defines the mode that creates a laser resonance. This is seen in Fig. 2.8 where one compares the laser output of a microring with uniform gain (Fig. 2.8(a)), to one with gain and loss as described (Fig. 2.8(b)). The first one exhibits multi-mode operation as several modes are present in the gain bandwidth, the second one exhibits single-mode operation as only one lasing mode is in the broken $\mathcal{PT}$ zone.

A second possibility is to couple two similar microrings, one with uniform gain and the other with uniform loss. In the passive case, the coupling of the two microrings breaks the degeneracy between their respective modes as in the coupled wavguides, this can be seen in the lasing spectrum of a pair of identical microrings with uniform gain (Fig. 2.9(c,d)). The exceptional points of these pairs depends only on the coupling constant and the gain and loss intensity. If we reach the exceptional point (broken $\mathcal{PT}$ zone) of only one pair of modes, again one mode will lase and the other will be absorbed. But the other pairs that are not in the broken $\mathcal{PT}$ zone feel a balance between gain and loss and do not amplify nor are damped. Only one mode is involved in the lasing phenomenon (Fig. 2.9(e,f)) and single-mode operation is achieved in comparison to a single microring with uniform

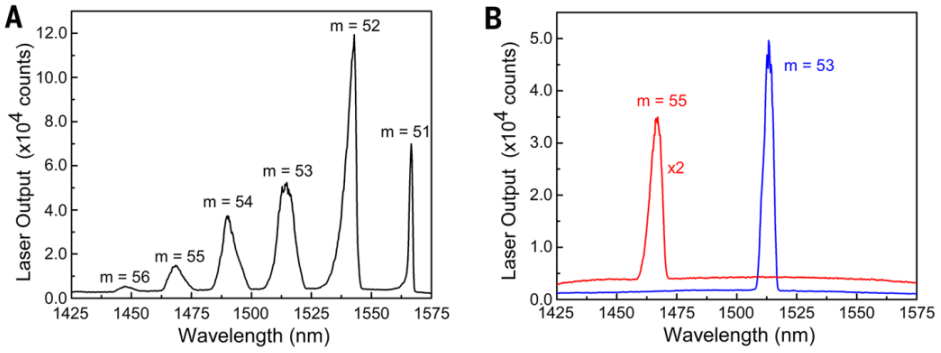

Figure 2.8: Lasing spectrum of a microring with uniform gain (A) or with gain loss pattern with an azimuthal order equal to 53 or 55 (B) (figure from [20]).

gain (Fig. 2.9(a,b)).

Robust light propagation

Disorder and defects induce back-reflections in photonic structures and hinder the possible applications. Topology has attracted attention in order to solve this problem: topologically protected edge modes can have the property to propagate in one direction only, and thus to allow for robust defect-immune transport. These modes typically require the breaking of time-reversal symmetry, e.g. with magnetic materials or with temporal modulation.

Non-Hermitian photonics, and the idea to use loss as an asset, also appeared in the context of robust transport. Non-Hermitian structures can have the property to amplify the forward propagating mode and to absorb the backward mode. A representative solution is a chain of rings coupled through auxiliary rings with gain and loss (see Fig. 2.10). The forward and backward modes are counter-clockwise in the main rings and clockwise in the auxiliary rings. The forward mode (left to right in Fig. 2.10) propagates only in the upper half of the auxiliary rings, which is the gain region. Inversely, the backward mode propagates only in the lower half of these auxiliary rings, which is the lossy region. This kind of structure demonstrates robust light transport in the presence of defects [51].

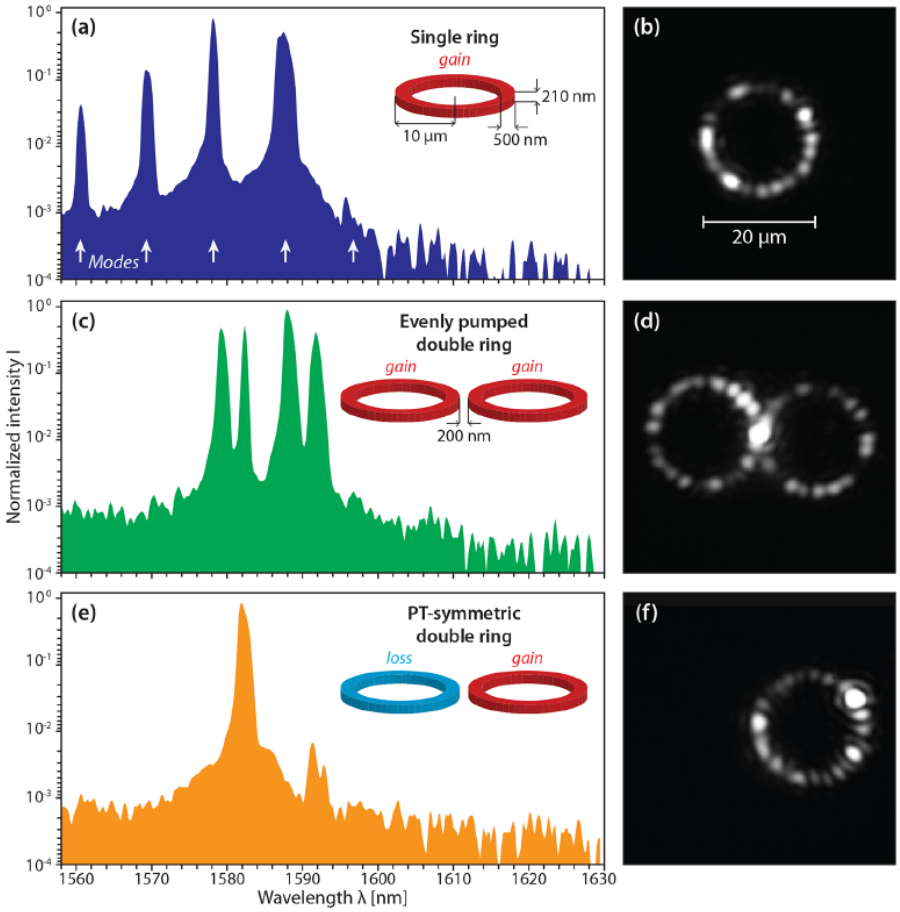

Figure 2.9: Lasing spectrum (left column) and intensity pattern (right column) of a single microring with uniform gain (a,b), of two coupled microrings with uniform gain (c,d) and $\mathcal{PT}$-symmetric coupled microrings (e,f) (figure from [50]).

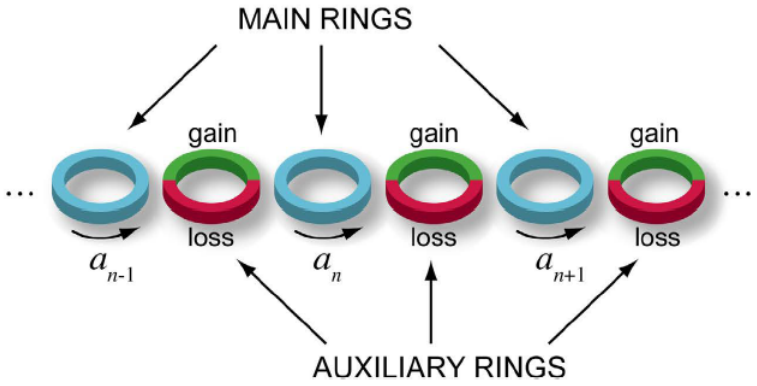

Figure 2.10: Example of photonic structure consisting of coupled rings with amplified forward mode and absorbed backward mode (figure from [51]).

3

Optical concepts

In this chapter we provide an overview of the main concepts utilized throughout this thesis. Sec. 3.1 prepares the field with Maxwell's equations leading to the Helmholtz equation and related concepts such as the Poynting vector, boundary conditions, and Fresnel coefficients. Afterwards, analytical models and simulation techniques adapted to various structures are presented in Sec. 3.2.

3.1 Photonics

The purpose of photonics is to transmit information with electromagnetic waves. It considers each step of this process from the emission of the information to its reception via multiple propagation channels and modulation.

The classical interaction of light with materials is defined by the Maxwell equations (Sec. 3.1.1). Sec. 3.1.2 introduces the Helmholtz equation and defines the Poynting vector and then we describe the Fresnel coefficients in Sec. 3.1.3.

3.1.1 Maxwell equations

Electromagnetic waves interact with the electrons and nuclei of materials. For our purposes, a quantum description of these interactions is not necessary. We focus on the Maxwell equations that describe the classical interplay between light and materials at a macroscopic level. If we consider a field with a harmonic variation

$e^{j\omega t}$, the equations can be written as [52]:

$$\nabla \cdot \mathbf{D} = \rho \tag{3.1}$$
$$\nabla \cdot \mathbf{B} = 0 \tag{3.2}$$
$$\nabla \times \mathbf{E} = -j\omega\mathbf{B} \tag{3.3}$$
$$\nabla \times \mathbf{H} = \mathbf{J} + j\omega\mathbf{D} \tag{3.4}$$

This set of equations connects the four macroscopic fields **D** (the dielectric displacement), **E** (the electric field), **H** (the magnetic field), and **B** (the magnetic induction) with the current densities **J** and the free charge ρ. In this work we will use the concept of modes. These are solutions of the Maxwell equations that propagate, even without internal sources of light, so we can set $\rho = 0$ and $\mathbf{J} = 0$.

Since we do not take into account the nonlinear optical response of the material, we can define the constitutive equations that describe the response of the material to the electromagnetic fields by:

$$\mathbf{D} = \varepsilon_0\varepsilon\mathbf{E} \tag{3.5}$$
$$\mathbf{B} = \mu_0\mu\mathbf{H} \tag{3.6}$$

with ε_0 and μ_0 the electric permittivity and magnetic permeability of vacuum, respectively. They are connected to the speed of light c through the relation $c = \frac{1}{\sqrt{\varepsilon_0\mu_0}}$. The dielectric permittivity ε describes the electric field response in a bulk material. In a similar way, the permeability μ describes its magnetic field response. We focus here on the non-magnetic isotropic case, so ε and $\mu(= 1)$ are scalars and not tensors. As described in Chap. 2, $\mathcal{PT}$ symmetrical structures experience gain and loss. As we will see, this induces that ε is complex at some point.

3.1.2 Helmholtz equation

Without external stimulation (**J** and $\rho = 0$) and by using the constitutive equations and the curl equations, we can find the wave equation:

$$\nabla \times \nabla \times \mathbf{E} = \mu_0\omega^2\mathbf{D} \tag{3.7}$$

leading to

$$\nabla(\nabla \cdot \mathbf{E}) - \nabla^2\mathbf{E} = \varepsilon\varepsilon_0\mu_0\omega^2\mathbf{E} = k_0^2\varepsilon\mathbf{E} \tag{3.8}$$

where we used $\omega/c = k_0$. In structures where ε is piecewise constant, we can reduce Eq. 3.1 to $\nabla \cdot \mathbf{E} = 0$, and the previous wave equation turns into the Helmholtz equation, which is also correct for the **H** field with these approximations:

$$\nabla^2\mathbf{E} + k_0^2\varepsilon\mathbf{E} = 0 \tag{3.9}$$
$$\nabla^2\mathbf{H} + k_0^2\varepsilon\mathbf{H} = 0 \tag{3.10}$$

The electric (magnetic) field profile solution depends on the boundary conditions at the interfaces (see Sec. 3.1.3).

In homogeneous media (ε constant), the solutions (or modes) are plane waves:

$$\mathbf{E} = \mathbf{E_0} e^{-j\mathbf{k}\cdot\mathbf{r}} \tag{3.11}$$

with the condition $\mathbf{E_0} \cdot \mathbf{k} = 0$ (from $\nabla \cdot \mathbf{E} = 0$) indicating that the field is perpendicular to the propagation direction. $\mathbf{k}$ is called the wavevector and indicates the direction of propagation. Its amplitude is defined by:

$$k = \frac{\omega}{c}\sqrt{\varepsilon_{\text{eff}}} = \frac{\omega}{c} n_{\text{eff}} \tag{3.12}$$

where n_{eff} is the effective refractive index, generally called the dispersion relation. The effective index is the link between ω and k. In homogeneous media the effective refractive index is equal to the refractive index of the material $n_{\text{eff}} = n = \sqrt{\varepsilon}$ and the dispersion relation is a straight line. We can already conclude that a homogeneous media with a complex refractive index will have a complex wavevector. The sign of the complex component (via Eq. 3.11) leads to a damped (negative imaginary component) or amplified (negative imaginary component) plane wave.

Note that all along this work, material dispersion will be neglected, meaning that we simply fix the material index in the frequency region of interest. In the frequency domain this does not constitute a restriction.

Like every wave, an electromagnetic wave transports energy. The resulting energy flow of a electromagnetic wave is represented by the Poynting vector. As we use harmonic fields, the time average of the Poynting vector is given by [53]:

$$\langle \mathbf{S} \rangle = \frac{1}{2} \Re \{ \mathbf{E} \times \mathbf{H}^* \} \tag{3.13}$$

with $*$ denoting the complex conjugation and $\Re$ the real part. It can be shown that the energy flow of a plane wave is given by:

$$|\langle \mathbf{S} \rangle| = \frac{\Re \{n\}}{2\mu_0 c} {\mathbf{E_0}}^2 \tag{3.14}$$

3.1.3 Fresnel coefficients

We briefly define the Fresnel coefficients for an incident plane wave (Eq. 3.11). They result from the boundary conditions of the electric and magnetic fields at a straight interface of two media labelled 1 and 2.

$$\widehat{\mathbf{n}} \cdot \{\mathbf{D}_1 - \mathbf{D}_2\} = 0 \qquad \widehat{\mathbf{n}} \cdot \{\mathbf{B}_1 - \mathbf{B}_2\} = 0 \tag{3.15}$$

$$\widehat{\mathbf{n}} \times \{\mathbf{E}_1 - \mathbf{E}_2\} = 0 \qquad \widehat{\mathbf{n}} \times \{\mathbf{H}_1 - \mathbf{H}_2\} = 0 \tag{3.16}$$

where $\widehat{\mathbf{n}}$ is a unit vector normal to the interface. Note that those boundary conditions are valid without current and charge ($\mathbf{J} = 0$ and $\rho = 0$).

Consider a plane wave propagating in medium 1 and impinging the interface with medium 2. Using the superposition principle the transmitted electric field in medium 2 (E_T) should match with the superposition of the incident (E_I) and the reflected (E_R) electric fields in medium 1. At normal incidence the transmission t

and reflection r coefficients are identical for both polarizations (TE and TM) [54] and are:

$$r \equiv \frac{E_R}{E_I} = \frac{n_1 - n_2}{n_1 + n_2}, \qquad t \equiv \frac{E_T}{E_I} = \frac{2n_1}{n_1 + n_2} \tag{3.17}$$

with n_1 (n_2) the complex refractive index of medium 1 (2).

The reflectance is defined as the reflected energy $|\langle \mathbf{S}_R \rangle|$ with respect to the incident energy $|\langle \mathbf{S}_I \rangle|$:

$$\frac{|\langle \mathbf{S}_R \rangle|}{|\langle \mathbf{S}_I \rangle|} = \left| \frac{E_R}{E_I} \right|^2 = |r|^2 = R \tag{3.18}$$

where we used Eq. 3.14 to find the reflection coefficient in Eq. 3.17. Similarly, the transmittance is defined as the transmitted energy $|\langle \mathbf{S}_T \rangle|$ divided by the incident energy:

$$\frac{|\langle \mathbf{S}_T \rangle|}{|\langle \mathbf{S}_I \rangle|} = \frac{\Re\{n_2\}}{\Re\{n_1\}} \left| \frac{E_T}{E_I} \right|^2 = \frac{\Re\{n_2\}}{\Re\{n_1\}} |t|^2 = T \tag{3.19}$$

The transmittance is therefore normalized by the permittivity of the two media. These two Eqs. 3.18 and 3.19 will be useful to describe the reflectance and transmittance throughout this work.

3.2 Semi-analytical and numerical models

In this section we further introduce the methods to describe the cavity resonances and the coupling with these resonances. Sec. 3.2.1 discusses Fabry-Pérot resonances and Sec. 3.2.2 presents coupled mode theory. Furthermore, we expose our simulation techniques for propagating waves with the eigenmode expansion method (Sec. 3.2.3) implemented in CAMFR, and the scattering and transfer matrix methods (Sec. 3.2.4). We conclude with a brief introduction to 1D periodic structures in Sec. 3.2.5.

3.2.1 Fabry-Pérot cavity

For many of the $\mathcal{PT}$ structures studied in this book (Chap. 4 and 7), the resonance interpretation is fairly straightforward via a Fabry-Pérot model (FP). The conventional FP structure is defined by a cavity enclosed by two partially reflective mirrors [55]. For a single frequency excitation, resonances arise inside the cavity and they induce local maxima in the transmittance spectra. These resonances results from constructive interference and were discovered by Charles Fabry and Alfred Pérot in 1897: they concluded that the interference induced contrast in the transmittance of a thin film could be used for interferometry [54].

This kind of resonance is produced via constructive interference of the wave after a round-trip inside the cavity. With β the wave vector of the light in the cavity medium, and l the length of the cavity, then the phase condition for a constructive interference is:

$$e^{-j\beta l} e^{-j\varphi_{r,L}} e^{-j\beta l} e^{-j\varphi_{r,R}} = e^{-j2m\pi} \tag{3.20}$$

Or equivalently

$$2\beta l + \varphi_{r,L} + \varphi_{r,R} = 2m\pi \tag{3.21}$$

where m is an integer defining the order of the resonance, and $\varphi_{r,L}$ and $\varphi_{r,R}$ the phases induced by the reflection (the phase of the left and right reflection coefficients r_L and r_R) at the partially reflective mirrors. As $\beta = \omega n/c$ with n the refractive index in the cavity, the frequency separation $\Delta\omega$ of the peaks is given by

$$|\Delta\omega| = \frac{c\pi}{2nl} \tag{3.22}$$

To excite a resonance, we could expect to need the exact resonance frequency ω_0. In fact there is a narrow band of frequencies around which the resonance can be excited. This widening of the acceptable exciting frequency range is due to the dissipation of energy in the cavity walls and in the dielectric of the cavity [53]. A measure of the sharpness of the resonance or the energy dissipation is the Q factor of the cavity [55]:

$$Q = \frac{\omega_0}{\omega_{\text{FWHM}}} = \frac{\omega_0 \tau}{2} \tag{3.23}$$

with ω_{FWHM} the full width at half maximum of the transmission resonance peak and τ the resonance lifetime.

3.2.2 Coupled mode theory

In this section we introduce Coupled Mode Theory (CMT), which will be useful for the description of the interaction between sharp resonant structures and waveguide modes in Chap. 6. CMT is strictly valid when the width of the resonance is far smaller than the resonance frequency [56]. In that case waveguide dispersion can safely be ignored [33]. Therefore, it is well-suited for various problems, and amongst them for the description of plasmonic [57] and photonic Fano resonances [58], or for aperture antennas [59].

This theory is established on the coupling of modes in a time-dependent formalism of optical resonators [55]. We assume a system (see Fig. 3.1) where a single mode optical resonator couples with m ports, which are single-mode waveguides in this work. Multiple resonators or resonator modes can also be modeled, by incorporating their interaction, or by simply connecting them with waveguides, as in Chap. 6. The equations of CMT are [56]:

$$\frac{da}{dt} = \left(j\omega_0 - \frac{1}{\tau}\right) a + \left(\langle\kappa|^*\right) |s_+\rangle \tag{3.24}$$

$$|s_-\rangle = C|s_+\rangle + a|d\rangle \tag{3.25}$$

where a is the complex amplitude of the mode in the cavity with ω_0 its center resonance frequency and τ the lifetime of the resonance. $|s_+\rangle$ and $|s_-\rangle$ correspond to the input and output waves in the ports, respectively. The various couplings are expressed by $\langle\kappa|$ for the resonator input and by $|d\rangle$ for the resonator output.

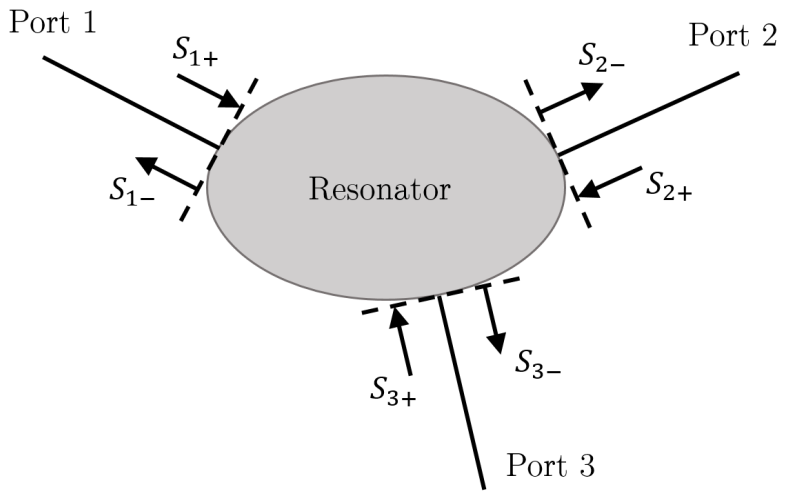

Figure 3.1: Schematic of an optical resonator system coupled with multiple ports. The arrows indicate the incoming and outgoing waves.

In addition, the incoming and outgoing waves in the ports can also couple through a direct pathway without intervention of the resonance, accounted for with a scattering matrix C.

Here we use the Dirac's bracket notation: the ket $|v\rangle$ can be represented by the column vector:

$$|v\rangle = \begin{bmatrix} v_1 \\ \vdots \\ v_n \end{bmatrix} \tag{3.26}$$

and the bra $\langle v|$ by a row vector:

$$\langle v| = \begin{bmatrix} v_1^* & \cdots & v_n^* \end{bmatrix} \tag{3.27}$$

with $*$ indicating complex conjugate.

With the lifetime of the resonance τ, the total decay rate is expressed as τ^{-1}. For our structure in Chap. 6 two factors are involved in this decay, the coupling τ_c^{-1} and the absorption/amplification τ_a^{-1}. The presence of loss in the cavity induces absorption, but inversely the presence of gain induces amplification with a negative decay rate. Another decay channel is here neglected, the radiation. The total decay rate is then given by:

$$\tau^{-1} = \tau_c^{-1} + \tau_a^{-1} \tag{3.28}$$

Note that the amplitude a is normalized such that $|a|^2$ corresponds to the energy in the resonator. Since $|s_{i+}|^2$ ($|s_{i-}|^2$) corresponds to the input (output) power propagating in port i, the conservation energy in the passive case ($\tau_a^{-1} = 0$) means

$$\frac{da}{dt} = \langle s_+|s_+\rangle - \langle s_-|s_-\rangle \tag{3.29}$$

We assume that τ and κ are independent of the frequency, this can be valid only if the dispersion of the waveguide mode around the cavity resonance is weak.

It means that the width of the resonance is smaller than the resonance frequency. With quantities oscillating with $e^{j\omega t}$, we can rewrite Eq. 3.24:

$$a = \frac{(\langle\kappa|^*)\,|s_+\rangle}{j\,(\omega-\omega_0)+1/\tau} \tag{3.30}$$

This equation highlights the single pole character of the resonator. In a similar way as for a Fabry-Pérot resonance, we can define a quality factor Q that links the narrowness of the transmission peak and the resonance lifetime (Eq. 3.23).

The parameters $\langle d|$ and $\langle\kappa|$ can be determined using time reversal transformation and energy conservation as described in [55] and one can find

$$\langle\kappa| = \langle d| \tag{3.31}$$

$$\langle d|d\rangle = 2/\tau_c \tag{3.32}$$

$$C|d\rangle^* = -|d\rangle \tag{3.33}$$

Eq. 3.31 shows a symmetry between input and output coupling. Eq. 3.32 shows that the output coupling is related to the decay rate of the resonance in the passive case. The energy escaping the cavity goes to the waveguides. The last equation shows that the coupling constants are linked to the direct scattering matrix C.

Using Eqs. 3.31 and 3.33 in Eqs. 3.24 and 3.25, the global process can be written with a scatter matrix S:

$$|s_-\rangle = S|s_+\rangle = \left[C + \frac{(\langle\kappa|^*)|d\rangle}{j(\omega-\omega_0)+1/\tau}\right]|s_+\rangle \tag{3.34}$$

In the special case of only one input waveguide, Eq. 3.34 can be rewritten

$$|s_-\rangle = S|s_+\rangle = C\left[1 + \frac{-2/\tau_c}{j(\omega-\omega_0)+1/\tau}\right]|s_+\rangle \tag{3.35}$$

using Eq. 3.32. For passive and reciprocal structures the scattering matrices will be unitary and symmetric, respectively. The coupled mode theory will be useful to describe the interaction of a chain of resonators and a waveguide, as we will see in Chap. 6.

3.2.3 Eigenmode expansion method

In this section we provide an overview of the linear mode expansion framework used in Chap. 4 with the numerical simulation program CAMFR [39].

The basis of mode expansion is the consideration of a structure that is invariant along a certain direction z. In this case ε and μ are independent of z. In theory, the structure may be infinite in the perpendicular direction(s). In practice, however, a boundary surface will always be introduced. In a general invariant structure the sourceless Maxwell equations have solutions of the form [32]:

$$\mathbf{E}(r) = \mathbf{E}(\mathbf{r}_t)e^{-j\beta z} \tag{3.36}$$

$$\mathbf{H}(r) = \mathbf{H}(\mathbf{r}_t)e^{-j\beta z} \tag{3.37}$$

with $\mathbf{r}_t$ the tangential component of $\mathbf{r}$, and β the mode propagation constant.

By inserting Eq. 3.36 in the Helmholtz equation 3.9, which is valid for (transversally) piecewise constant geometries, we obtain an eigenvalue problem:

$$(\nabla_t^2 + k_0^2\varepsilon)\mathbf{E} = \beta^2\mathbf{E} \tag{3.38}$$

hence the term eigenmode expansion. ∇_t^2 is the transverse Laplacian operator. The expression for the **H**-field is analogous.

If β has a real component the mode is propagative. If β has an imaginary part the mode amplitude is exponentially decaying or increasing. In the $\mathcal{PT}$ framework, propagative modes lay in the $\mathcal{PT}$-symmetric phase while decaying or increasing modes are present in the broken $\mathcal{PT}$-symmetric phase after an exceptional point. The modes with real β can persist in the absence of any sources, while maintaining their general shape. In the passive case, we can also have decaying (evanescent) modes which are excited at discontinuities between several structures, and are negligible a few (effective) wavelengths away from the interface.

Using adequate boundary conditions we obtain a set of eigenmodes. The forward propagating field in the structure, in response to an arbitrary excitation, can be written as a superposition of these modes [60]

$$\mathbf{E}(r) = \sum_i A_i \mathbf{E}_i(\mathbf{r}_t) e^{-j\beta_i z} \tag{3.39}$$

$$\mathbf{H}(r) = \sum_i A_i \mathbf{H}_i(\mathbf{r}_t) e^{-j\beta_i z} \tag{3.40}$$

with A_i complex mode amplitudes. In this way, with the knowledge of the modal field profiles and propagation constants, the field throughout the invariant structure is reduced to a vector of mode amplitudes:

$$(\mathbf{E}(\mathbf{r}), \mathbf{H}(\mathbf{r})) \leftrightarrow \mathbf{A} = [A_i] \tag{3.41}$$

The number of modes is infinite. However, for calculations the series has to be truncated to a finite number N. The results are still relevant, because the method converges as N increases. Indeed, the contributions of strongly evanescent modes become negligible.

From the Lorentz reciprocity theorem one can show that the modes are orthogonal. Furthermore, we can always normalize the profiles, and in our formalism the important orthonormality relation is expressed as:

$$\int_t (\mathbf{E}_i \times \mathbf{H}_j) \,.\, \mathbf{u}_z \mathrm{d}l = \delta_{ij} \tag{3.42}$$

with $\mathbf{u}_z$ the unit vector along z, δ_{ij} the Kronecker delta and integration along the transverse direction. Note that this orthonormality is only valid in the $\mathcal{PT}$ symmetric phase. Orthonormality in the broken $\mathcal{PT}$ symmetric phase needs to be redefined [46], but this new formalism is out of the scope of this book.

If an interface between two structures occurs, an incident mode can scatter. On the reflection side there are fields propagating in both directions. These bidirectional situations are also modeled by mode expansion, if we include backward propagating modes in equations 3.39 and 3.40. By splitting Maxwells equations in

transverse and longitudinal components, it is possible to show that a mode with components:

$$(\mathbf{E}_{i,t}, \mathbf{E}_{i,z}, \mathbf{H}_{i,t}, \mathbf{H}_{i,z}, \beta_i) \tag{3.43}$$

has a corresponding counterpropagating mode with:

$$(\mathbf{E}_{i,t}, -\mathbf{E}_{i,z}, -\mathbf{H}_{i,t}, \mathbf{H}_{i,z}, -\beta_i) \tag{3.44}$$

3.2.4 Scattering matrix and Transfer matrix formalism

Propagation through a 1D optical structure can be described by a scattering matrix S. This matrix connects the incoming and outgoing amplitudes of a wave as follows:

$$\begin{pmatrix} b_L \\ f_R \end{pmatrix} = \begin{pmatrix} r_L & t \\ t & r_R \end{pmatrix} \begin{pmatrix} f_L \\ b_R \end{pmatrix} = S \begin{pmatrix} f_L \\ b_R \end{pmatrix} \tag{3.45}$$

with $f_{L/R}$ or $b_{L/R}$ the amplitude of the forward or backward propagating mode at the left/right of the structure (see Fig. 3.2 for convention). For a plane wave, r_L and r_R are the left and right reflection coefficient respectively and t is the transmission coefficient. For more complex modes, these coefficients are determined via the mode-matching technique. This technique imposes continuity of the tangential total field. The coefficients depend on overlap integrals of the modes at the interface.

Figure 3.2: Description of a finite 1D structure with the incoming and outgoing waves.

As all the systems we study are reciprocal, transmissions from the left and the right are equal, which implies that S is symmetric. In the passive case, S is unitary ($\mathcal{T}$ symmetric) as a consequence of the conservation of the probability or in our case the intensity of the amplitude. This leads to the equations:

$$|r_L|^2 + |t|^2 = 1 \tag{3.46}$$
$$|r_R|^2 + |t|^2 = 1 \tag{3.47}$$
$$tr_l^* + r_R t^* = 0 \tag{3.48}$$

The two first equations induce that the left and right reflectances are equal $R_L = R_R = R$ with $R_{L/R} = |r_{L/R}|^2$. This leads to the familiar conservation relation for the passive case:

$$R + T = 1 \tag{3.49}$$

When we add gain and loss in a $\mathcal{PT}$ symmetric fashion, S-matrix respects $\mathcal{PT}$ symmetry. It means that there is a broken and an unbroken $\mathcal{PT}$ phase. In the unbroken phase each S-matrix eigenstate is mapped back to itself under the $\mathcal{PT}$ operation, whereas in the broken phase they are mapped to each other. At the boundary, called the exceptional points, the two eigenstates merge. To identify these phases one can examine the eigenvalues of S [61], which have unity module only in the unbroken phase. Alternatively, one can use the quantity $(R_L+R_R)/2-T$, which is below (above) unity in the unbroken (broken) phase, respectively. When this quantity is equal to one, it describes the boundary between the two phases. The potential lasing states of a 1D $\mathcal{PT}$ structure only appear in these broken phases [62].

The objective is to model structures consisting of several layers and interfaces. Therefore we have to combine their S matrices to obtain the total S matrix of the whole structure. This so-called S-scheme is numerically the most stable.

Another scheme, that is popular in single-mode methods, is the transfer matrix scheme. The transfer matrix formalism gives computational advantages [63] in comparison with the S-scheme but it is counterbalanced by a lesser stability for non-linear simulations for example [64]. As we use a linear single-mode structure in Chap. 6, we will use the transfer matrix formalism. It examines the propagation of an incoming wave along a given fixed direction. Instead of connecting the outgoing and the incoming amplitudes, the transfer matrix M connects the amplitudes on the right side to the left one:

$$\begin{pmatrix} b_R \\ f_R \end{pmatrix} = \begin{pmatrix} 1/t & -r_L/t \\ r_R/t & 1/t^* \end{pmatrix} \begin{pmatrix} b_L \\ f_L \end{pmatrix} = M \begin{pmatrix} b_L \\ f_L \end{pmatrix} \tag{3.50}$$

Note that $\det(M) = 1$ if the external refractive indices are equal, even in the presence of gain and loss [65].

Each layer of the structure is represented by a transfer matrix. Then the whole transfer matrix is obtained via the multiplication of each layer's transfer matrix. The transfer matrix can be viewed as a mapping transforming the wave after it passes through each scatterer or layer. For an N layer structure, the total transfer matrix is described as:

$$\begin{pmatrix} b_R \\ f_R \end{pmatrix} = M \begin{pmatrix} b_L \\ f_L \end{pmatrix} = M_1 M_2 \cdots M_{N-1} M_N \begin{pmatrix} b_L \\ f_L \end{pmatrix} \tag{3.51}$$

When we add gain and loss in a $\mathcal{PT}$ symmetric fashion, the conservation relation 3.49 is replaced by another one. As $\det(M) = 1$ is still valid, we can deduce:

$$r_L r_R = t^2 \left(1 - \frac{1}{T}\right) \tag{3.52}$$

which leads to the generalized conservation relation:

$$\sqrt{R_L R_R} = |T - 1| \tag{3.53}$$

This equation is very useful to understand the different behaviours of all single mode 1D structures with $\mathcal{PT}$ symmetry. Eq. 3.53 can be reduced to $T+\sqrt{R_L R_R} = 1$ if $T < 1$. This relation reminds us of the conservation relation 3.49 where the

reflectance R of the passive case is replaced by a geometric mean of the left and right reflectances of the $\mathcal{PT}$ symmetric case. So in general $R_L \neq R_R$, which implies that the scattering from one side loses power while the scattering from the other side gains power. Naturally, unintended equality of R_L and R_R can occur by varying some parameter (e.g. wavelength) in a complex $\mathcal{PT}$ structure.

When $T > 1$, the conservation relation becomes $T - \sqrt{R_L R_R} = 1$. In that case, the scattering from both sides gains power. Unintended degeneracy of the reflectances ($R_L = R_R$) is also possible leading to a pseudo conservation equation $T - R = 1$.

Finally when $T = 1$ we find $\sqrt{R_L R_R} = 0$, which signifies that at least one of the reflectances is equal to zero (or both, if degenerate). Such a scattering process can be called an anisotropic transmission resonance (ATR) [61]. In the non-degenerate case, we have a power conserving scattering process from one side, while from the other side the scattering process gains power. ATRs arise from transmission resonance ($T = 1$) of passive cases when $\mathcal{PT}$ symmetry (gain/loss) is added, this will be shown in Chap. 6 and 7.

3.2.5 Periodic structure

If we specify a structure to be periodic along the z direction as in Fig. 3.3, this means for the permittivity:

$$\varepsilon(z) = \varepsilon(z + a) \tag{3.54}$$

with a the period. Using this symmetry only, it is possible to show that the modes have the following structure [66]:

$$\mathbf{E}(z) = \mathbf{u}_k(z) e^{-jk_z(\omega)z} \tag{3.55}$$

with $\mathbf{u}_k(z)$ having the same lattice periodicity:

$$\mathbf{u}_k(z) = \mathbf{u}_k(z + a) \tag{3.56}$$

These modes are called Bloch modes and k_z is the Bloch propagation constant. This is the main result of the Floquet-Bloch theory.

As we have seen, the dispersion $k(\omega)$ of plane waves in homogeneous media is a straight line. This is no longer the case for periodic structures as we can see in Fig. 3.4. This dispersion relation is obtained for the structure of Fig. 3.3 with $n_1 = 1.0$ and $n_2 = 2.0$ and with the same widths $d_1 = d_2 = 0.5a$. One of the main results is the presence of gaps called bandgaps. At frequencies inside these gaps, no k_z is available and so there is no propagating mode in the z direction. Conversely, outside these gaps, there is an infinity of propagating modes forming bands. The usual graphs of ω as a function of k_z are called band diagrams or band structures.

Bandgaps always occur in a 1D structure with normal incidence and $n_1 \neq n_2$. The size of these bandgaps increases with the contrast between the two refractive indices. No propagating modes lay inside these bandgaps but there are evanescent modes with complex k_z. As these evanescent modes do not respect the translational symmetry of the system, they can not be excited in perfect infinite structure. They

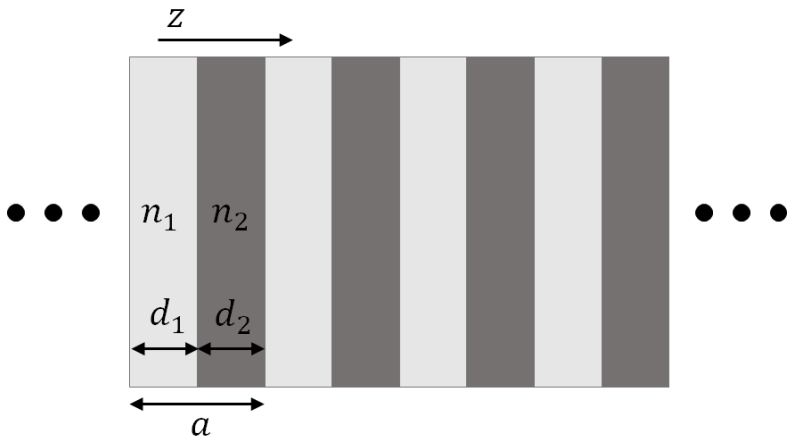

Figure 3.3: Infinite periodic structure along z composed of a succession of two layers of different materials.

can only appear around defects or at the boundaries of the crystal where they can localize and form a resonance.

As we can see in Fig. 3.4, the bands display a periodic behaviour. With the equivalence of the solutions, we can restrict our studies to the interval $k_z = [-\pi/a, \pi/a]$ to obtain all the necessary information. This interval is called the first Brillouin zone in the reciprocal or k-space. Moreover, the symmetry between forward and backward modes allows us to only consider $k_z = [0, \pi/a]$, the reduced Brillouin zone.

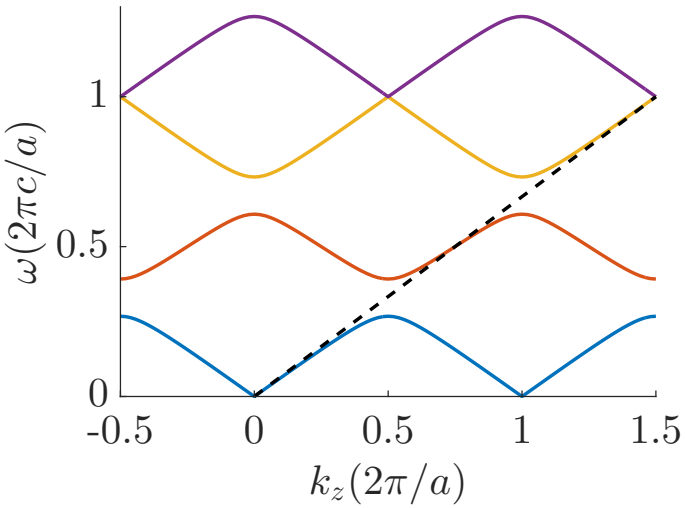

Figure 3.4: Band structure of a periodic structure. We observe bandgaps or regions of ω where no mode or k_z is available. The dashed line shows the dispersion of a homogeneous medium with an averaged refractive index $(d_1 n_1 + d_2 n_2)/a = 1.5$

Physically, the bandgaps can be understood as a consequence of multiple reflections and interferences on each interface of the structure. Another physical interpretation is found via the field profiles of the modes just above or below a bandgap. These two modes have the same periodicity but one is more localized in

high index regions, and inversely for the other mode. Being localised in high index regions tends to decrease the frequency of the mode. This establishes a difference of frequencies between the two modes and opens a bandgap.

Adding balanced gain and loss in a periodic structure is not straightforward. A first idea could be to add gain in one of the material ($\Im(n_1) = +\gamma$) and loss in the other ($\Im(n_2) = -\gamma$), with γ the gain/loss factor. But in this case, the mode just below/above the first bandgap and more situated in the high/low refractive index n_2/n_1 does not feel a balance between gain and loss. The modes will experience amplification or absorption as soon as $\gamma \neq 0$, and they will not split from an exceptional point, rendering this configuration non $\mathcal{PT}$-symmetric. If we want a

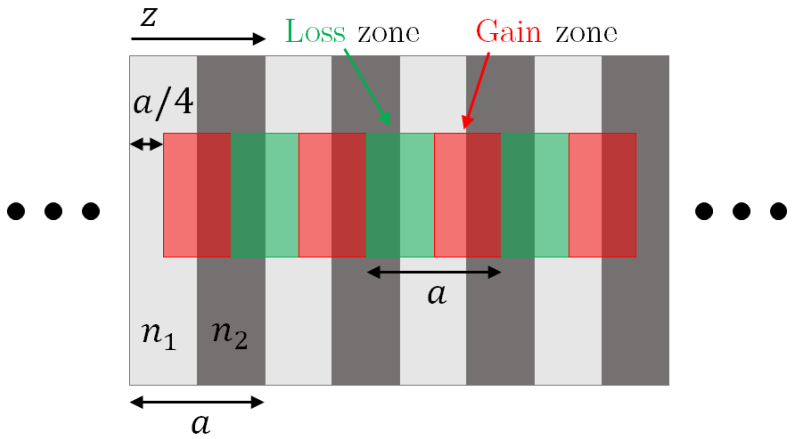

Figure 3.5: Infinite periodic structure along z composed of a real (n_1,n_2) and imaginary (gain and loss) periodic modulation of the refractive index. These two modulations have the same period but the imaginary one is translated from a quarter period compared to the real one.

real balanced mapping of gain and loss, they must be equally present in each layer. This can be done by using a complex modulation of the refractive index with the same period as the real modulation, but translated by a quarter period (see Fig. 3.5). The band structure in Fig. 3.6 is obtained with this mapping and $\gamma = 0.5$. As presented in the previous chapter, the modes merge by pairs at exceptional points to become complex conjugates. We note that these exceptional points depend on k_z. For the two lowest bands, the exceptional point occurs at smaller γ at the edge of the Brillouin zone. We can observe that $\mathcal{PT}$ symmetry tends to merge the modes just below and above the first bandgap and thus tends to close the first bandgap (around $\omega = 0.3\ 2\pi c/a$) encircled by these two bands. With $\gamma = 0.5$, there are propagating modes for all frequencies below $0.55\ 2\pi c/a$. We can also observe that in the passive regime, the two modes of the two highest bands at the edge of the Brillouin zone are already degenerated (Fig. 3.4). $\mathcal{PT}$ symmetry will leave this degeneracy by giving a complex component to these two modes. For them, the exceptional point is situated at $\gamma = 0$ and they enter the $\mathcal{PT}$ broken phase as soon as $\gamma \neq 0$.

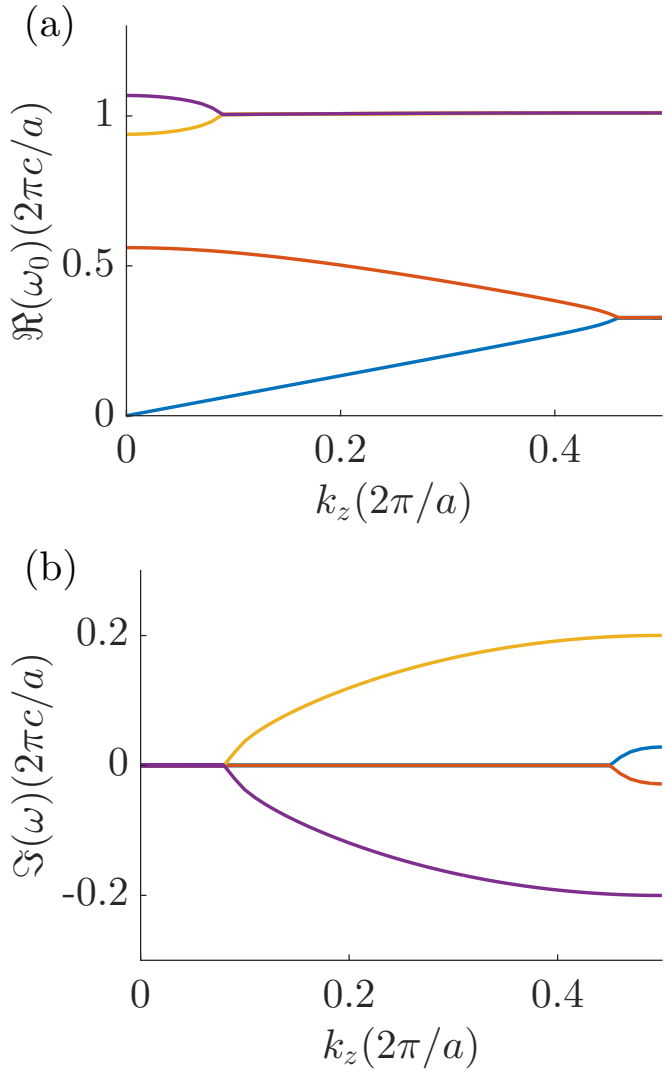

Figure 3.6: Real part (a) and imaginary part (b) of the band structure of a $\mathcal{PT}$ symmetric periodic structure with gain and loss.

4

Diffractive $\mathcal{PT}$-symmetric grating

4.1 Introduction

$\mathcal{PT}$ symmetry is widely investigated because of the novel light control abilities (see Chap. 2). In particular, it induces the modes of a structure to merge at exceptional points. In this chapter, we use this merging phenomenon to transform a specific high-contrast dual-mode diffraction grating [67] into a powerful switching device, by an intricate tuning of the guided modes propagating in the grating section.

In Sec. 4.2 we present the grating structure in its passive form, and discuss the transmission and reflection diffraction orders. The excitation and interplay of the two Bloch modes present in this grating allow us to compare it to a directional coupler. Next we describe the gain/loss pattern we use for this periodic structure, the motivation for this choice is found in Sec. 3.2.5. We perform the calculation and interpretation of its transmittance properties for different incidence conditions in Sec. 4.2.1 and 4.2.2. The longitudinal feedback of the finite-depth grating and the gain/loss properties of the modes lead to a rich interference structure. The grating now exhibits an exceptional point, leading to strong transmission contrasts between the available diffraction channels. Larger gain/loss beyond the exceptional point leads to laser-like resonance modes.

In addition, in Sec. 4.3 we adjust the periodicity of the real and imaginary parts of the refractive index, while preserving the $\mathcal{PT}$-symmetric character. With the correct excitation conditions, this leads to a mixing of previously uncoupled modes and a qualitative change of mode-merging at the critical points. Specifically, this configuration leads to two different exceptional points, instead of one, allowing for more variation in the diffraction properties.

This chapter is based on the work presented in [14].

4.2 Single period

We build upon a grating structure that was extensively discussed in [67] leading to strong diffraction contrasts. Here we examine this device when gain and loss are involved, for specific excitation conditions.

The model structure (Fig. 4.1(a)) is a silica grating in air, on top of a silica substrate, with a period p of 800 nm, grating depth d and a fill factor ff of 0.4 (the silica teeth width divided by the period). The refractive index of silica is fixed to $n_{\text{silica}} = 1.45$, and air has index 1. The structure is invariant along z (perpendicular to the plane of Fig. 4.1(a)), so essentially we examine a one-dimensional grating in a two-dimensional space.

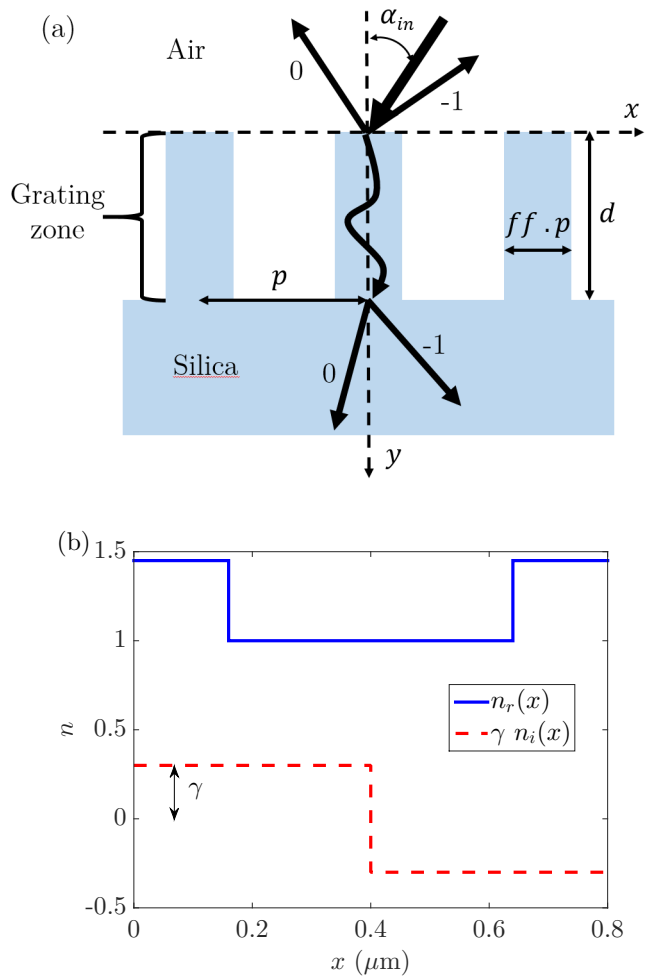

Figure 4.1: (a) The grating schematic. Light is incident with an angle α_{in}, there are two reflection orders and two transmission orders indicated. (b) Real (blue line) and imaginary part (dashed red line) of the index of refraction $n(x)$ along one period of the grating. The imaginary part is scaled by the (positive) factor γ.

When incident light reaches the top of the grating light is reflected via various reflection orders, with the number of orders depending on the period p, the wavelength of the incident light λ and the angle of incidence α_{in}. Additionally the light excites the propagating Bloch modes in the grating, which eventually reach

the second interface where they partially reflect and partially excite various available transmission orders (their availability also depends on n_{silica}). This process is described in detail in [67].

Now we apply gain/loss to the grating (Fig. 4.1(b)), so along the groove depth d in the grating zone, but not in the substrate below, via the refractive index $n(x) = n_r(x) + \gamma\, n_i(x)i$. We need to respect the usual condition for $\mathcal{PT}$ symmetry which is $n(-x) = n^*(x)$. The real part $n_r(x)$ is symmetric (and equal to 1.45 or 1) and $n_i(x)$ is antisymmetric (and equal to ± 1) with respect to the origin (here at the center of a silica section) thus $\gamma\, n_i(x) = \pm\gamma$. This choice of gain/loss pattern is discussed in Sec. 3.2.5. The amount of gain/loss injected is defined by γ, which is real and positive.

We choose this setup, with gain/loss partly in air, to introduce fewer parameters in the description. In practice one will need various dielectric media and indices, however the behaviour will remain the same.

To describe the grating we use rigorous two-dimensional numerical simulations (eigenmode expansion (see Sec. 3.2.3) with CAMFR [39] and finite element method with COMSOL [68]). We only examine TE polarization (one electric field component out-of-plane, along the z-direction).

In the following two sections we examine the grating with gain/loss for two specific incidence angles: the so-called Littrow mounting and perpendicular incidence. We choose these angles because they allow for a high-contrast interference behaviour, which is controllable via gain/loss in an interesting way. In addition, these two incidence conditions will meet and interact when we tailor the period in Sec. 4.3.

4.2.1 Littrow mounting

We use the parameters $\lambda = 1060$ nm and $\alpha_{\text{in}} = 41.5°$ to achieve a Littrow mounting. This kind of mounting ensures that the reflection order -1 propagates in the exact opposite direction of the incident light. Then there are two reflection orders (0 and -1) and two transmission orders (0 and -1). The two transmission (reflection) orders are also symmetrical compared to the y-axis. This structure achieves high transmission efficiencies in the study without gain/loss, almost all the power finishes in the two transmission orders [67].

Practically, the Littrow-mounting requires that the lateral (x) component of the propagation constant of the incident wave k_{x0} is equal to π/p. In this setup, we can see in the band structures (Fig. 4.2(a)) that the grating experiences only two guided modes with different longitudinal components (k_y) of the propagation constants in the grating zone. Each of these modes is excited at the top by almost half of the input power. This condition also ensures that the two modes are at the limit of the Brillouin zone of the grating. Furthermore, by adjusting the groove depth d, the interference between the two guided grating modes allows us to transmit almost all the power to the substrate, either to transmission order 0 or to order -1, similar to a two-mode interferometer [67].

We calculate the transmittance properties for each transmission order of this grating, with variations of the groove depth d and the gain/loss γ (Fig. 4.3). We clearly see two very different regimes on either side of $\gamma = 0.23$, which is the $\mathcal{PT}$

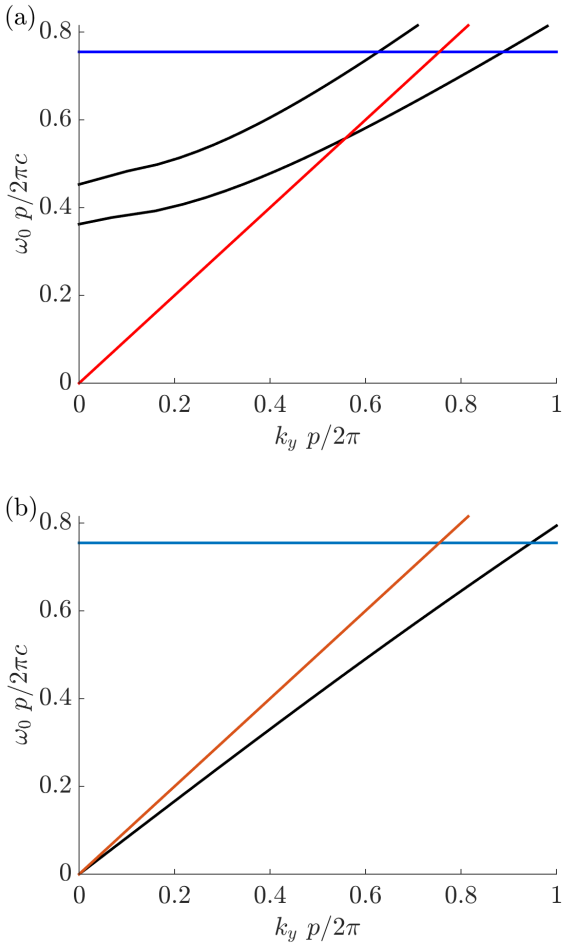

Figure 4.2: Band structures of the grating showing the longitudinal component (k_y) of the propagation constants of the propagating Bloch modes as a function of the frequency ω_0 for (a) the Littrow mounting ($k_x = \pi/p$) and (b) the perpendicular incidence ($k_x = 0$). The red line represents the light line and the blue line shows the frequency used in this chapter. In the Littrow mounting, propagating modes can exist below the light line because we only plot k_y and not the full propagation constant of the modes (with k_x taken into account).

symmetry breaking point (see Chap. 2).

Below this point ($\gamma < 0.23$) we have the usual two-mode coupling behaviour: in function of the groove depth the two guided modes interfere and allow light transmission in a specific proportion to the two different transmission orders. For example for a groove depth of 6.1 μm and $\gamma = 0$, all the light is transmitted to the order 0 ($T_0 \approx 1$), and none to order -1 ($T_{-1} \approx 0$).

When γ is increased, the distance needed to perform this exchange of power increases asymptotically. Near the breaking point the structure acts like a very efficient switching device. Indeed, with a fixed groove depth d (and therefore fixed geometry), we can choose in which channel we want the light to be transmitted with a very small gain/loss variation. This behaviour was pointed out in other geometries, e.g. in [16].

Beyond the breaking point ($\gamma > 0.23$) the behaviour is very different. We

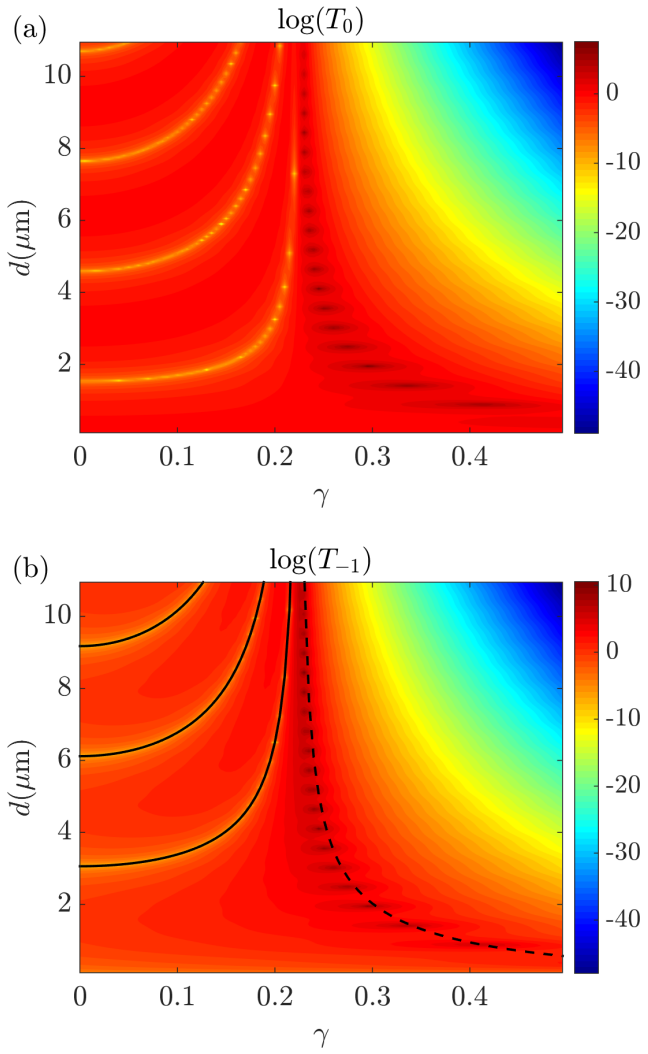

Figure 4.3: (a) Transmitted light to transmission order 0 (T_0) and (b) to diffraction order -1 (T_{-1}) for the Littrow-mounting case, in function of groove depth d and gain/loss factor γ. The graphs are in logarithmic scale with respect to the incoming power (0 indicates $T_{0/-1} = 1$). In (b) the three black lines below the critical point are the theoretical coupling lengths, and the black dashed line beyond the critical point indicates the theoretical phase resonance for lasing.

observe a laser-like resonance on the dark islands, indicating a very large transmission. For even higher γ we note that the light can no longer be coupled to the two different transmission orders and thus all the power finishes in the two reflection orders. So in the context of switching applications, beyond the breaking point all the light can be reflected.

We now explain all the previous phenomena in detail by analysing the two guided modes that propagate in the grating region for this Littrow-mounting case, via their effective refractive indices (Fig. 4.4(a)) and their field profiles (Fig. 4.4(b) and (c)). These effective refractive indices are defined from the longitudinal component (k_y) of the propagation constants of the propagating Bloch modes in the grating zone (so as if the grating teeth were infinitely long along y).

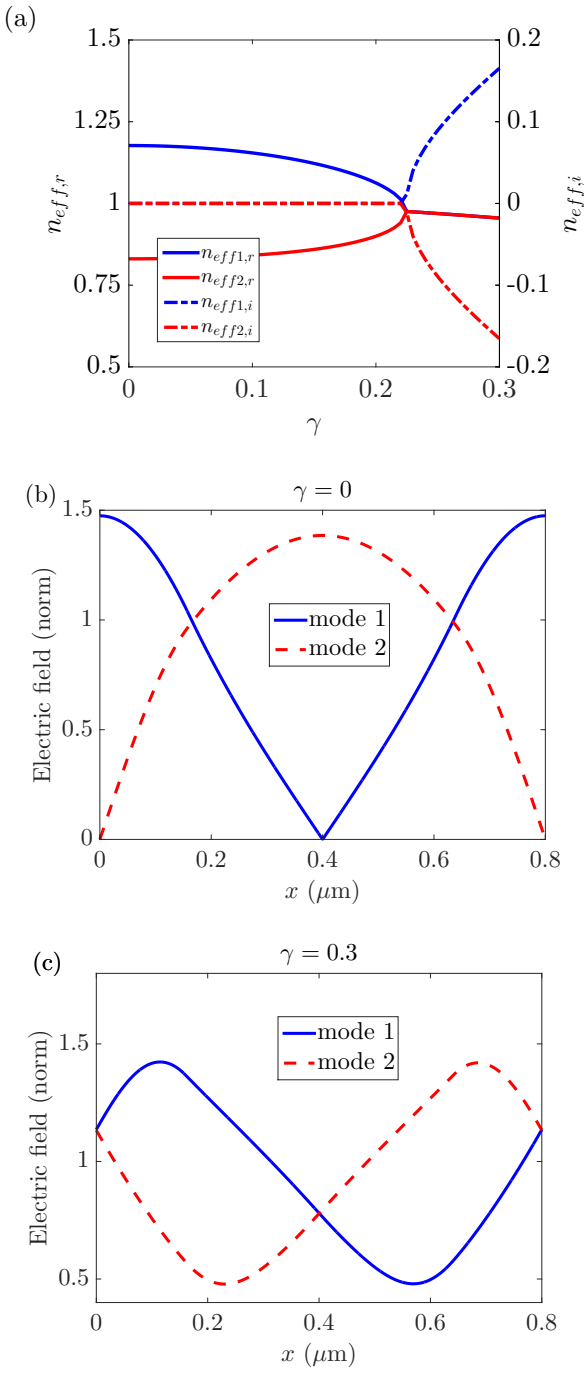

Figure 4.4: (a) Real (solid line) and imaginary (dashed-dotted line) part of the effective refractive indices of the two modes in function of γ (the amount of gain/loss). (b) and (c) The field profiles of the two modes at $\gamma = 0$ and $\gamma = 0.3$ respectively.

We observe the $\mathcal{PT}$ symmetry breaking point around $\gamma = 0.23$ (Fig. 4.4(a)). The real parts of n_{eff} for mode 1 and mode 2 merge, while one mode (mode 1) experiences gain (positive imaginary part) and the other (mode 2) experiences loss beyond the critical point. This is a well known phenomenon presented in Sec. 2.2.2 and also described for an infinite grating [26, 28].

The field profiles reflect this observation: for $\gamma = 0$ mode 1 (2) has its maximum (minimum) in silica and its minimum (maximum) in air (Fig. 4.4(b)), leading to the two different values of the real part of n_{eff}. For $\gamma > 0$ but still below the breaking point, these fields remain symmetric compared to the origin and are present with the same proportion in the gain and loss part, leading to a zero imaginary part of n_{eff} despite the presence of gain and loss. When γ is increased until the breaking point, mode 1 keeps this general shape but is flattened: The norm of the electric field increases at $x = 0.4$ μm and decreases at $x = 0$ and 0.8 μm. For mode 2, inversely, the electric field decreases at $x = 0.4$ μm and increases at $x = 0$ and 0.8 μm. This change continues until mode 2 almost matches the shape of mode 1 near the breaking point. Beyond this point, the two modes mirror each other (Fig. 4.4(c)) and are equally present in the air and silica part, leading to the same real parts of n_{eff}. However, one mode is more present in the gain part and the other in the loss part, leading to a non-zero imaginary part of n_{eff}, all consistent with Fig. 4.4(a).

Below the breaking point the effective indices (i.e. the propagation constants) come close to each other. This means that the coupling length (i.e. the groove depth period) needed for the two-mode interference increases. Indeed the distance needed to switch the outgoing power from one transmission order to the other is given by $\lambda/2(n_{eff1,r} - n_{eff2,r})$ (similar to the coupling length in Sec. 2.2.2). When the effective indices come closer and merge with each other, this distance increases asymptotically. This explains in Fig. 4.3 (and theoretically shown in (b)) the behaviour of the minimum transmission lines (yellow lines) below the breaking point, these lines appear when all the light is transmitted through the other transmission order.

Beyond the breaking point, the laser-like resonances (the points with very large transmission, the dark spots in Fig. 4.3) are explained by the round-trip Fabry-Perot effect of the particular mode that experiences gain (here mode 1). This is modeled via $\exp(-in_{eff}k_0 2d)r_1 r_2 = 1$ (similar to model of Sec. 3.2.1) with r_1 and r_2 the mode reflection amplitudes at the two interfaces, and $k_0 = 2\pi/\lambda$ the incident wave number. The phase equality of this equation gives us the localization of these large transmission points (dashed black line in Fig. 4.3(b)), while the amplitude equality gives us the periodicity of these large transmission points along the groove depth. The laser effect emits light towards the two transmission and the two reflection orders without interference of the other guided mode, since only the mode with gain is amplified and the other with loss is absorbed. This is clearly an effect stemming from the longitudinal discontinuity and finite length of the grating, which is not present in many of the 'standard' $\mathcal{PT}$ geometries such as the directional coupler [9–11] or in gratings [24–28]. Other $\mathcal{PT}$ structures have shown lasing properties e.g. with whispering-gallery modes [20–23].

The grating in the Littrow mounting case is interesting due to the high potential for switching applications. Moreover the understanding of its transmittance

properties is critical to understand the phenomena when we tailor the period in Sec. 4.3.

4.2.2 Perpendicular incidence

Now we study the transmittance properties of the grating with the same geometry, except that the light is perpendicularly incident, i.e. $k_{x0} = 0$. In this configuration the grating has only one propagating Bloch mode in the center of the Brillouin zone (see Fig. 4.2(b)). The grating possesses also one reflection order (0) and three transmission orders (+1, 0 and -1). We only show the power transmitted to the 0th transmission order (Fig. 4.5), because the +1 and -1 orders are not excited (except near the breaking point, discussed below).

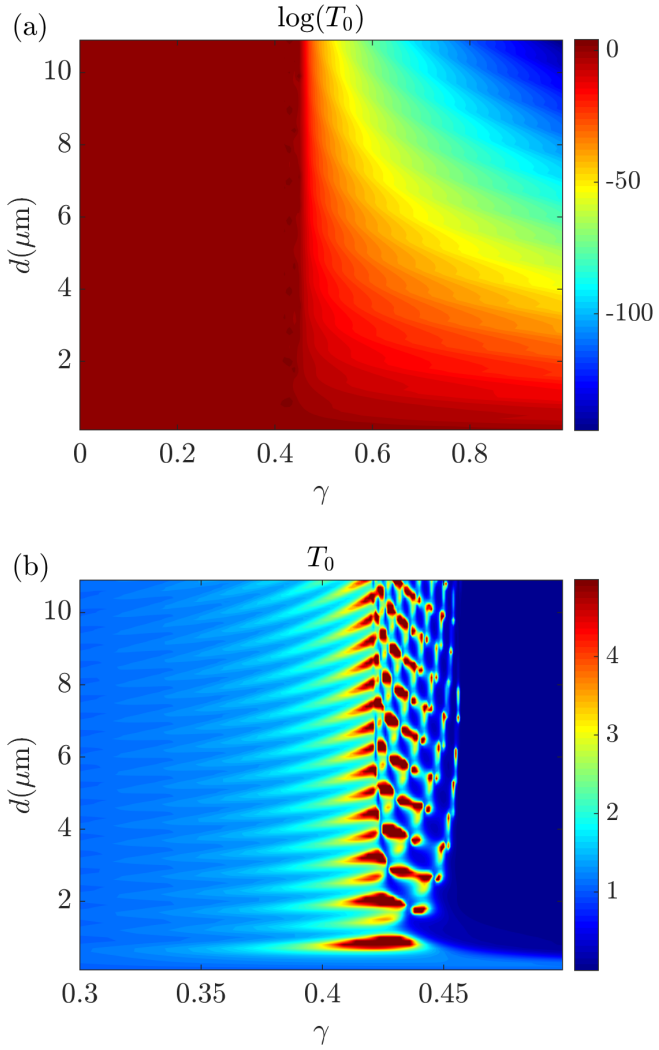

Figure 4.5: Transmitted light to diffraction order 0 for perpendicular incidence. (a) is in log scale and (b) is a zoom in linear scale but saturated at 5 for visibility.

There are three very different regimes delimited by $\gamma = 0.42$ and 0.46. In the first regime ($\gamma < 0.42$), almost all the light is transmitted to the zeroth transmission order. In the second regime ($0.42 < \gamma < 0.46$), there is a complex pattern in

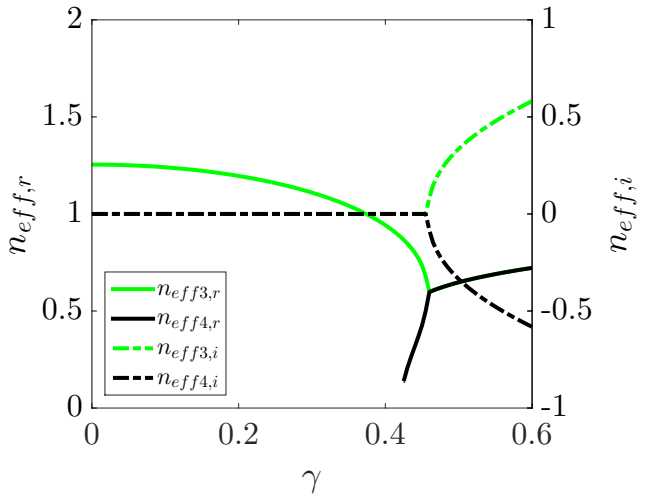

Figure 4.6: Real (solid line) and imaginary (dashed-dotted line) part of the effective refractive indices of the two modes in function of γ.

the transmittance. Finally, in the third regime ($\gamma > 0.46$), the light is reflected to the zeroth reflection order.

Again, the previous behaviours can be explained by analyzing the index of the modes that propagate in the grating for this incidence configuration (Fig. 4.6). We observe that there is only one propagating mode (mode 3) for the grating for $\gamma < 0.42$. This explains why all the light is transmitted to the zeroth diffraction order: the incoming perpendicular light (efficiently) couples with the only available guided mode, which at the exit interface (efficiently) couples with the forward diffraction mode (order 0). We do not have the two-mode interference as for the Littrow mounting case of the previous section. The lines we see in Fig. 4.5(b) is due to a Fabry-Perot effect of this single-mode. Note that on these lines the output power can exceed unity, even if the mode experiences no gain, because in $\mathcal{PT}$-symmetric structures the total power is not locally preserved [10,11,27]. Even for the unbroken $\mathcal{PT}$ phase, the modes are not power orthogonal and thus the power can oscillate [11].

However from $\gamma = 0.42$ a new propagating mode appears (mode 4). The mode numbers here (3 and 4) are used for later reference. When a $\mathcal{PT}$ structure supports an even number of modes (at $\gamma = 0$), each mode forms a pair with another. But when the structure supports an odd number of modes, a new mode emerges when γ is increased to form a pair with the last one. This was pointed out recently for a single multi-mode waveguide [13], and applies also in our Bloch mode case. Mode 4 is the new emerging mode due to the odd number of pre-existing modes (only mode 3). Modes 3 and 4 interfere to shape the interesting, complex pattern for a relatively narrow range of γ (for $0.42 < \gamma < 0.46$, Fig. 4.5(b)). Further on, this new mode quickly merges with mode 3 at the $\mathcal{PT}$ symmetry breaking point around $\gamma = 0.46$. Beyond this point we observe a behaviour similar to the previous Littrow mounting case, where all the light is reflected.

In this case when we apply the formula for the laser-like resonance (see Sec. 4.2.1), we find very small d values. For such small d, the grating is too thin (in comparison with the wavelength) and the evanescent modes do not vanish. Thus,

the modes can interfere with these evanescent modes and disturb the appearance of laser or Fabry-Perot modes. Nevertheless, the resonance seems to be vaguely present in Fig. 4.5(b) (a light blue line for small d and large γ).

The characteristics of the perpendicular case are very different from the Littrow case, since there is only one propagating mode (when $\gamma = 0$). With the studies of both cases, we have all the information to understand the more complex, period-doubled system.

4.3 Double period

Now we study the same diffraction grating, but with a double period (1.6 μm) for the imaginary part (of the refractive index in the grating zone), while the real part keeps the original period (0.8 μm) (Fig. 4.7). We examine this case because it remains $\mathcal{PT}$-symmetric, but the modal properties change qualitatively, as we will see.

From the geometry, it follows that an entire real period experiences gain, while the next one experiences loss and so on. By changing the total period with the same incidence as in the single-period Littrow mounting case ($\alpha_{\text{in}} = 41.5°$), we allow new orders to appear. There are three reflection orders (0, -1 and -2) and five transmission orders (+1, 0, -1, -2 and -3). The reflection (and transmission) orders 0 and -1 of the single-period case (Sec. 4.2) correspond to the newly labeled 0 and -2 orders (compare Fig. 4.1(a) with Fig. 4.7(a)). In addition, 'truly new' orders appear due to the halving of k_G, the reciprocal vector of the grating, by doubling the period (i.e. $k_G = 2\pi/p_d$ where p_d is the doubled period), these new orders are indicated with dashed arrows in Fig. 4.7(a).

We compute the transmittance properties of this new grating (orders 0, -1 and -2, Fig. 4.8) with the incidence of the single-period Littrow mounting configuration. The orders that are not shown do not provide more information. We observe three distinct regimes in function of γ. Below $\gamma = 0.24$ we recover a similar behaviour as for the single-period Littrow case (Sec. 4.2.1). Between $\gamma = 0.24$ and $\gamma = 0.43$ we retrieve laser-like resonances (Sec. 4.2.1), but also the transmittance without the two-mode interference (and with single-mode Fabry-Perot resonances) of the single-period perpendicular-incidence case (Sec. 4.2.2). Beyond $\gamma = 0.43$ we recover the usual behaviour of the two previous single-period cases beyond their critical points, all the light is reflected. In addition, transmission order -1 is not excited at $\gamma = 0$ (very thin blue line in Fig. 4.8(b)), because we retrieve the previous single-period Littrow configuration with only two diffraction orders, as the period is again the original value (for $\gamma = 0$), and order -1 does not exist.

The linear-scale transmission spectrum for a constant grating depth ($d = 0.6$ μm, Fig. 4.9) illustrates the three regimes in another way, with both dual-mode interference peaks, and a single-mode laser-like resonance.

Interestingly, this transmittance behaviour contains a mixture of the single-period Littrow-mounting and the perpendicular incidence case. For a closer analysis we calculate the modal effective refractive indices (Fig. 4.10(a) and (b)) and the field profiles (Fig. 4.11(a) and (b)). We use the same mode numbers as they were introduced in the single-period sections. The numbers are identified at $\gamma = 0$ because the single and double-period structures are the same in that case.

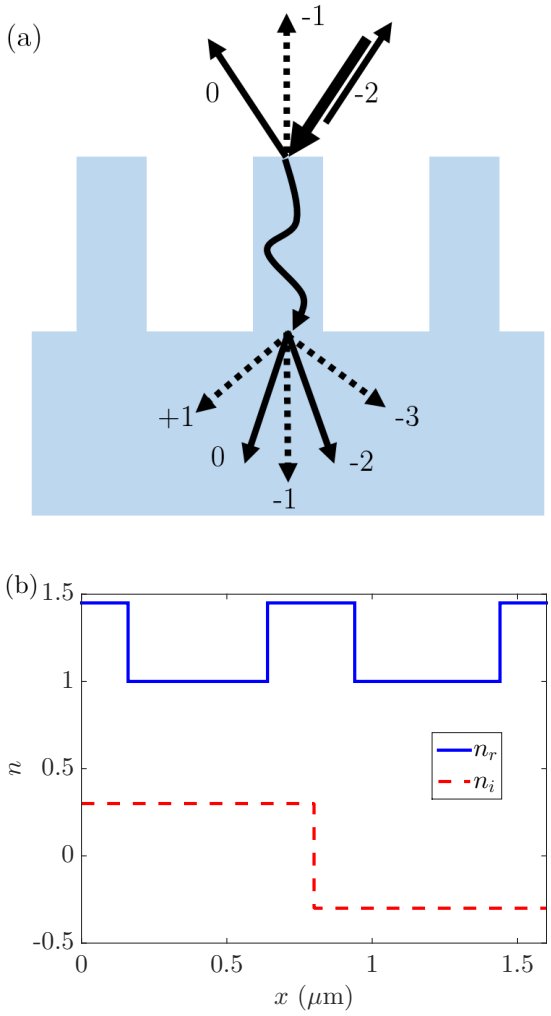

Figure 4.7: (a) All the orders allowed by the double period structure. The full arrows represent orders already present in the single period case, the dashed arrows represent orders that appear after period doubling. (b) Real and imaginary part of the index of refraction along one doubled period of the grating.

With the double period we have reduced the Brillouin zone (and thus the reciprocal lattice vector k_G), effectively coupling the angled orders (Littrow mounting) with the straight orders (perpendicular incidence). As a consequence mode 3 is now excitable from the angled incidence via diffraction with k_G. However, the mode is not yet excited when $\gamma = 0$, because then the reduction of the Brillouin zone is only virtual. Thus, at $\gamma = 0$ only modes 1 and 2 (the same as in the single-period Littrow case) are excited by the incident light with half the total power each, and this explains why transmission order 0 and -2 transmit almost all the power. When γ increases the mode profiles change (as we have seen in the single-period Littrow case) and the other transmission orders start to be excited, but their contribution remains limited (except near the first critical point and the laser-like resonances).

When γ increases, just as in Fig. 4.4(a), n_{eff} of mode 1 and 2 approach each other, and their interference (and coupling length) explains the exchange of output

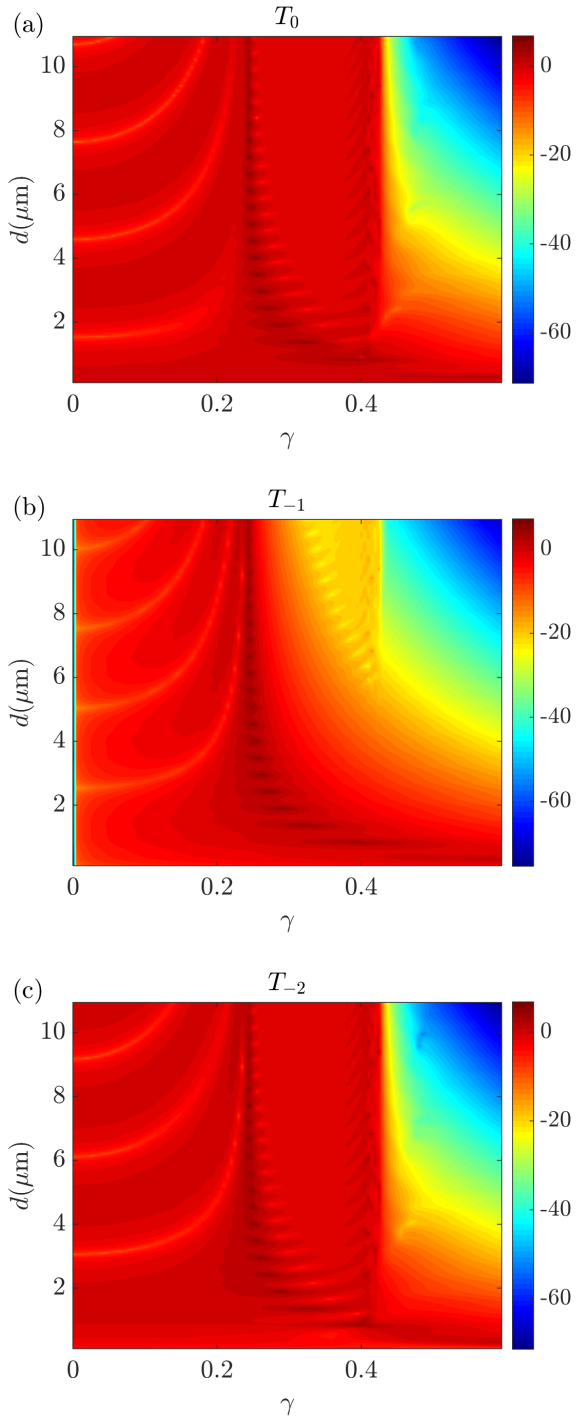

Figure 4.8: Transmitted power to transmission order (a) 0, (b) -1, and (c) -2 in the double period case. The three graphs are in log scale.

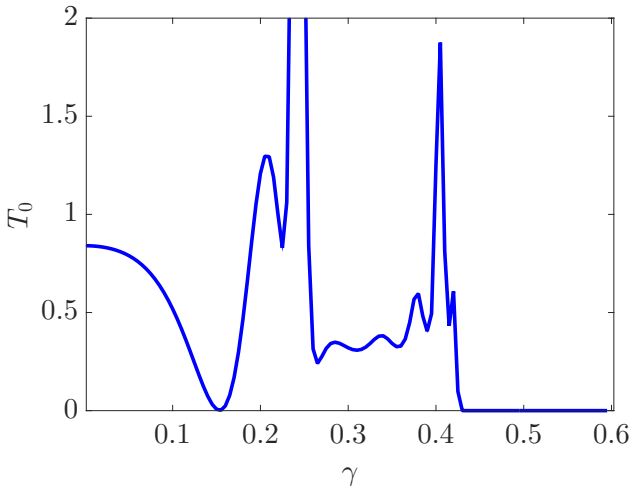

Figure 4.9: Transmitted power to transmission order 0 in the double period case with $d = 6$ μm.

power between the two diffraction orders in function of d. However, unlike previously, they do not merge together, mode 2 instead coalesces at $\gamma = 0.24$ with mode 3 (Fig. 4.10(a) and (b)), which is qualitatively different. This merging can also be seen in Fig. 4.11(a) and (b), the profile of mode 1 is quite stable between $\gamma = 0$ and 0.25. On the other hand, the profiles of mode 2 and 3 become mirror images of each other as they approach the $\mathcal{PT}$ symmetry breaking point. Previously, for the single-period case, this was instead for modes 1 and 2 (Fig. 4.4(c)).

Between $\gamma = 0.24$ and $\gamma = 0.43$ only mode 1 remains which is not coalesced and excitable. There is no two-mode interference anymore. The output power is quite stable, except for laser-like resonances (mostly just above $\gamma = 0.24$), and (weaker) Fabry-Perot resonances near $\gamma = 0.4$ (upwards slanting dark-red lines in Fig. 4.8(a) and (c). Further on at $\gamma = 0.43$ this mode merges with mode 4 that appears around $\gamma = 0.4$. This appearance is again connected to the odd number of initial modes, as in the perpendicular single-period case, although previously it was mode 3 and 4 merging instead of mode 1 and 4 here. Beyond the final merging point no excitable mode is left, so we retrieve the final regime when γ is too large and all the light is reflected.

For the same doubled grating, but under perpendicular incidence, we do not observe the same three regimes. The mode picture is the same as Fig. 4.8 but in that case only mode 3 is excited by the incident light and carries power. When it merges with mode 2 at $\gamma = 0.24$ and beyond, no light is transmitted anymore through the grating. We observe a transmittance pattern like Fig. 4.5(a) for the transmission order 0, but with the critical point at $\gamma = 0.24$ instead of $\gamma = 0.42$ as for the single-period perpendicular case. The merging between mode 1 and 4 at $\gamma = 0.43$ does not affect the transmittance properties because none of them is excited by the incident light.

Thus, separately tailoring the real and imaginary index periodicity leads to more complicated and interesting characteristics because of the appearance and interaction of new orders and modes. It allows for a change of the mode merging process through $\mathcal{PT}$ symmetry breaking.

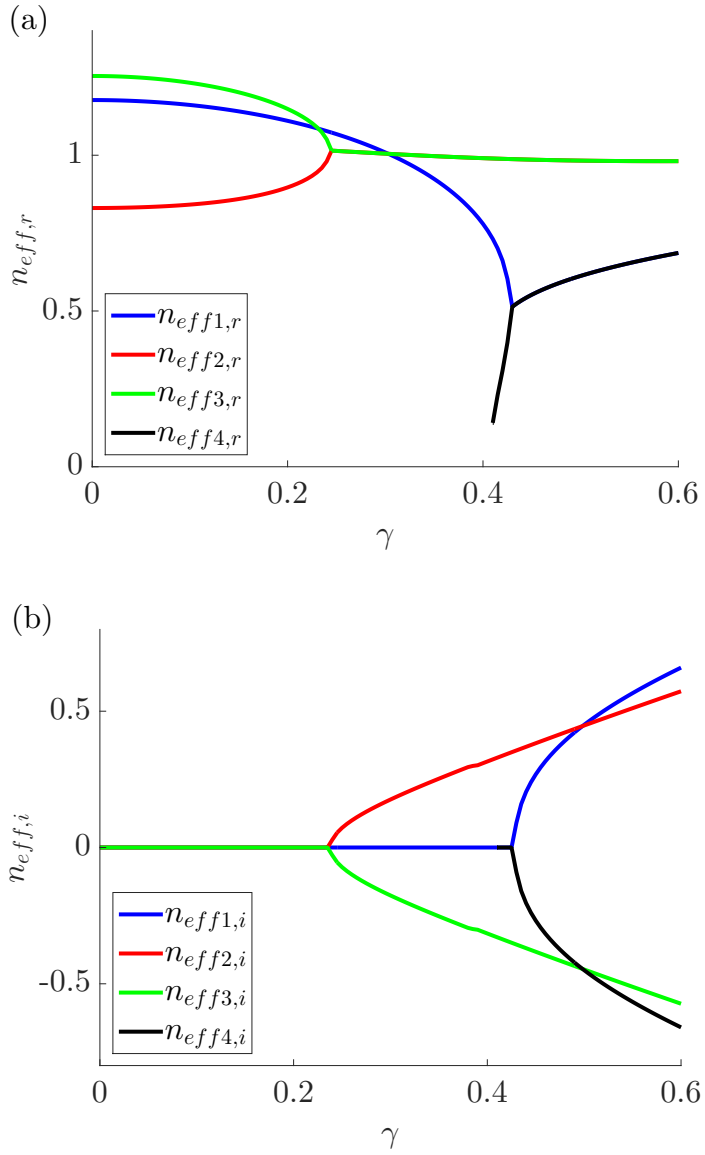

Figure 4.10: (a) Real and (b) imaginary parts of the effective refractive indices of the modes as a function of γ.

4.4 Summary

In this chapter we have analyzed, with rigorous simulations, the characteristics of a specific, finite $\mathcal{PT}$-symmetric diffraction grating. This structure experiences one or several symmetry breaking points when the gain/loss factor is increased. These points mark clear boundaries between very different regimes.

In the single-period Littrow case the structure experiences only one critical point. Beneath this point the interference between the two propagating modes allows us to transmit all the light to the desired diffraction order. Beyond this

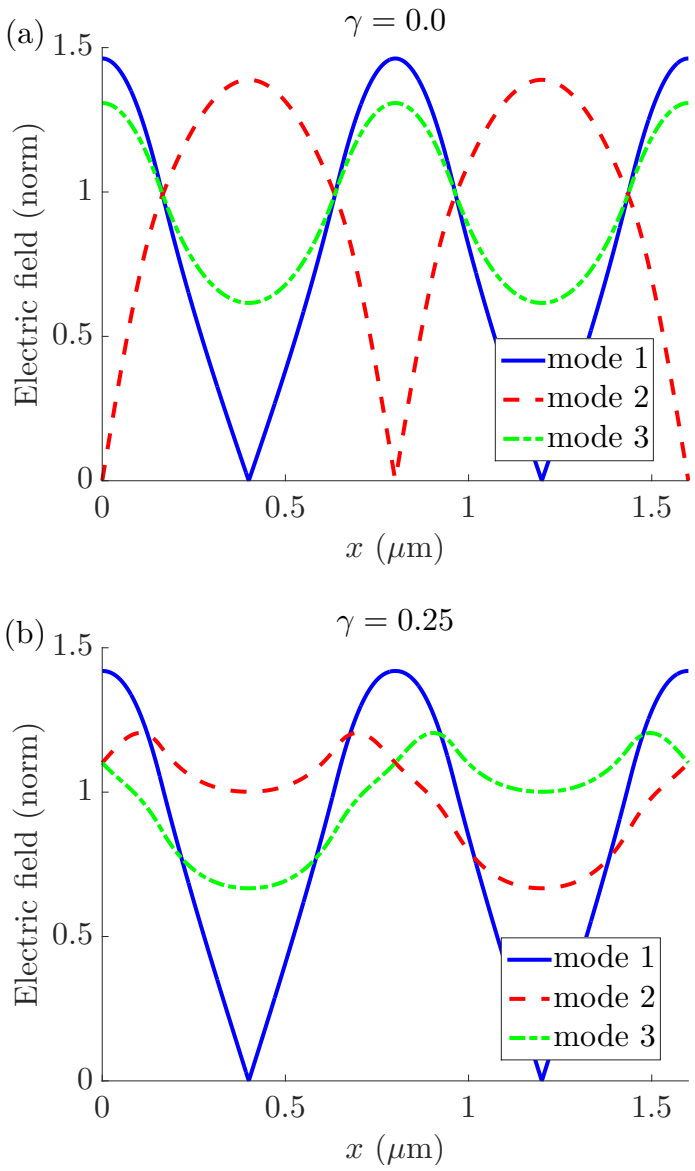

Figure 4.11: (a) and (b) show the field profiles of the three modes at $\gamma = 0$ and $\gamma = 0.25$, respectively.

point the light is no longer coupled to the modes and is reflected. In between, a laser-like resonance can be achieved with a suitable set of groove depth and gain/loss. These properties render this structure and configuration very useful for switching applications.

The single-period perpendicular incidence case also experiences only one critical point. As there is only one propagating mode the dual-mode interference scenario is not possible, and single-mode Fabry-Perot resonances appear. The odd number of modes leads to the appearance of a new Bloch mode, which merges when gain/loss is further increased.

Subsequently, we vary the imaginary and real parts of the index separately, taking care to conserve the $\mathcal{PT}$ symmetry. By period-doubling the imaginary part we observe an interesting mixing phenomenon between previously uncoupled

modes in the grating. This leads to a qualitatively different symmetry breaking picture, which shows elements of both the perpendicular and Littrow situations of the single-period configuration. This type of period adjustment can thus lead to tailored diffraction characteristics, by exploiting the limited number of guided modes in the grating.

For experimental implementation we believe that an integrated grating [69] with in-plane propagation would be the most feasible method. The two different thicknesses of the guiding layer can create the needed (effective) index contrast. The parameters (period, angle of incidence, thickness) are then adjusted to retrieve the desired grating properties, e.g. around the usual wavelength of 1.5 μm. The loss can be implemented as a judiciously deposited metal layer (e.g. chromium) with a controlled thickness on top of the grating [7, 20]. The gain is clearly the most complicated feature to achieve, and is typically done via dye molecules [70], quantum wells/dots [20] or rare earth elements [71]. For example InGaAsP multiple quantum wells on an InP substrate have reported gain coefficients of over 1000 cm^{-1} around 1.5 μm [72].

We note that one can decrease the needed gain for $\mathcal{PT}$ effects (such as the critical points) by decreasing the difference of refractive indices in the grating (i.e. the difference of layer thicknesses for an in-plane grating). However, this will increase the needed propagating length necessary to observe e.g. transmission order switching (as these lengths are proportional to the inverse of the effective index contrast). Thus one can decrease the necessary gain to reach an experimentally feasible value at the cost of device size and on condition that the platform provides for sufficient propagation lengths.

Interesting subjects for future study would be the effect of potential instabilities beyond the lasing points [73] which is approached in Chap. 6 or the influence of more sophisticated gain models, such as gain with saturation or with the charge carrier dynamics taken into account.

5

Symmetry recovery

5.1 Introduction

In the previous chapter, we transformed a simple grating into a powerful switching structure thanks to $\mathcal{PT}$ symmetry and the exceptional points. In this chapter we focus on these exceptional points and the different existing $\mathcal{PT}$ phases (unbroken and broken). The usual $\mathcal{PT}$ structures always switch from the unbroken to the broken phase via these exceptional points when the gain/loss factor increases. However, we present a simple structure that initially switches from unbroken to broken (as usual), but then reverts back to the unbroken phase via an 'inverse' exceptional point. Similar behaviour was reported for a complicated multimode model [74]. We show this phenomenon in the simplest possible four-mode linear model.

We first investigate and explain this phenomenon via a theoretical analysis in Sec. 5.2. The relative coupling between pairs of modes turns out to be crucial: the recovery of symmetry is only possible for particular coupling ratios. Furthermore, we numerically present the behaviour in two possible (dielectric and plasmonic) implementations in Sec. 5.3.

This chapter is based on the work published in [8].

5.2 Theoretical model

Our proposed structure contains four coupled modes, e.g. via dielectric waveguides (Fig. 5.1(a)) or plasmonic surfaces (Fig. 5.1(b)), which are in a particular $\mathcal{PT}$ configuration, and will be coupled in a judicious way. We remark that the specific nature of the waveguides does not matter. In a similar way as in Sec. 2.2.2, we

note for the unperturbed propagation constant $\beta = n_e k_0$ (so without coupling and without gain/loss), with n_e the effective index, $k_0 = 2\pi/\lambda_0$, and λ_0 the vacuum wavelength. The coupling constants κ_{ij} depend on the distance d_{ij} between the waveguides i and j. Gain is injected in the two upper modes, and the same amount of loss is considered for the two lower ones, via the same factor $\gamma_{core/cav}$, which ensures $\mathcal{PT}$ symmetry. This leads to a modal effective gain/loss parameter γ.

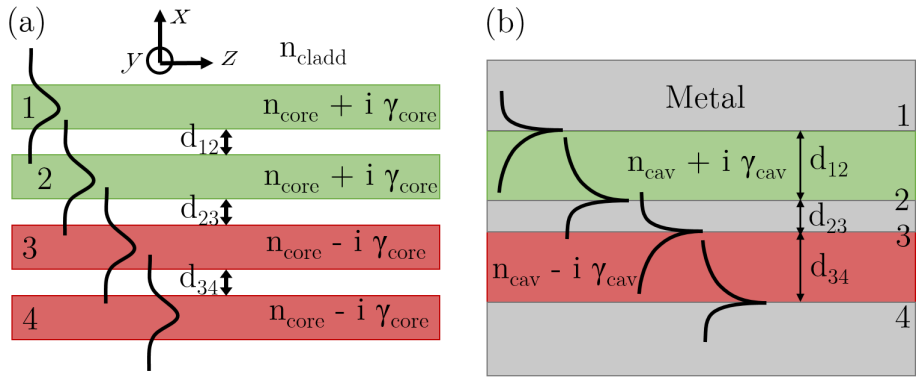

Figure 5.1: Two possible implementations: (a) Four dielectric slab waveguides, (b) four surface plasmon polariton modes at dielectric/metal interfaces.

Such a system can be described by the following matrix [47]:

$$\frac{i}{k_0}\frac{d}{dz}\begin{pmatrix} c_1 \\ c_2 \\ c_3 \\ c_4 \end{pmatrix} = \begin{pmatrix} n_e + i\gamma & \kappa_{12} & \kappa_{13} & \kappa_{14} \\ \kappa_{21} & n_e + i\gamma & \kappa_{23} & \kappa_{24} \\ \kappa_{31} & \kappa_{32} & n_e - i\gamma & \kappa_{34} \\ \kappa_{41} & \kappa_{42} & \kappa_{43} & n_e - i\gamma \end{pmatrix} \begin{pmatrix} c_1 \\ c_2 \\ c_3 \\ c_4 \end{pmatrix} \tag{5.1}$$

with c_i the amplitude of the unperturbed mode of waveguide i. As the waveguides are symmetric and reciprocal, we have $\kappa_{ij} = \kappa_{ji}$, and the coupling constants are determined via the lossless case. We assume nearest-neighbour coupling only. The odd/even properties of the refractive index along the x axis lead to the same distances between waveguide 1 and 2 and between 3 and 4, so $\kappa_{12} = \kappa_{34}$. The system becomes:

$$\frac{i}{k_0}\frac{d}{dz}\begin{pmatrix} c_1 \\ c_2 \\ c_3 \\ c_4 \end{pmatrix} = \begin{pmatrix} n_e + i\gamma & \kappa_{12} & 0 & 0 \\ \kappa_{12} & n_e + i\gamma & \kappa_{23} & 0 \\ 0 & \kappa_{23} & n_e - i\gamma & \kappa_{12} \\ 0 & 0 & \kappa_{12} & n_e - i\gamma \end{pmatrix} \begin{pmatrix} c_1 \\ c_2 \\ c_3 \\ c_4 \end{pmatrix} \tag{5.2}$$

The matrix eigenvalues lead to the propagation constants of the four supermodes $\beta_{coupled}$, that mix the four unperturbed modes, with the analytical form:

$$\beta_{coupled} = \beta \pm \sqrt{A \pm \sqrt{B}} \tag{5.3}$$

With:

$$A = \frac{\kappa_{23}^2}{2} + \kappa_{12}^2 - \gamma^2 \qquad B = \frac{\kappa_{23}^4}{4} + \kappa_{12}^2\kappa_{23}^2 - 4\kappa_{12}^2\gamma^2 \tag{5.4}$$

When γ increases A and B become negative at particular points, leading inexorably to a broken phase with complex conjugate eigenvalues. However, depending on the ratio $\alpha = \kappa_{23}/\kappa_{12}$, the structure shows a richer behaviour than just a single switch from the unbroken to a broken phase, as we now discuss. For the remainder of this theoretical analysis we normalize $\kappa_{12} = 1$, but γ and $\beta_{coupled} - \beta$ can be scaled for other values of κ_{12}.

The root of A happens when $\gamma = \gamma_A = [(2\kappa_{12}^2 + \kappa_{23}^2)/2]^{1/2}$, for B it is $\gamma = \gamma_B = \kappa_{23}(4\kappa_{12}^2 + \kappa_{23}^2)^{1/2}/(4\kappa_{12})$, and for $A - \sqrt{B}$ one finds $\gamma = \gamma_\pm = [(\kappa_{23}^2 - 2\kappa_{12}^2 \pm \kappa_{23}\sqrt{\kappa_{23}^2 - 4\kappa_{12}^2})/2]^{1/2}$. These four values are presented as a function of α in Fig. 5.2(f).

If $\alpha < 2$, $A - \sqrt{B}$ does not have real roots. $\beta_{coupled}$ becomes complex via $\sqrt{B}$, so when $\gamma > \gamma_B$ (= 0.56 in Fig. 5.2(a)). γ_B is the single exceptional point of the structure, and marks the switch between unbroken and broken $\mathcal{PT}$ phase (real versus imaginary $\beta_{coupled}$). In this case the two modes with largest $\beta_{coupled}$ merge, just like the third and fourth mode, which is the standard $\mathcal{PT}$ merging picture seen previously. However, for larger coupling the second and third mode tend to approach each other (around $\gamma = 1$ in Fig. 5.2(b)).

If $\alpha = 2$, $A - \sqrt{B}$ has a single degenerate real root ($\gamma_+ = \gamma_-$) but is still positive. At this special point ($\gamma = 1$, Fig. 5.2(c)) the structure has two degenerate modes ($\beta_{coupled} = \beta$), where the second and third mode touch. However, the exceptional point remains at a larger γ_B (= 1.42 in Fig. 5.2(c)).

If $\alpha > 2$ and $\alpha < (\sqrt{5} - 1)(\sqrt{5} + 2)^{1/2} \approx 2.54$, $A - \sqrt{B}$ has two different real roots ($\gamma_\pm$) and is negative for γ included between these two ($0.73 < \gamma < 1.37$ in Fig. 5.2(d)). So in this region there are two complex conjugate eigenvalues, and an extra broken phase appears. However, this new broken phase is finite, for γ between γ_+ and γ_B, all the eigenvalues are real again, the symmetry is recovered ($1.37 < \gamma < 1.52$ in Fig. 5.2(d), symmetry recovery (SR) zone in Fig. 5.2(f)). Therefore, we switch from unbroken to broken at γ_-, from broken to unbroken at γ_+ (symmetry recovery), and to the final broken phase at γ_B (Fig. 5.2(d)).

For $\alpha > (\sqrt{5} - 1)(\sqrt{5} + 2)^{1/2}$, γ_A is smaller than γ_B and γ_+ (Fig. 5.2(f)) and symmetry recovery is no longer possible. In this case we obtain a broken phase for $\gamma > \gamma_-$ (= 0.38 in Fig. 5.2(e)) (first exceptional point, for second and third mode), which is never unbroken, although there is a second exceptional point γ_A (for first and fourth mode, $\gamma_A = 2.62$ in Fig. 5.2(e)). The second and third modes that merge initially (as in the previous case), do not become real again.

In a compact way, we find symmetry recovery for $2 < \alpha < 2.54$ when γ is included between γ_+ and γ_B, see symmetry recovery (SR) zone in Fig. 5.2(f).

Thus, this simple $\mathcal{PT}$ structure can have a sequence of transitions between unbroken and broken phases, for a particular range of the mode coupling constants. Upon increasing the gain/loss, previously merged modes 'unmerge' again, and ultimately couple with another mode.

5.3 Dielectric and plasmonic implementations

The nature of the waveguides for this behaviour does not matter, so we can implement the system with both dielectric and plasmonic waveguides (Fig. 5.1), as

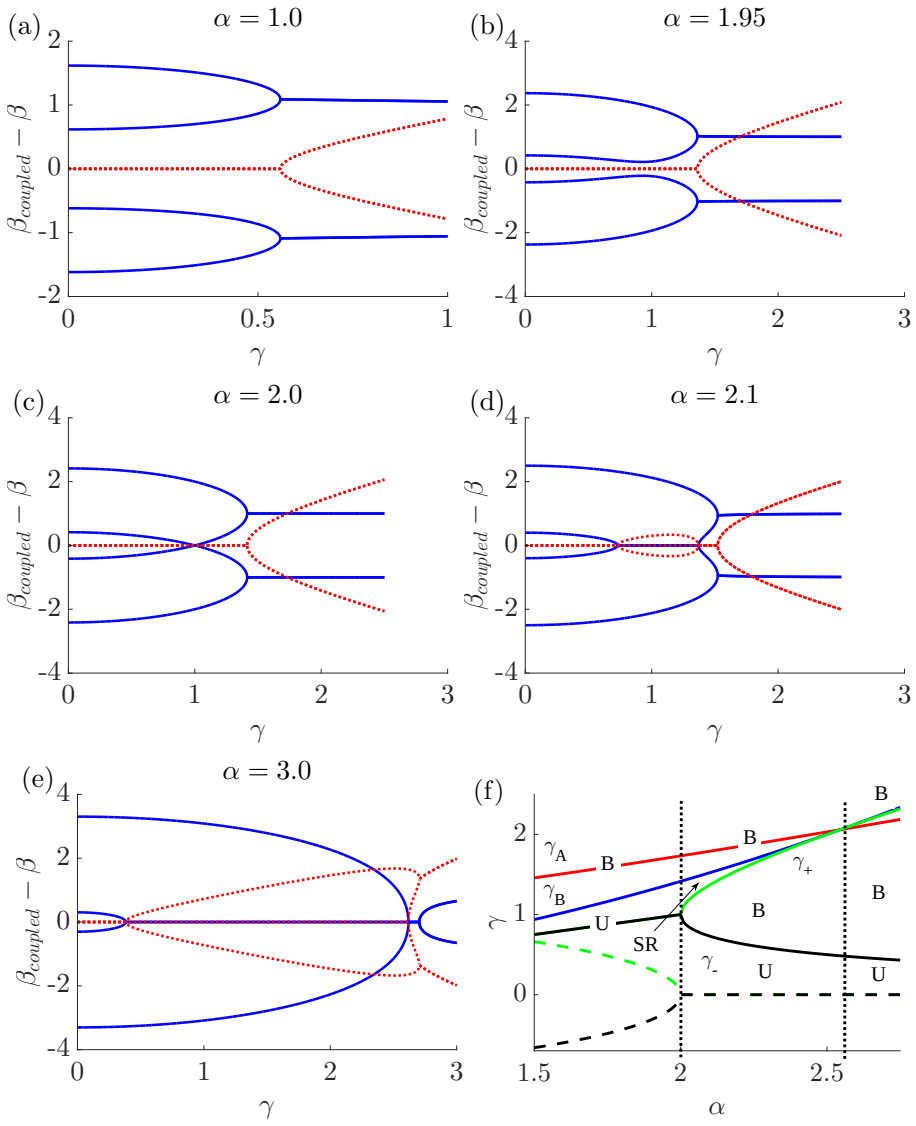

Figure 5.2: (a,b,c,d,e) Real (solid, blue) and imaginary (dotted, red) part of the supermode constants $\beta_{coupled} - \beta$ as a function of gain/loss γ, for specific values of α. (f) Evolution of γ_A (red), γ_B (blue), γ_+ (green line for real part and green dashed line for imaginary part) and γ_- (black line for real part and black dashed line for imaginary part) as a function of α. These values define the boundaries between the different $\mathcal{PT}$ phases: (U) unbroken, (B) broken and (SR) symmetry recovery. The dotted black lines ($\alpha = 2$ and $\alpha \approx 2.54$) delineate the three different regimes.

we demonstrate in the following part. This behaviour will become more physical when we examine the mode profiles for the plasmonic implementation.

The dielectric case (Fig. 5.1(a)) has four slab waveguides with $n_{core} = 3.5$ embedded in a medium with $n_{cladd} = 1.5$, the thickness of the slabs is 0.2μm and we use $\lambda_0 = 1.5\mu$m. We must have $d_{12} = d_{34}$ to ensure $\mathcal{PT}$ symmetry and we chose them equal to 0.3μm. We determine the four effective indices n_e as a function of γ_{core} for particular values of the distance d_{23} (and thus of the coupling constant

κ_{23}), see Fig. 5.3 for both the analytical (dotted line) and numerical dispersion (solid line).

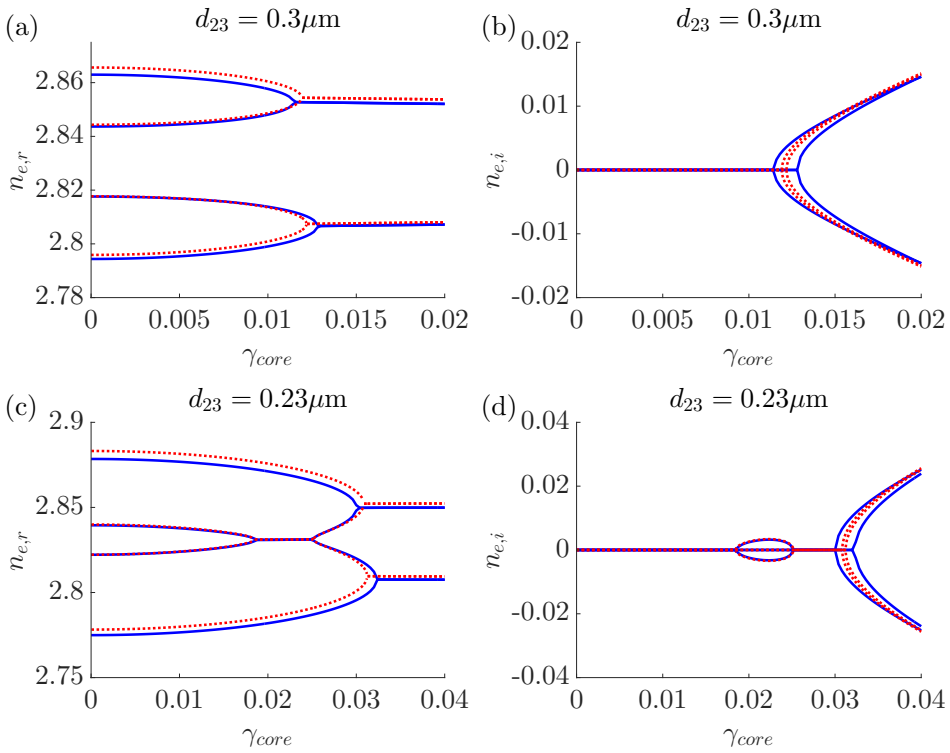

Figure 5.3: (a,c) Real and (b,d) imaginary parts of n_e as a function of γ_{core} for the dielectric structure at two values of d_{23}, with numerical (blue solid lines) and theoretical (red dotted lines) calculations.

For the theoretical calculation of n_e we calculate β and the mode profile of a single slab mode, the coupling constants are obtained with overlap equations [47]. Then we inject these parameters in Eq. 5.1 to obtain the eigenvalues of the system, without any fitting. On the other hand, the numerical calculations are performed with COMSOL [68] for the multiple waveguide system.

We obtain a good agreement between theory and numerics (Fig. 5.3). We have a typical case in Fig. 5.3(a,b) with $\alpha = 1$, and symmetry recovery in Fig. 5.3(c,d) with $\alpha = 2.024$. The behaviour is exactly the same as for the theoretical analysis of Sec. 5.2, except that the two final critical points are not at the same value of γ_{core} (e.g. around $\gamma_{core} = 0.012$ in Fig. 5.3(b)). This is due to the coupling constant between two non-neighbouring waveguides, which we did not include in the theoretical analysis of Sec. 5.2 for simplicity, but are taken into account in the theoretical and numerical calculations of Fig. 5.3.

For the plasmonic case (Fig. 5.1(b)) we have two dielectric layers separating three metal sections, so that four surfaces (with surface plasmon polariton modes) are available. We use a lossless metal with $n = -1.24i$ (corresponding to a Drude model with $\lambda_0 = 1\mu$m and plasma frequency $\omega_p = 3 \times 10^{15}$ rad/s). The dielectric layers with gain/loss have a thickness $d_{12} = d_{34} = 0.4\mu$m and $n_{cav} = 1$.

We calculate numerically n_e when we change γ_{cav} for two values of d_{23} (Fig. 5.4). Again we obtain symmetry recovery (case where $2 < \alpha < 2.54$) in Fig.

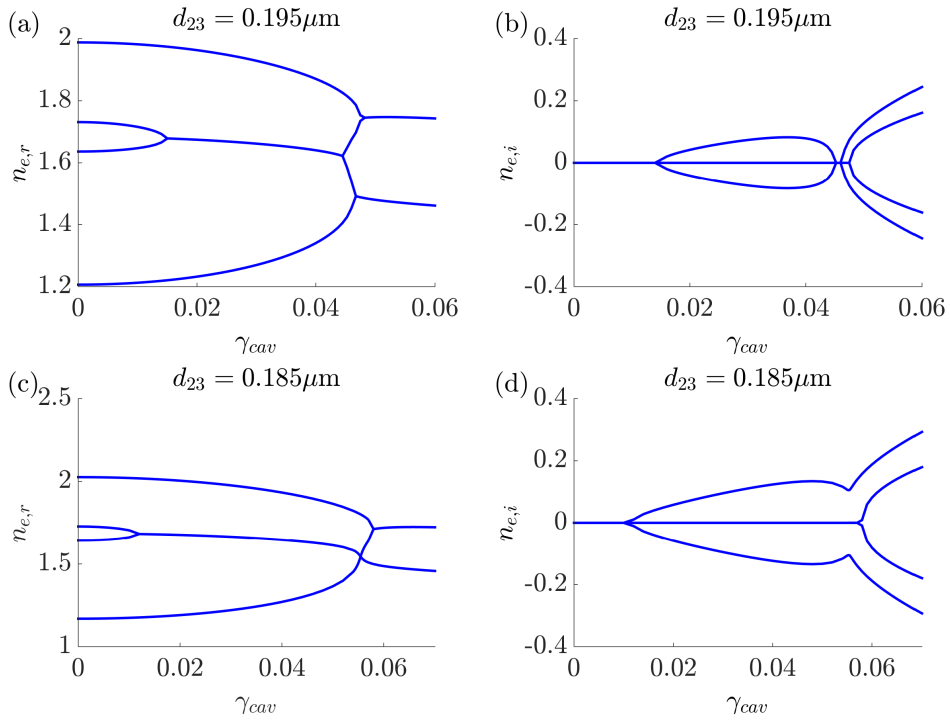

Figure 5.4: (a,c) Real and (b,d) imaginary parts of n_e for the plasmonic structure as a function of γ_{cav} for $d_{23} = 0.195\mu$m (a,b) and 0.185μm (c,d).

5.4(a,b), but now via four coupled plasmonic modes. We observe the overcoupled case in Fig. 5.4(c,d) as in Fig. 5.2(e) with $\alpha > 2.54$. There is no symmetry recovery and mode 2 and 3 merge and stay linked even for large γ_{cav}. This is difficult to observe in Fig. 5.2(e) due to overlapping curves, but is clear in Fig. 5.4(d) due to the non-neighbour interactions. Note that modes 2 and 3 still 'feel' the merging of the other two modes (just before $\gamma_{cav} = 0.06$ in Fig. 5.4(c,d)).

The mode profiles of the four plasmonic supermodes describe the origins of this phenomenon. For $\alpha < 2$ (i.e. relatively large d_{23}, Fig. 5.5 (a,b,c,d)), the two modes with larger (lower) n_e and symmetric (antisymmetric) profiles in the dielectric cavities merge together, as in the typical $\mathcal{PT}$ case (Fig. 5.2(a,b)) (so the first and second mode pair up, just like the third and fourth mode). For $\alpha > 2$ (i.e. relatively small d_{23}, Fig. 5.5(e,f,g,h)), we force coupling between the two central unperturbed modes (so between the second and third mode). This leads to two modes with large fields at the inner (outer) surfaces in Fig. 5.5(e,h) (Fig. 5.5(f,g)). The two modes with large fields on the outer surfaces can 'easily' modify their profile to merge together, and this leads to the first broken phase. For bigger γ_{cav}, they split (Fig. 5.5(i,j,k,l)) again (symmetry recovery), and then later (for even larger γ_{cav}) merge with their original pairing partner. For really small d_{23} the coupling (between the second and third mode) is too strong, so that the first merging is sustained and never splits again (as in Fig. 5.4(c,d)).

This behaviour thus does not depend on the nature of the four coupled modes. It directly stems from the increased coupling between two modes, which were originally not destined to merge, but go through an initial fusion, and eventually return to the typical partner.

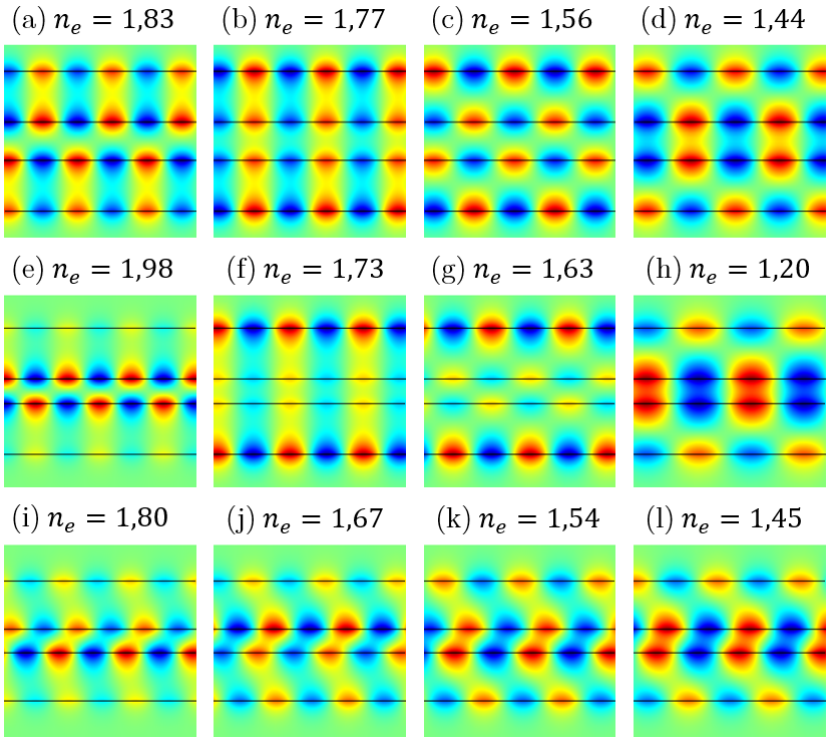

Figure 5.5: The four supermode magnetic field (H_y) profiles for the plasmonic case with (a,b,c,d) $d_{23} = 0.3\mu$m and $\gamma_{cav} = 0$, (e,f,g,h) $d_{23} = 0.195\mu$m and $\gamma_{cav} = 0$, and (i,j,k,l) $d_{23} = 0.195\mu$m and $\gamma_{cav} = 0.046$ (symmetry recovery phase in Fig. 5.4(a,b)).

5.4 Summary

In this chapter, we study theoretically and numerically the mode merging properties in a particular $\mathcal{PT}$-symmetric system of four coupled waveguides. We obtain the analytical condition for which this structure achieves an unusual merging scheme with two distinct unbroken $\mathcal{PT}$ phases. This effect originates from the initial coupling of two modes, which normally remain distinct, but ultimately split again and merge with another, traditional partner mode.

This particular behaviour can appear in systems with multiple modes, as we will also see in Chap. 7, but here we introduce it for the simplest possible structure, and propose dielectric and plasmonic implementations. This recovery of symmetry will be useful in designing novel $\mathcal{PT}$ devices.

6

Broadband unidirectional invisibility

6.1 Introduction

In this chapter, we particularly focus on an important behaviour for one-dimensional $\mathcal{PT}$ structures, the anisotropic transmission resonances (ATRs) [61] or unidirectional invisibility [75, 76]. This means that one obtains unity transmission and zero reflection for incidence from one side of the structure, and a different reflection from the other side (see Sec. 3.2.4). Initially this phenomenon was introduced in tight-binding or Bragg cavity structures [17, 19, 24, 27]. We study this effect next to various other $\mathcal{PT}$ effects in a finite chain of resonators next to a waveguide. Because our geometry is side coupled, the behaviour is very different for the ATRs. Side-coupled structures have already attracted attention in the $\mathcal{PT}$ context for sensor applications [77] (e.g. nanoparticule detection). Our system can also be integrated on-chip, with independent control of the coupling loss (as it is an open system) and the material gain/loss.

We describe the two resonator structure in Sec. 6.2 and its scattering properties in Sec. 6.2.1. We use numerical and analytical calculations with coupled-mode-theory in a transfer and scattering matrix approach to analyze in detail various geometries with multiple cavities. An important parameter for these coherently interacting cavities is the length of the intermediate waveguide, which can be tuned to change the phase and interference properties. The spectrum of two side-coupled resonators (without gain or loss) can exhibit a very narrow transmission peak [78, 79]. We will exploit this peak with $\mathcal{PT}$ symmetry to demonstrate both very narrow and broadband ATRs.

The study of the scattering matrix provides us detailed info on exceptional points and on lasing states in Sec. 6.2.2. Moreover, we address the stability of these systems in Sec. 6.2.3, as the presence of gain can readily make them unstable.

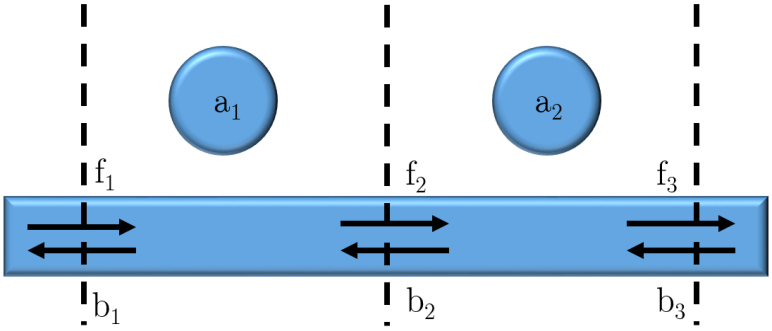

Figure 6.1: Geometry of the two resonator structure. a_1 and a_2 are the mode amplitudes of each resonator. f_i (b_i) denotes the forward (backward) waveguide mode amplitude. The dashed lines separate the two unit cells of the system.

We show the versatility of these systems with a four resonator structure in Sec. 6.3. With four resonators the possible configurations are more numerous, as we can choose between a gain-gain-loss-loss or gain-loss-gain-loss profile, and we can even symmetrically modify the resonance frequencies and the amount of gain/loss, all the while remaining $\mathcal{PT}$-symmetric. We show that these configurations give rise to a unidirectional invisibility scheme with complex behaviour as a function of the frequencies: a rich, tunable dispersion with multiple, crossing ATRs is obtained, offering possibilities for 'ATR engineering'.

This chapter is based on [40].

6.2 Two cavities

The first studied structure is constituted of two resonators coupled next to a waveguide (see Fig. 6.1). We assume that the resonators and waveguide are single mode in the studied frequency region. Furthermore, the resonators are placed sufficiently far from each other so interaction occurs only through the waveguide. Then, the fields in a single unit cell can be described by coupled-mode-theory presented in Sec. 3.2.2:

$$\frac{da_n}{dt} = \left(j\omega_0 - \tfrac{1}{\tau_c} \pm \gamma\right) a_n + df_n + db_{n+1} \tag{6.1}$$

$$f_{n+1} = e^{j\phi} f_n + da_n \tag{6.2}$$

$$b_n = e^{j\phi} b_{n+1} + da_n \tag{6.3}$$

with a_n the complex mode amplitude of the cavity, whereas f_n and f_{n+1} (b_n and b_{n+1}) denote the forward (backward) waveguide mode amplitudes, and $n = 1, 2$. The coupling time to the waveguide is τ_c, and the resonance frequency of the cavities is ω_0. Here $d = je^{j\phi/2}/\sqrt{\tau_c}$, where ϕ depends on the length of the intermediate waveguide and plays a major role in the phase and interference characteristics. Finally, when $\gamma > 0$ it defines the amount of gain ($+\gamma$) or loss ($-\gamma$) present in the nth resonator, and vice versa when $\gamma < 0$. We mean here inherent gain or loss of the resonator via e.g. external pumping of a gain medium, or material absorption.

For a two resonator structure $\mathcal{PT}$ symmetry requires that one cavity supports gain and the other loss (see Sec. 2.2.1). The amplitudes are normalized so that $|a_n|^2$ is equal to the total power in the resonator n, and $|f_n|^2$ ($|b_n|^2$) is the power in the forward (backward) mode of the waveguide at position n. As we mainly work in the continuous wave regime, the temporal dependence of the solution is $e^{j\omega t}$ and we can replace the time derivative d/dt by $j\omega$ with ω the excitation frequency and j the imaginary unit. In this side-coupling scheme, without gain or loss, there is a strong reflection on resonance. Note that these equations are equivalent to a model of a ring resonator next to two waveguides [80].

6.2.1 Reflection and transmission

We first examine the asymmetric reflection properties. A direct transfer-matrix approach is employed (see Sec. 3.2.4), which is much more resource efficient than a time-domain one, but is insensitive to the stability (stability is studied in Sec. 6.2.3). The transfer-matrix for one cavity can be written as:

$$\begin{aligned}\begin{pmatrix} b_n \\ f_n \end{pmatrix} &= \begin{pmatrix} e^{j\phi} - \frac{d^2}{j(\omega_0-\omega)\pm\gamma} & \frac{-d^2 e^{-j\phi}}{j(\omega_0-\omega)\pm\gamma} \\ \frac{d^2 e^{-j\phi}}{j(\omega_0-\omega)\pm\gamma} & e^{-j\phi} + \frac{d^2 e^{2j\phi}}{j(\omega_0-\omega)\pm\gamma} \end{pmatrix} \begin{pmatrix} b_{n+1} \\ f_{n+1} \end{pmatrix} \\ &= M_\pm \begin{pmatrix} b_{n+1} \\ f_{n+1} \end{pmatrix}\end{aligned} \tag{6.4}$$

The transfer-matrix for the entire system M_{tot} is obtained by multiplication. As our scattering system is $\mathcal{PT}$-symmetric, we can use the formalism of [61] and define the total transfer-matrix as a function of three real parameters (B and the phase and amplitude of A) via:

$$M_{tot} = M_- M_+ = \begin{pmatrix} A^* & jB \\ -jC & A \end{pmatrix} \tag{6.5}$$

with C given by $C = (|A|^2 - 1)/B$ and M_- (M_+) denotes the transfer-matrix for the cavity with loss (gain). Finally, we can obtain the scattering-matrix from the total transfer-matrix:

$$S = \frac{1}{A} \begin{pmatrix} jB & 1 \\ 1 & jC \end{pmatrix} = \begin{pmatrix} r_L & t_c \\ t_c & r_R \end{pmatrix} \tag{6.6}$$

with r_L and r_R the left and right reflection coefficient and t_c the transmission coefficient. This matrix is $\mathcal{PT}$-symmetric for our particular system (Eq. (6.4) and on), meaning that S satisfies the symmetry relation $(\mathcal{PT})S(\omega^*)(\mathcal{PT}) = S^{-1}(\omega)$ with $\mathcal{P} = \left(\begin{smallmatrix} 0 & 1 \\ 1 & 0 \end{smallmatrix}\right)$ and $\mathcal{T}$ the complex conjugation operator. From S we can extract all the information, such as the reflection with input from the left side $R_L = |r_L|^2$, the reflection from the right side $R_R = |r_R|^2$ and the transmission $T = |t_c|^2$. The transmission is the same regardless of the input side because of reciprocity.

We calculate the transmission for a loss-gain structure as a function of the normalized frequency detuning $(\omega - \omega_0)\tau_c$ (see Fig. 6.2). We observe the typical spectrum of two side-coupled resonators for three different phases ϕ with the normalized gain/loss factor $\gamma\tau_c = 0$ (without gain or loss, Fig. 6.2(a)). The transmission reaches zero (and reflection reaches unity) at the resonance frequency ω_0.

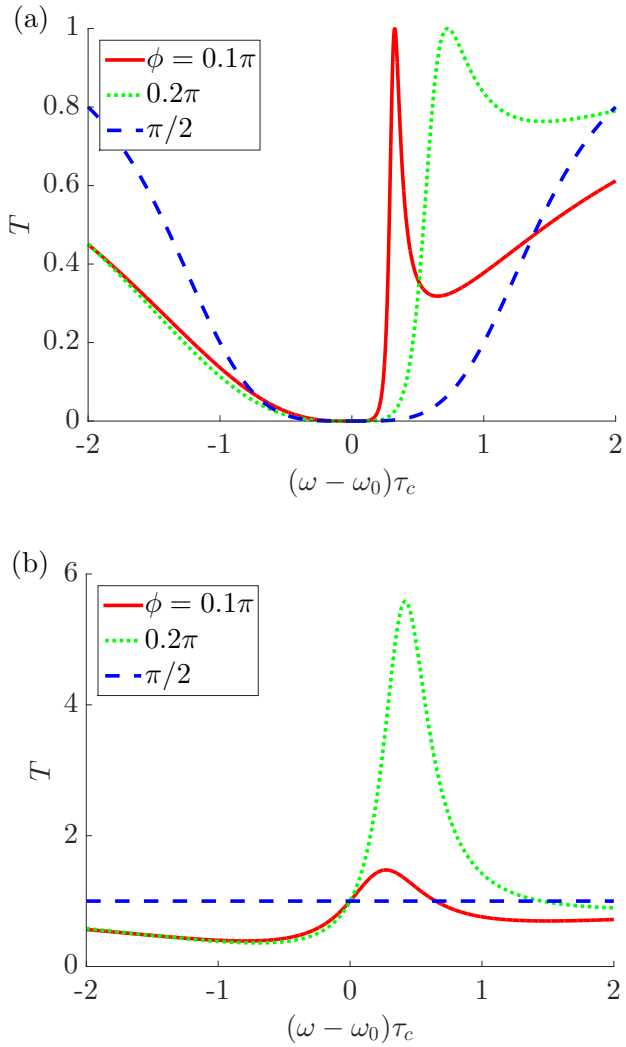

Figure 6.2: Transmission of the two resonator structure as a function of the detuning $(\omega - \omega_0)\tau_c$ with three different values of ϕ, (a) for $\gamma\tau_c = 0$ and (b) for $\gamma\tau_c = 1$.

In addition, due to the cavity interaction, there is a narrow transmission peak (reaching $T = 1$) for small values of ϕ in the high reflection band. This peak becomes narrower and closer to $\omega = \omega_0$ as ϕ tends to 0. As we will see, the ATRs of these structures will directly originate from the extension of this particular peak for $\gamma\tau_c \neq 0$. We note in passing that these line shapes are reminiscent of Fano resonances, which show up as interferences between a broadband and a narrowband feature [81].

When $\gamma\tau_c$ is equal to 1 (Fig. 6.2(b)), the zero transmission zone around ω_0 tends to disappear. However, information about the ATRs requires the examination of the left and right side reflection, as they are no longer the same for $\gamma\tau_c \neq 0$. Therefore we analyze the left and right reflection R together with the transmission T as a function of the detuning and $\gamma\tau_c$ for a loss-gain structure (Fig. 6.3). In these figures, left and right incidence corresponds to $\gamma\tau_c > 0$ and < 0, respectively (the right and left halves of the graphs).

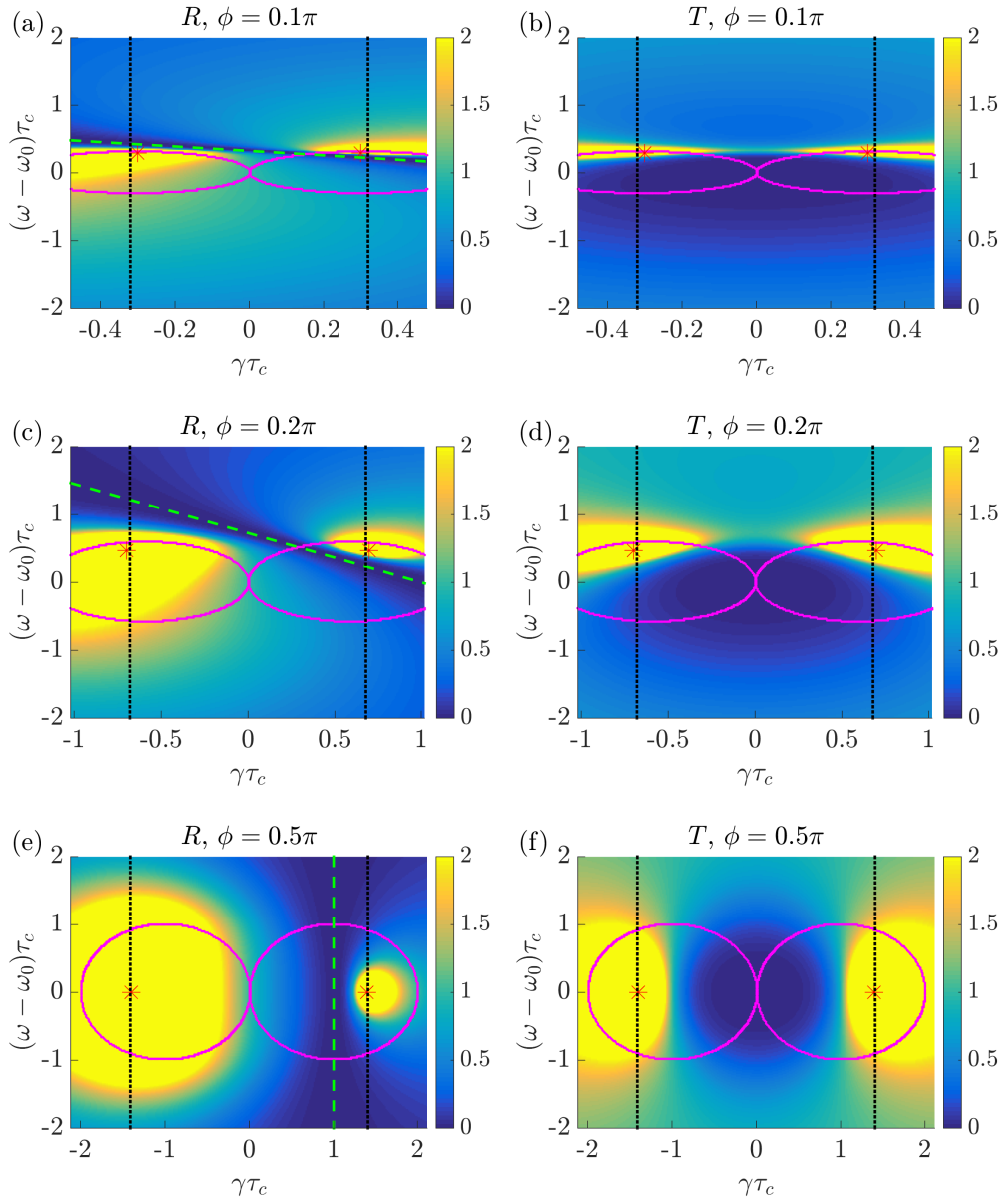

Figure 6.3: Reflection (left column) and transmission (right column) for the two resonator structure (loss-gain) as a function of $\gamma\tau_c$ and detuning $(\omega - \omega_0)\tau_c$, and saturated to two for clarity. (a,b) For $\phi = 0.1\pi$, (c,d) 0.2π and (e,f) $\pi/2$. $\gamma\tau_c > 0$ (< 0) is for left (right) incidence. The green dashed lines represent the ATRs. The vertical black dotted lines represent the stability limit (see Sec. 6.2.3). The red stars indicate the lasing states and the magenta elliptical curves represent the exceptional points.

The range $0 < \phi \leq \pi/2$ already presents all behaviours. The vertical black dotted lines indicate the maximum $\gamma\tau_c$ for stability, which is discussed in Sec. 6.2.3. Note that the transmission remains symmetric, the graphs for $\gamma\tau_c > 0$ and < 0 are the same. However, the asymmetry between the left and right reflection is present for every value of ϕ. The ATRs arise when the reflection from a specific side reaches zero (dark blue zones in Fig. 6.3(a,c,e), indicated with green dashed lines).

Interestingly, for fixed $\gamma\tau_c$, the sharpness of the zero reflection minimum is narrower as ϕ decreases. Thus, the frequency range of the ATRs is wider when ϕ increases, and becomes very broadband for $\phi = \pi/2$ (see Fig. 6.3(e)), which will be limited in practice by effects such as waveguide and material dispersion. This behaviour is in line with the transmission resonances observed for $\gamma\tau_c = 0$ (Fig. 6.2(a)). Note also that R and T are symmetric around $\omega = \omega_0$ for the special case of $\phi = \pi/2$.

ATRs arise when $T = 1$ (see Sec. 3.2.4), so with $|t_c|^2 = |1/A|^2 = 1$, we find an analytical condition for ATRs in this system:

$$(\omega - \omega_0)\tau_c = (1 - \tau_c\gamma)\tan\phi \tag{6.7}$$

which is the equation of a straight line (green dashed lines in Fig. 6.3). This line is anchored at the point $\omega = \omega_0$ and $\gamma\tau_c = 1$ and has a slope of $-\tau_c \tan\phi$. Therefore with $\phi = \pi/2$ the slope indeed becomes infinite and we observe the broadband ATR of Fig. 6.3(e).

As T is symmetric around $\gamma\tau_c = 0$, one finds another line where $T = 1$, symmetric to the previously indicated ATR lines (dashed green lines). This line indicates the ATRs if we had chosen a gain-loss structure, instead of loss-gain, so this is not a 'different' ATR. In that case, R should be mirrored in Fig. 6.3.

Finally, we also observe that there tends to be more reflection when incidence is from the gain side than from the loss side, as indeed the yellow zones are larger on the left of Fig. 6.3(a,c,e).

We conclude that the two resonator system already presents a fairly complex behaviour of asymmetric scattering properties, deriving from the passive transmission resonances. The geometry can achieve both very narrow or broadband ATRs just by varying the length of the intermediate waveguide.

We remark that the model neglects some effects that can influence the results for specific applications and intensities. First, dispersion will ultimately limit the broadband ATRs to a finite range of frequencies. For waveguide dispersion the geometry and materials could offer degrees of freedom to optimize the available range, for example with photonic crystal waveguide engineering. Material dispersion will also impact the ATR range, certainly via the finite window of active materials. We also note that the complex permittivity of the materials will follow the Kramers-Kronig relations, which can distort the characteristics. Second, gain saturation and charge carrier dynamics in the gain material will limit the maximal $\gamma\tau_c$ that can be reached in practice. Third, the large intensities around the lasing states will break the linear approximation, and may lead to new carrier and nonlinear effects, temporal instabilities [82], switching behaviour and so on. The latter phenomena are expected mainly around the stability threshold, so below the gain values for the discussed ATRs.

6.2.2 Lasing states and exceptional points

Another interesting feature of active structures is the lasing states that can arise from the presence of gain. These states can be derived from the scattering matrix (Eq. (6.6)), as T, R_L and R_R become infinite when $A = 0$, leading to:

$$(\omega - \omega_0)\tau_c = -j\left(1 + e^{-j\phi}\sqrt{e^{2j\phi}\tau_c^2\gamma^2 + 1}\right) \tag{6.8}$$

Lasing states require a purely real frequency. Therefore the left side of this equation has to be purely real, so the lasing states exist only when the imaginary part of the right side is equal to zero, which we indicate with red stars in Fig. 6.3. Within the numerical accuracy these points are at the stability limit (vertical black dotted lines in Fig. 6.3, discussed in detail in Sec. 6.2.3). The two cavity structure has two lasing states, but they are exactly at the same detuning and gain/loss, which is understandable as T is reciprocal, so there is left-right symmetry in Fig. 6.3(b,d,f).

Furthermore, as the S-matrix respects $\mathcal{PT}$ symmetry, there is a broken and an unbroken $\mathcal{PT}$ phase. As we have discussed in Sec. 3.2.4, in the unbroken phase each S-matrix eigenstate is mapped back to itself under the $\mathcal{PT}$ operation, whereas in the broken phase they are mapped to each other. The two eigenstates merge at the boundary of these phases which are called the exceptional points. To identify these phases one can examine the eigenvalues of S [61], which have unity module only in the unbroken phase. Alternatively, one can use the quantity $(R_L + R_R)/2 - T$, which is below (above) unity in the unbroken (broken) phase, respectively. When this quantity is equal to one, it describes the boundary between the two phases, shown as the magenta elliptical lines in Fig. 6.3. We observe that the lasing states only appear in the broken phase (inside the magenta lines) in accordance with [62].

Thus, as in other $\mathcal{PT}$ devices, the two side-coupled resonator structure presents lasing states and a broken $\mathcal{PT}$ phase. In our model the particular states are fairly straightforward to determine analytically.

6.2.3 Stability

The main advantage of this structure concerns the versatility of the scattering properties. However, a stationary transfer-matrix formalism fails to take into account a possible instability of the system, which is common in the presence of gain [73]. Therefore, we analyse the stability range, via the matrix H that describes the system without external excitation:

$$\frac{d}{dt}\begin{pmatrix} a_1 \\ a_2 \end{pmatrix} = H\begin{pmatrix} a_1 \\ a_2 \end{pmatrix} \tag{6.9}$$

with:

$$H = \begin{pmatrix} j\omega_0 - 1/\tau_c - \gamma & d^2 \\ d^2 & j\omega_0 - 1/\tau_c + \gamma \end{pmatrix} \tag{6.10}$$

where the first resonator supports loss and the second supports gain ($\gamma > 0$ here). Unlike the S-matrix, H is neither Hermitian nor $\mathcal{PT}$-symmetric due to the coupling with the waveguide. The energy contained in the resonators and the intermediate

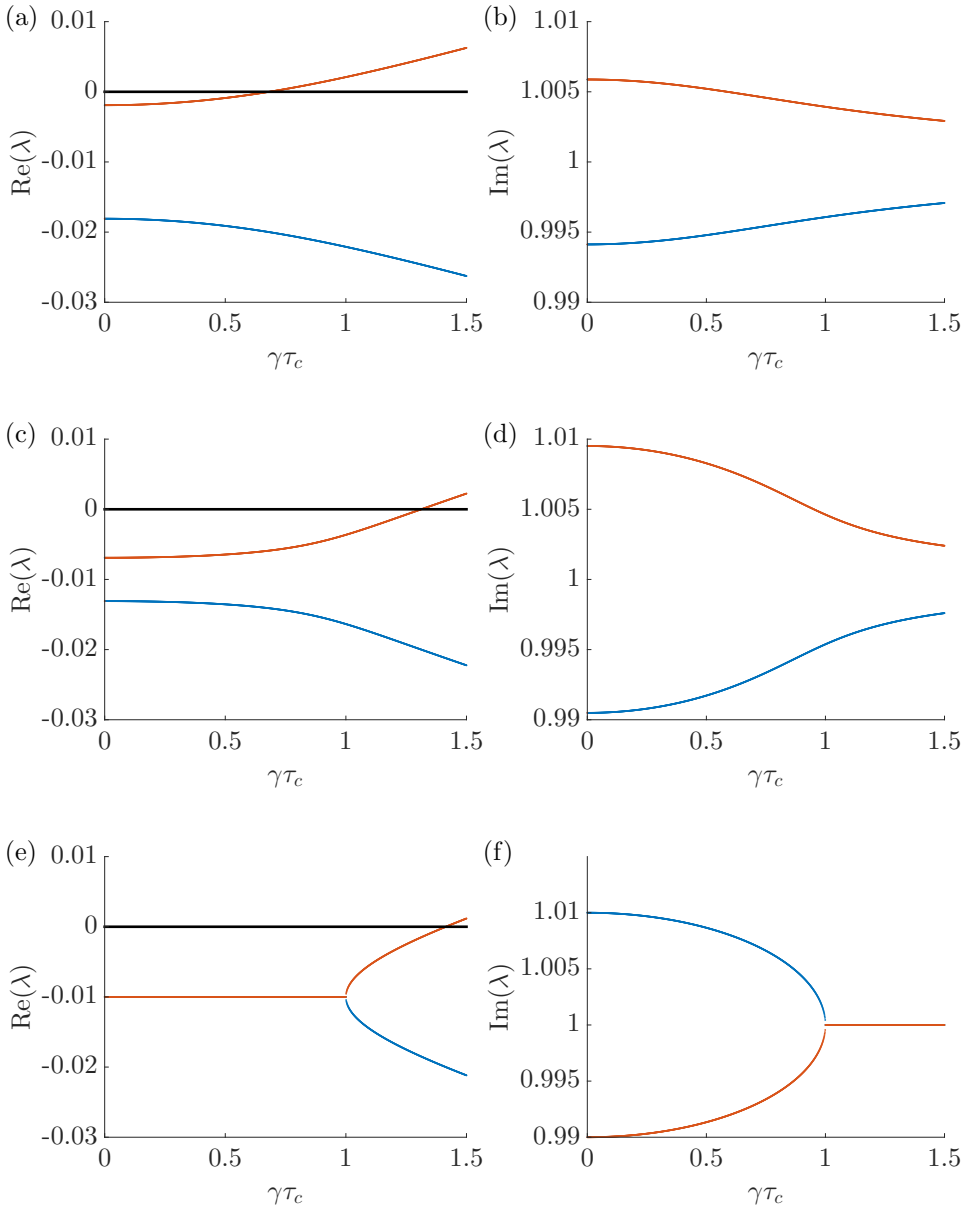

Figure 6.4: Real (left column) and imaginary (right column) part of the eigenvalues $\lambda_{1,2}$ as a function of $\gamma\tau_c$ for (a,b) $\phi = 0.2\pi$, (c,d) 0.4π and (e,f) $\pi/2$. The black horizontal line in the left column marks $\mathrm{Re}(\lambda) = 0$, the instability threshold.

waveguide flows out of the system. The eigenvalues λ of H describe the evolution of the collective eigenstates:

$$\lambda_{1,2} = \left(j\omega_0 - \frac{1}{\tau_c}\right) \pm \sqrt{\gamma^2 + \frac{e^{2j\phi}}{\tau_c^2}} \tag{6.11}$$

The imaginary part of these eigenvalues represents the eigenfrequency of the modes. The real part represents the time evolution of the total power inside the two cavity system.

We plot λ as a function of $\gamma\tau_c$ (Fig. 6.4) for three values of ϕ. Without gain or loss ($\gamma\tau_c = 0$), the two eigenvalues have a negative real part (see Fig. 6.4(a,c,e)), which means that the total power present in the cavities is flowing out of the system through the waveguide.

Remark that even though we are not describing a pure $\mathcal{PT}$-symmetric structure here, we observe similar curve shapes, especially for $\phi = \pi/2$ (Fig. 6.4(e,f)). The imaginary parts of the eigenvalues merge together, whereas the two real parts split beyond a particular point, which thus looks like an exceptional point (at $\gamma\tau_c = 1$). As ϕ decreases, this behaviour looks less and less like 'perfect' $\mathcal{PT}$, which is comparable to a directional $\mathcal{PT}$ coupler with unequal waveguides (Fig. 6.4(a,b) and Fig. 6.4(c,d)).

For stability, we focus on the real part of the eigenvalues. When one is positive, it shows us that the power inside the cavities grows exponentially with time. When $\gamma\tau_c$ increases, one of the modes always reaches a point where its real part becomes positive (e.g. at $\gamma\tau_c \approx 0.7$ in Fig. 6.4(a)), leading to unstable behaviour that ultimately will become nonlinear and requires other modeling approaches.

We check the previous with time domain simulations of R and T as a function of the detuning $(\omega - \omega_0)\tau_c$ and $\gamma\tau_c$ (see Fig. 6.5). The boundary between the stable and the unstable regime is well described by the zero of the real part of the eigenvalue (vertical black lines in Fig. 6.5), and corresponds with an exponential growth in the time domain results. Thus, for each configuration we can define a maximum limit for $\gamma\tau_c$ beyond which the system is unstable, defining a valid range of gain/loss.

6.3 Four cavities

We further show the versatility of these systems with a four cascaded resonator geometry (see Fig. 6.6). We skip the three cascaded resonator system as it offers less degrees of freedom and behaviours. We use the same formalism as in the previous section. In principle most results can be analytically derived, but the equations become unwieldy, so calculations are more convenient.

The transmission T of a four resonator structure without loss/gain for four values of ϕ is shown in Fig. 6.7. Typically there are three peaks with $T = 1$ (and $R = 0$) for four resonators. For $\phi = 0.1\pi$ the three peaks are relatively close to each other around $\omega_0 = \omega$. When ϕ increases the three peaks move to the right, and the rightmost peak (number 3) tends to infinite detuning when ϕ reaches $\pi/4$. Beyond this value of ϕ peak 3 appears from minus infinity and continues moving to the right. Finally, when ϕ reaches $\pi/2$, peak 2 also moves to infinite detuning. This pattern continues as ϕ increases. As previously the ATRs of the $\mathcal{PT}$-symmetric system will originate from the behaviours of these three peaks.

We calculate the reflection and transmission with a loss-gain-loss-gain profile for three phases (Fig. 6.8). We observe two kinds of ATRs. There is a straight line ATR where the reflection is zero (slanted green line in Fig. 6.8(a,c,e)), but for only one incidence direction. This line originates from the second peak with $T = 1$ in Fig. 6.7 and can be compared to the ATR line of the two resonator structure (green dashed line in Fig. 6.3(a,c,e)). This ATR becomes very broadband (Fig. 6.8(e)) when peak 2 goes to infinite detuning.

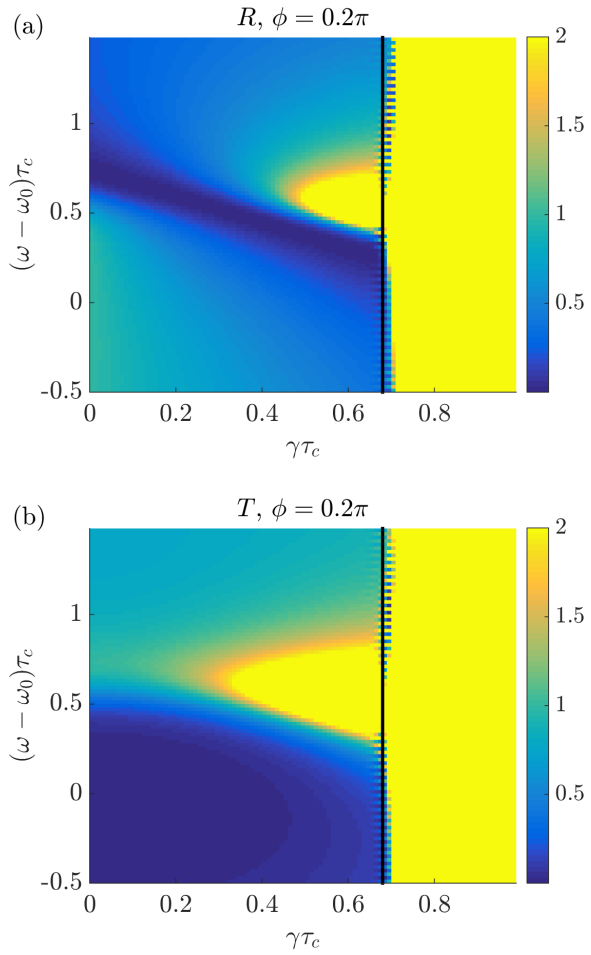

Figure 6.5: (a) Left reflection and (b) transmission as a function of the detuning and $\gamma\tau_c$ for a loss-gain structure. The parameters are the same as in Fig. 6.2. These values are calculated with time domain simulations and are saturated to two for clarity. The black lines mark when one of the eigenvalues begins to have a positive real part (around $\gamma\tau_c \approx 0.7$ in Fig. 6.4(a)).

Additionally, there is an ATR where $R_R = R_L = 0$ and $T = 1$, which originates from peaks 1 and 3 (nearly horizontal green line in Fig. 6.8(a) and green ellipse in Fig. 6.8(c,e)). This indicates a 'doubly accidental' degeneracy [61] where both reflections are equal to zero, so the structure is transparent from both directions. This can appear due to extra tuning parameters, but seems inherent in our geometry. The latter type of ATR would actually better be described as an 'isotropic' transmission resonance. We can observe that the ellipse becomes infinitely large (Fig. 6.8(a)) as peak 3 goes to infinity (for $\phi = \pi/4$), so we only observe a horizontal line close to $(\omega - \omega_0)\tau_c = 0.5$.

The structure also exhibits two lasing states at the limit of the stable range. There are two additional lasing states but they lie deeper into the unstable part. The exceptional point boundaries are also more complicated, with four zones instead of two for the two resonator structure (magenta curves in Fig. 6.8). As in Fig. 6.3, we observe that the reflection tends to be stronger when the incidence is from the gain side (larger yellow areas on the left side of R).

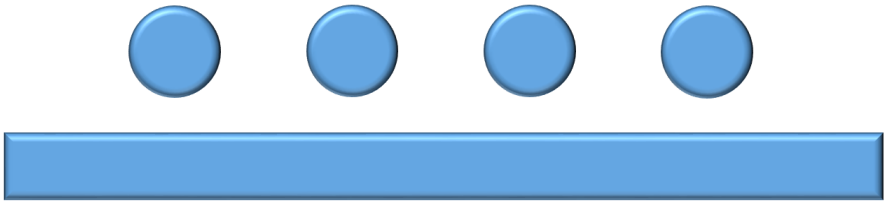

Figure 6.6: Geometry of the four resonator structure.

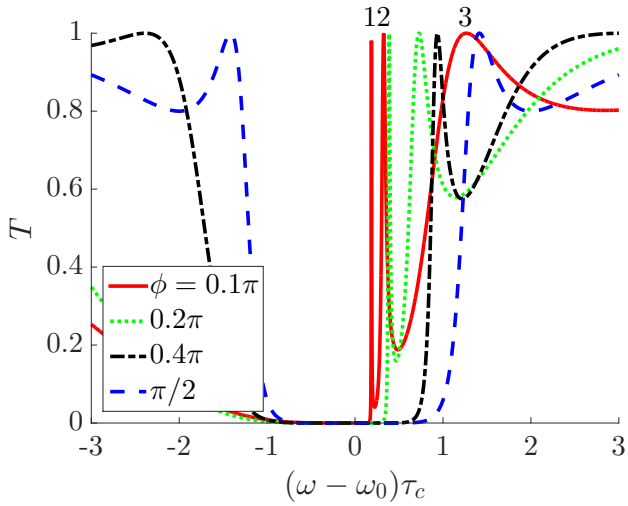

Figure 6.7: Transmission of the four resonator structure as a function of the detuning $(\omega - \omega_0)\tau_c$ for $\gamma\tau_c = 0$ with four different values of ϕ. The three numbers indicate the three peaks with $T = 1$ for $\phi = 0.1\pi$.

The degrees of liberty for this structure are numerous as we are only limited by the $\mathcal{PT}$ symmetry relation $n(x) = n^*(-x)$. For example, if we change the elements symmetrically, we can vary the gain/loss profile (such as loss-loss-gain-gain instead of loss-gain-loss-gain), the resonance frequencies of the cavities (ω_1 has to equal ω_4, and ω_2 has to equal ω_3, but the couples can differ), the amount of gain/loss in the cavities, and the phase ϕ. We describe succinctly a few examples (Fig. 6.9) where we observe rich possibilities for the ATRs, the exceptional points and the lasing states.

As a first example, we examine a loss-loss-gain-gain profile, in contrast with the previous loss-gain-loss-gain design. The reflection graph with ATRs and exceptional points is qualitatively different (Fig. 6.9(a)), with for example two pairs of lasing states, in contrast with the single pair in Fig. 6.8 (and in particular with Fig. 6.8(e) for the same phase).

In the other examples we return to a loss-gain-loss-gain profile, but we change the gain/loss values. In Fig. 6.9(b) with a gain/loss sequence $(-0.3\gamma, \gamma, -\gamma, 0.3\gamma)$, we observe an interaction between the line and ellipse of ATRs of Fig. 6.8(c), which looks similar to 'anti-crossing' behaviour. In Fig. 6.9(c) the structure has a gain/loss sequence $(-0.01\gamma, \gamma, -\gamma, 0.01\gamma)$ leading to another qualitative change of the ATRs, specifically the elliptical ATR of Fig. 6.8(d) becomes a parabola in Fig. 6.9(c). Furthermore, the change of the exceptional points is even more

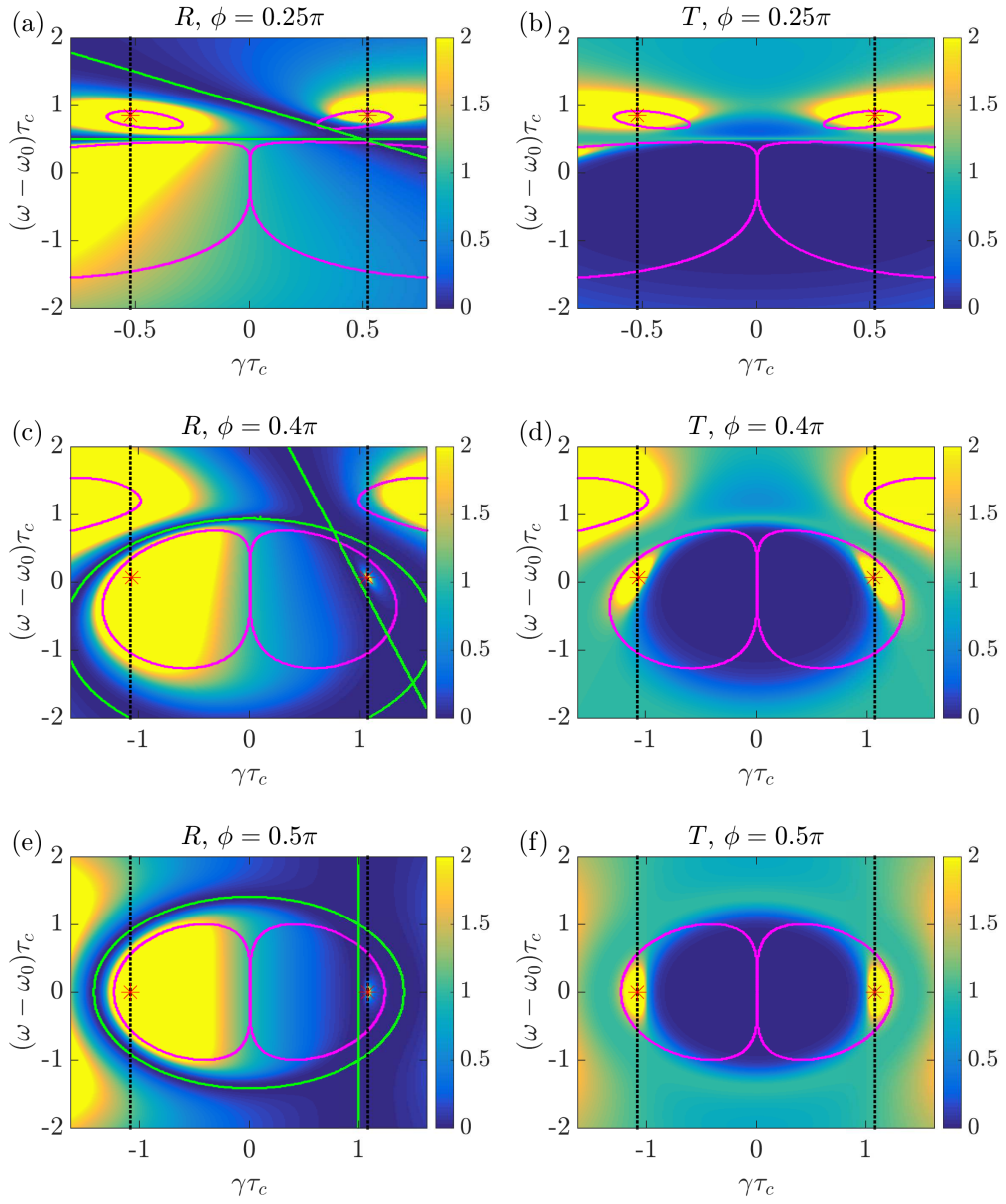

Figure 6.8: Reflection (left column) and transmission (right column) for four resonators (loss-gain-loss-gain) as a function of $\gamma\tau_c$ and the detuning $(\omega - \omega_0)\tau_c$, and saturated to two for clarity. For (a,b) $\phi = \pi/4$, (c,d) 0.4π and (e,f) $\pi/2$. $\gamma\tau_c > 0$ (< 0) is the reflection and transmission for left (right) incidence. The black dotted lines represent the stability limit. The green lines show the ATRs, the red stars indicate the laser states and the magenta curves represent the limits of the broken symmetry phase.

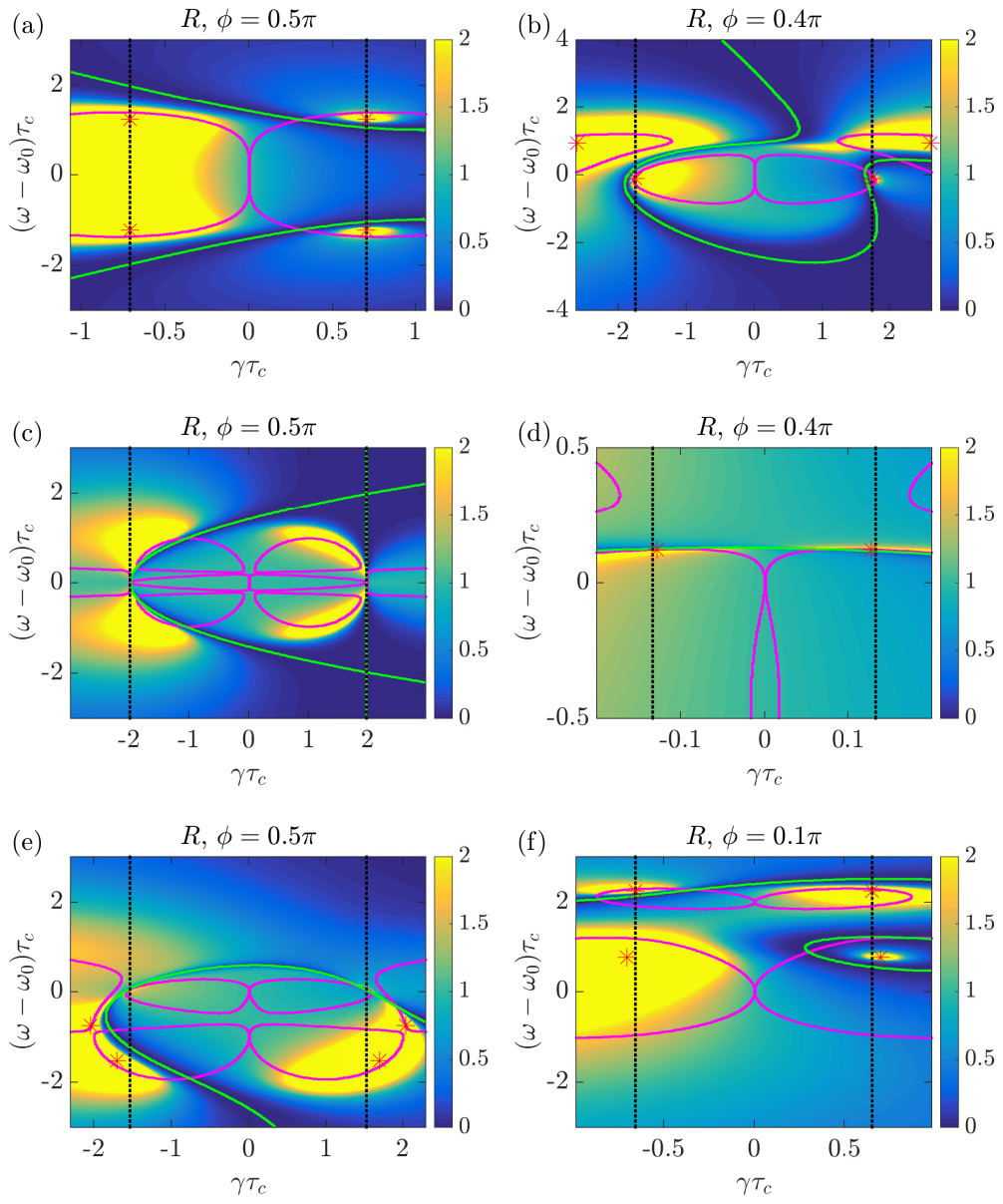

Figure 6.9: Reflection for various four resonator structures as a function of $\gamma\tau_c$ and the detuning $(\omega - \omega_0)\tau_c$, and saturated to two for clarity. (a) Loss-loss-gain-gain structure with resonance frequency sequence $(\omega_0, \omega_0, \omega_0, \omega_0)$ and gain/loss sequence $(-\gamma, -\gamma, \gamma, \gamma)$. The other structures are loss-gain-loss-gain with sequences (b) $(\omega_0, \omega_0, \omega_0, \omega_0)$ and $(-0.3\gamma, \gamma, -\gamma, 0.3\gamma)$, (c) $(\omega_0, \omega_0, \omega_0, \omega_0)$ and $(-0.01\gamma, \gamma, -\gamma, 0.01\gamma)$, (d) $(\omega_0, \omega_0 - 1/\tau_c, \omega_0 - 1/\tau_c, \omega_0)$ and $(-\gamma, \gamma, -\gamma, \gamma)$, (e) $(\omega_0, \omega_0 - 1/\tau_c, \omega_0 - 1/\tau_c, \omega_0)$ and $(-0.1\gamma, \gamma, -\gamma, 0.1\gamma)$ and (f) $(\omega_0, \omega_0 + 2/\tau_c, \omega_0 + 2/\tau_c, \omega_0)$ and $(-\gamma, 0.5\gamma, -0.5\gamma, \gamma)$. Vertical black dotted lines are stability limits, green lines are ATRs, red stars are lasing states, magenta lines indicate exceptional points.

complicated.

As another example we change the resonance frequencies, while keeping $\mathcal{PT}$ symmetry. For Fig. 6.9(d) we use the frequencies $(\omega_0, \omega_0 - 1/\tau_c, \omega_0 - 1/\tau_c, \omega_0)$, but with the standard gain/loss $(-\gamma, \gamma, -\gamma, \gamma)$. We observe a very flat and narrow ATR, similar to the nearly horizontal ATR of Fig. 6.8(a). But here the reflection is zero for only one incidence direction (the green curve is very slightly slanted in Fig. 6.9(d)), and we are not in the 'doubly accidental' degeneracy case of Fig. 6.8(a).

For the final examples we change both resonance frequency and gain/loss sequences. For Fig. 6.9(e) we use the frequencies $(\omega_0, \omega_0 - 1/\tau_c, \omega_0 - 1/\tau_c, \omega_0)$ and the gain/loss sequence $(-0.1\gamma, \gamma, -\gamma, 0.1\gamma)$. We observe a similar interaction between the ATR line and ellipse as in Fig. 6.9(b), but mirrored as a function of detuning. In comparison, there are also two more broken symmetry zones. Finally, Fig. 6.9(f) with $(\omega_0, \omega_0 + 2/\tau_c, \omega_0 + 2/\tau_c, \omega_0)$ and $(-\gamma, 0.5\gamma, -0.5\gamma, \gamma)$ shows another behaviour, and can barely be compared to previous cases.

One observes that the number of possible configurations and behaviours quickly grows with the number of cavities. Thus a particular desired behaviour can be targeted via the analytical model for a relatively small number of cavities.

6.4 Summary

In this chapter we introduce a new $\mathcal{PT}$ geometry consisting of side-coupled cavities with interesting unidirectional characteristics. In these systems we show that the bandwidth can be uniquely tuned to be particularly broad or narrow, via a simple structural parameter (the length of waveguide between the cavities). The unidirectional effect is one of the most salient features in the $\mathcal{PT}$ field; it is strongly researched nowadays for potential applications and will also be approached in Chap. 7. The proposed design can be implemented on-chip in various ways, for example using photonic crystal cavities or ring resonators.

With a compact, physical model we have analyzed in detail the scattering characteristics of the one-dimensional structures with side-coupled resonators. Because of side-coupling the behaviour is very different from typical tight-binding or Bragg defect structures. It is also an analytically tractable open system with flexible control of cavity-waveguide coupling and the intrinsic gain and loss.

The spectrum of two resonators (without gain or loss) exhibits a very narrow transmission ($R = 0$) peak. With added gain and loss the ATRs originate precisely from this peak, which can be tuned by the length of the intermediate waveguide, in order to demonstrate very narrow or broadband ATRs. Moreover, the study of the scattering matrix provides us detailed info on related important properties, such as the lasing states, the exceptional points, and the stability of the system.

Furthermore, the versatility of these systems is exhibited with a chain of four resonators. The possible degrees of freedom are numerous, as we can choose between a gain-gain-loss-loss or gain-loss-gain-loss profile, and we can even symmetrically modify the frequencies of the resonators and the amount of gain and loss. Each of these configurations gives rise to a unidirectional (or bidirectional) invisibility scheme with complex behaviour as a function of the frequencies: a

rich, tunable dispersion with multiple, crossing or anti-crossing ATRs is obtained, offering possibilities for 'ATR engineering'.

In future work one could also explore structures without perfect $\mathcal{PT}$ geometry, with e.g. gain/loss profiles that are not left-right symmetric. These would often lead to imperfect ATRs, however, with reflections that are not perfectly zero. We do not explore these cases here, but they would significantly expand the available parameter space. Furthermore, Bragg gratings with non-linearity have also demonstrated robust ATRs with non-reciprocal transmission [75], we can expect to find the same effect in our system if we add non-linearity, for example via material non-linearities in the resonators [64, 82].

7

Topological edge modes with $\mathcal{PT}$ symmetry

7.1 Introduction

Topology examines the conservation of mathematical or physical properties under continuous deformations. It expanded towards the development and comprehension of topological insulators [83], and it opens opportunities in many fields and in particular in photonics [84]. One of the intriguing promises is a unidirectional waveguide that allows light to travel through an imperfect structure without suffering from back-reflection. Topological effects are available in many photonic systems, for example in photonic crystals, coupled resonators, metamaterials and quasi-crystals [85]. In particular, 1D quasi-periodic structures [86–88] with or without a defect [89] have a proven interest as a topological playground [90].

$\mathcal{PT}$ symmetry has been employed to obtain topological states [91–93], or to tailor such states [94, 95] within a 1D structure. We have seen, in Sec. 2.2.3, that $\mathcal{PT}$ symmetry or non-Hermitian photonics can create states with similar properties as topology. In this chapter, we associate $\mathcal{PT}$ symmetry and topology in a 1D quasi-crystal device to observe their intriguing combined characteristics.

We consider as a model system a quasi-crystal consisting of two abutted Fibonacci sequences presenting topological edge modes, recently introduced for the passive regime [96, 97]. We portray this passive structure in Sec. 7.2, with a calculation of its transmittance and an interpretation of its intrinsic topological properties.

Subsequently we add gain and loss in Sec. 7.3, in order to investigate the global (Sec. 7.3.1) or local (Sec. 7.3.2) interplay between $\mathcal{PT}$- and topology-related characteristics. With the capabilities of $\mathcal{PT}$ symmetry to act on bandgaps, we

examine how gain and loss affect edge modes that are lying inside the gaps. We present the curious mode-merging behaviours displayed by the different types of modes in this quasi-crystal when $\mathcal{PT}$ symmetry is added. Among other typical $\mathcal{PT}$-phenomena, for example, the symmetry recovery effect presented in Chap. 5 appears. In addition, as in other 1D $\mathcal{PT}$ structures, we detect the anisotropic transmission resonances (ATRs) presented in Chap. 6 but in a much more complex pattern than previously noticed. Furthermore, due to the presence of gain, we get a family of lasing resonances, that we are able to describe with a simple Fabry-Perot model in Sec. 7.3.3. Possibilities are suggested for engineering the lasing spectrum (gain-frequency relation at threshold).

This chapter is based on the work published in [98].

7.2 Topological Fibonacci sequence

We study the scattering properties of an open 1D photonic quasi-crystal structure composed of two parts stitched together. In this section, we examine only the passive properties (no gain or loss). The two parts are Fibonacci sequences, which are quasi-periodic and composed of an alternation of two letters A, B, representing two different materials (Fig. 7.1(a)).

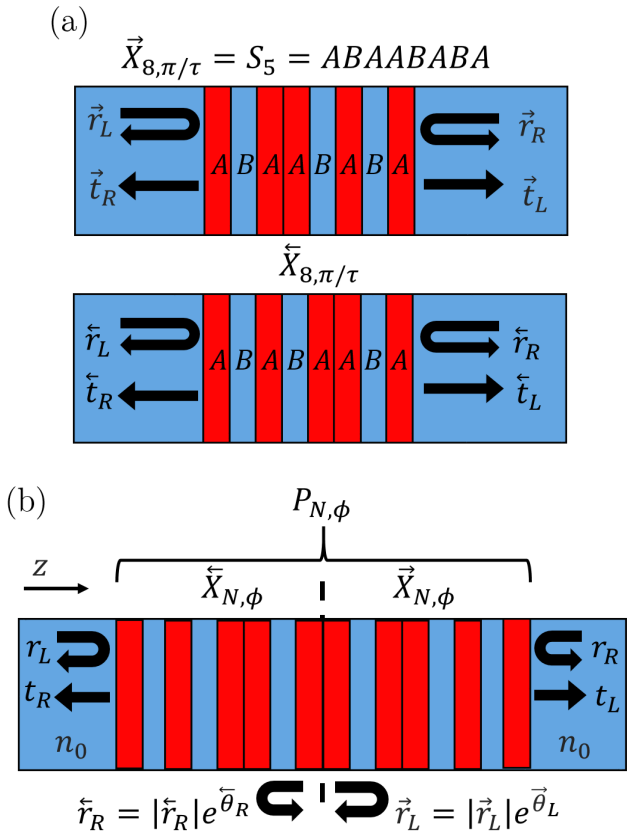

Figure 7.1: (a) Geometry of the Fibonacci sequences $\overleftarrow{X}_{N,\phi}$ and $\overrightarrow{X}_{N,\phi}$ with their implementations into a photonic quasi-crystal. (b) Geometry of the structure $P_{N,\phi}$ with the convention for the right/left transmission and reflection.

The traditional mechanism to generate a Fibonacci sequence is by using an inflation/substitution algorithm σ. σ applies onto A, B according to $\sigma(A) = AB$ and $\sigma(B) = A$, and its application onto more than one letter obeys the relation $\sigma(YZ) = \sigma(Y)\sigma(Z)$ (e.g. $\sigma(AB) = \sigma(A)\sigma(B) = ABA$). Consecutive applications of σ gives rise to a Fibonacci sequence $S_j = \sigma^j(B)$ (with $j \in \mathbb{N}$), whose length is the Fibonacci number $F_{j>1} = F_{j-1} + F_{j-2}$ (with $F_0 = F_1 = 1$). When $j \to \infty$ the ratio $F_{j+1}/F_j \to \tau$ with $\tau = (1 + \sqrt{5})/2$ the golden ratio [63]. The infinite chain $S_\infty \equiv \lim_{j\to\infty} S_j$ is quasi-periodic and self-similar under the substitution process [99]. This sequence can be roughly compared to a periodic succession of A's and B's with 'pseudo-randomly' added A letters (see S_5 in Fig. 7.1(a)).

A convenient way to describe S_j is to use the two-valued function $\chi_{n,\phi}$, whose values ± 1 are identified to A $(+1)$ and B (-1):

$$\chi_{n,\phi} = \text{sign}\,[\cos(2\pi n/\tau + \phi) - \cos(\pi/\tau)] \tag{7.1}$$

with $n \in \mathbb{N}_0$ and a degree of freedom ϕ that is 2π periodic. In this chapter we will use this second construction method to define a more general parametrized structure. This angular degree of freedom ϕ is irrelevant for the infinite chain, but relevant for a finite segment $\overrightarrow{X}_{N,\phi} = [\chi_{1,\phi}\ \chi_{2,\phi}\ \cdots\ \chi_{N,\phi}]$ of $\overrightarrow{X}_{\infty,\phi}$. One can show that the finite segment $S_j = \sigma^j(B)$ is the same as $\overrightarrow{X}_{N,\phi}$, if $\phi = \pi/\tau$ and $N = F_j$. However, in general in this chapter $\phi \neq \pi/\tau$, and the two constructions are not equivalent. The irrationality of τ ensures that $\overrightarrow{X}_{N,\phi}$ is quasi-periodic [100].

Finally, there is also a geometrical construction of $\overrightarrow{X}_{N,\phi}$ possible via the cut-and-project method. This visualisation principle links to one of the computational methods for calculating the spectrum and eigenstates of a quasi-crystal, by solving Maxwell's equations in higher dimensions (i.e. super-space method) [63].

Our structure $P_{N,\phi}$, which we call a TIFS (Twinned Inverted Fibonacci Sequence), is composed of two symmetric abutted segments: the reversed $\overleftarrow{X}_{N,\phi} = [\chi_{N,\phi}\ \chi_{N-1,\phi}\ \cdots\ \chi_{1,\phi}]$ and $\overrightarrow{X}_{N,\phi}$, see Fig. 7.1(b), with the aim to disrupt the spectral properties of the Fibonacci sequence and thus to induce defect modes. For photonic implementation, A and B (or ± 1) correspond to two different material layers with the same length $L = 1$ μm and refractive indices $n_A = 3$ and $n_B = 2$, respectively. The outside refractive index is $n_0 = 2$.

We investigate the properties of the TIFS structure $P_{N,\phi}$ through numerical simulations (with CAMFR [39]) of the transmission $T = |t_L^2| = |t_R^2|$ with $t_{L/R}$ the left and right transmission amplitudes, and the left and right reflection $R_{L/R} = |r_{L/R}^2|$, with $r_{L/R}$ the left/right reflection amplitude (see Fig. 7.1(b) for conventions). For $\overleftarrow{X}_{N,\phi}$ and $\overrightarrow{X}_{N,\phi}$ we use the same conventions for transmission or reflection with an extra left/right arrow (e.g. $\overrightarrow{r}_L$ for the left reflection amplitude of $\overrightarrow{X}_{N,\phi}$, see Fig. 7.1(a)). The transmission is the same regardless of the input side because of reciprocity.

Fig. 7.2 shows the transmission of $P_{N,\phi}$ and the related 'non-mirrored' segment $\overrightarrow{X}_{2N,\phi}$ ($2N$ in order to have the same number of layers as $P_{N,\phi}$) as a function of $k_0 = 2\pi/\lambda_0$ with λ_0 the vacuum wavelength of an incident perpendicular plane wave. Similar to a periodic crystal, quasi-periodicity opens a series of bandgaps for both structures in the same ranges of k_0. In this chapter we plot the graphs

as a function of k_0 instead of $omega_0$ (so k_0 is not the Bloch wavenumber here). This is for easier correspondence with the first paper in this field.

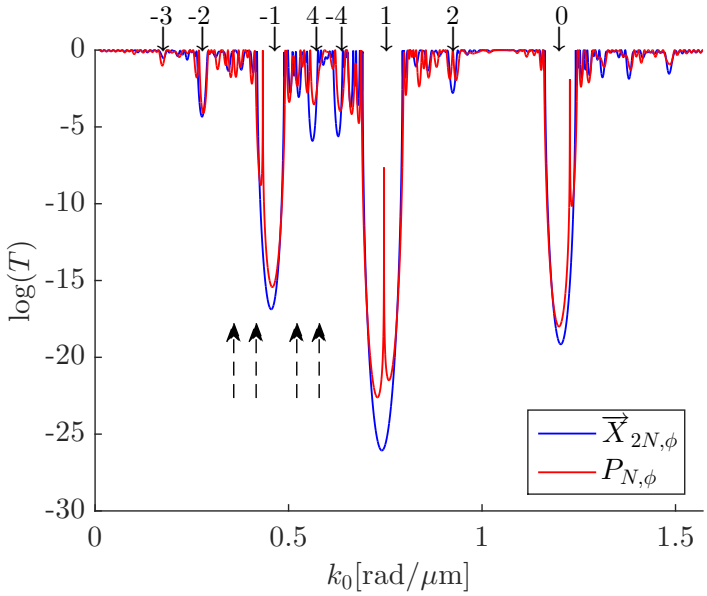

Figure 7.2: Transmission of $\overrightarrow{X}_{2N,\phi}$ (blue) and $P_{N,\phi}$ (red) with $N = 50$ and $\phi = 3$ rad. The black arrows on top denote the positions of the bandgaps given by Eq. 7.2 with the corresponding m values. The four dashed black arrows below indicate the k_0 values of the profiles in Fig. 7.3.

We can locate the theoretical positions of these bandgaps via the gap-labelling theorem [85, 99, 101, 102]

$$k_{gap} = [n + \mathrm{mod}(m/\tau, 1)]\,[2\pi/(D\ n_{\mathrm{av}})] \tag{7.2}$$

with $m \in \mathbb{Z}$, $n \in \mathbb{N}$, $D = 2L$ the basic pair thickness of our system and n_{av} the average refractive index. We mark the bandgaps using this equation with black arrows and the corresponding m number on top in Fig. 7.2.

If we compare these quasi-periodic spectra to the band diagram of a periodic succession of A and B (not shown), the gap around $k_0 \approx 1.2$ rad/μm ($m = 0$) appears in both periodic and quasi-periodic structures: It corresponds to the 'natural' first bandgap (with $n = 1$) of the periodic structure and to the smallest physical distance for a constructive round-trip. All the other gaps of the quasi-periodic structure thus open in a pass-band of the periodic structure (e.g. the first pass band $n = 0$ of the periodic structure is for $k_0 < 1.2$ rad/μm).

It is interesting to note that an infinite quasi-periodic sequence opens an infinite number of bandgaps, and the transmission spectrum becomes fractal [99,102]. Here for a finite sequence, we observe only the larger bandgaps with smaller $|m|$.

Each transmission peak inside and outside the bandgaps indicates a mode of the structure. Turning to the TIFS $P_{N,\phi}$ (red curve in Fig. 7.2) we observe some additional peaks of transmission inside the bandgaps in comparison to the transmission of $\overrightarrow{X}_{2N,\phi}$ (blue curve). As $P_{N,\phi}$ is not an exact Fibonacci sequence but is the result of stitching two sequences, this configuration creates an interface in

the structure at the mirror plane. This interface allows for one or more additional modes to appear in the bandgaps.

We show in Fig. 7.3 the profiles of four band modes of $P_{N,\phi}$ around the bandgap with $m = -1$. They display different shapes but are all symmetric with respect to the central mirror plane of $P_{N,\phi}$ (at $z = 50\mu$m). The two modes with $k_0 \approx 0.58$ and 0.42 rad/μm possess less 'modulations nodes' than the others and thus can be considered as more fundamental (more details in Sec. 7.3.1). All these profiles are also spatially extended over the whole structure.

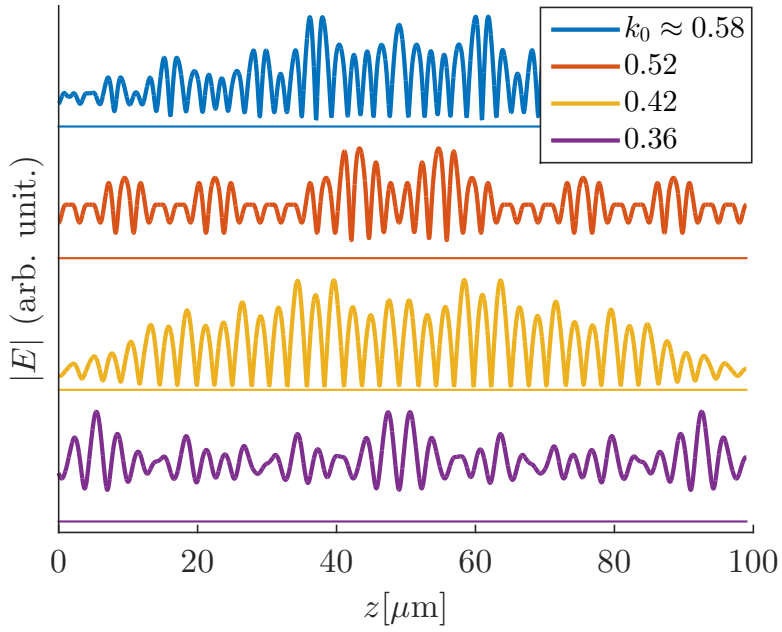

Figure 7.3: Field profiles of the band modes of the TIFS structure $P_{N,\phi}$ as a function of the position z with $N = 50$ and $\phi = 5$ rad. The modes at $k_0 \approx 0.52$ and 0.36 rad/μm are located in the middle of a band. The modes at $k_0 \approx 0.58$ and 0.42 rad/μm are located at the edge of a band. These k_0 are indicated by dashed black arrows in Fig. 7.2.

The latter is in contrast with the field profiles of the TIFS interface modes; we show these modes for the gap with $m = -1$ in Fig. 7.4 for different values of ϕ. An interface mode is confined to the central mirror plane for every value of ϕ, and this property is general for all bandgap modes. The interface mode profiles also present a symmetry (e.g. for $\phi = 0.5$ and 6 rad in Fig. 7.4) or an antisymmetry ($\phi = 1.5$ and 3 rad), more details will be provided below. Finally, larger bandgaps lead to more confined interface modes (not shown) with narrower bandwidths.

We focus on the transmission around two of the lower frequency bandgaps ($k_0 \approx 0.45$ rad/μm, $m = -1$, Fig. 7.5(a) and $k_0 \approx 1.2$ rad/μm, $m = 0$, Fig. 7.5(b)), varying ϕ and k_0. We do not examine the larger bandgap with $m = 1$, as it encounters the same topological properties as for $m = -1$. Moreover, in a larger bandgap the interface mode is narrower, so a finer grid of k_0 (higher computational cost) is needed. The interface mode in the bandgaps describes one (Fig. 7.5(b)) or two (Fig. 7.5(a)) cycles as a function of ϕ, respectively. Along these cycles the

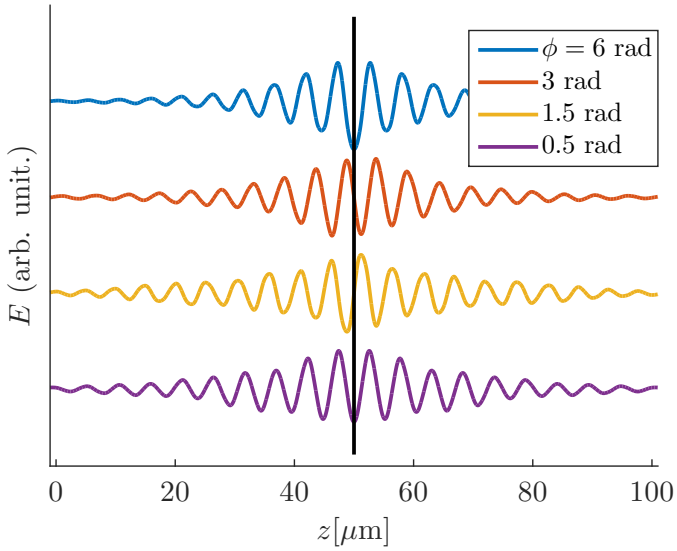

Figure 7.4: Electrical (E) field profiles of the interface mode as a function of the position z (see Fig. 7.1(b)) for varying ϕ. The structure is between $z = 0$ μm and $z = 100$ μm, the symmetry plane is indicated by the black line. The interface mode is located in the bandgap around $k_0 \approx 0.45$ rad/μm and $m = -1$ in Fig. 7.2.

interface mode performs some spectral jumps for definite values of ϕ. These jumps are the consequence of a letter switch in the sequence $\overrightarrow{X}_{N,\phi}$ (and symmetrically in $\overleftarrow{X}_{N,\phi}$), when ϕ varies (see Fig. 7.6).

More in detail, each letter of $\overrightarrow{X}_{N,\phi}$ flips from B to A (red crosses in Fig. 7.6) at a different value of ϕ (see Eq. 7.1). In addition, at this value of ϕ, the next letter in the sequence (except for the first one) also does a reverse flip from A to B (blue circles in Fig. 7.6). As $\overleftarrow{X}_{N,\phi}$ mirrors $\overrightarrow{X}_{N,\phi}$, these conclusions are also valid for the inverse sequence. As the interface mode is confined to the center of the TIFS structure $P_{N,\phi}$, the flipping of the first letters of $\overrightarrow{X}_{N,\phi}$ (or the last ones of $\overleftarrow{X}_{N,\phi}$) induce a larger jump than those at the extremities of the chain $P_{N,\phi}$ (with negligible field amplitude). We indicate with red triangles in Fig. 7.5 the ϕ values where one of the five first (last) letters of $\overrightarrow{X}_{N,\phi}$ ($\overleftarrow{X}_{N,\phi}$) flips, indeed leading to a significant spectral jump of the interface mode.

Furthermore, we indicate that the red crosses and blue circles are situated along lines (black dashed lines in Fig. 7.6). In addition, the ϕ separation (vertical distance in Fig. 7.6) between the same kind of flip (A to B or B to A) of two successive letters is always equal to 2.4 rad (so the vertical distance between two red crosses or between two blue circles in Fig. 7.6). The incommensurability between this 'flip' period and the ϕ period induces that these flips never occur two times at the exact same value of ϕ.

The number of cycles of the interface mode eigenvalues for a 2π path of ϕ is

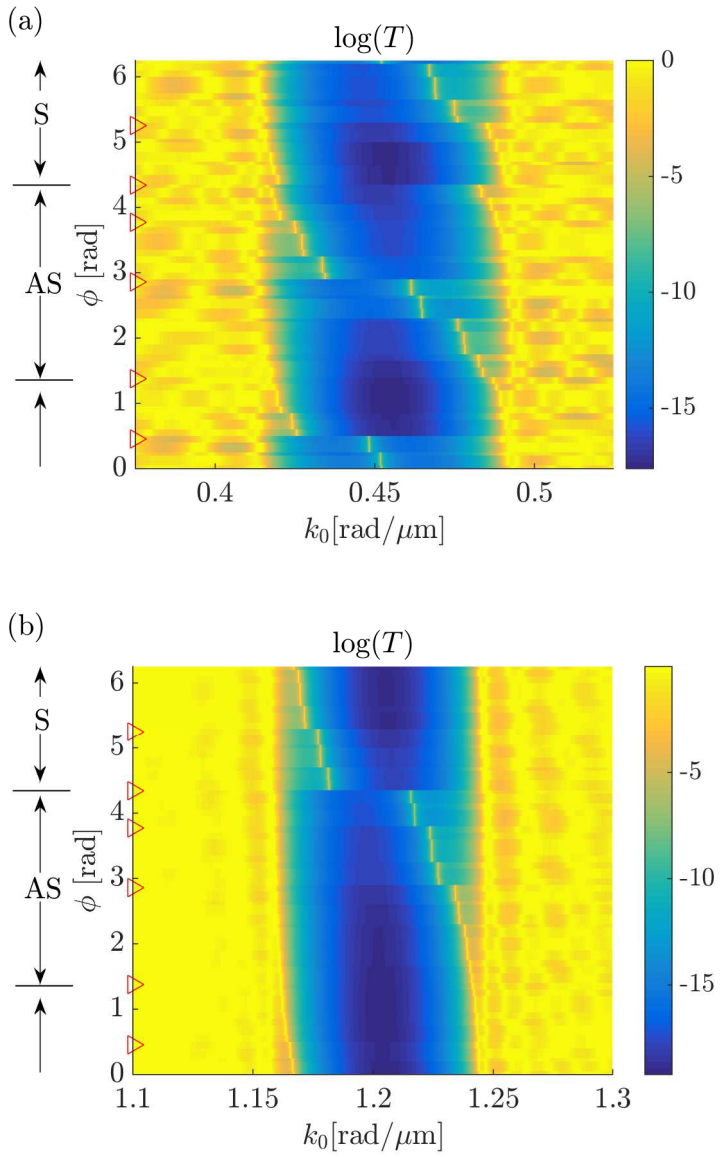

Figure 7.5: Transmission (log scale) of the TIFS structure $P_{N,\phi}$ as a function of k_0 and ϕ around the bandgap with $m = -1$ (a) and the bandgap with $m = 0$ (b) and with $N = 50$. The red triangles on the left axis indicate the values of ϕ where at least one of the first (last) letters of $\overrightarrow{X}_{N,\phi}$ ($\overleftarrow{X}_{N,\phi}$) flips (see Fig. 7.6), leading to a spectral (horizontal) jump of the interface mode. The 'AS' and 'S' zones stand for the ϕ regions where the interface mode profiles are antisymmetric or symmetric, respectively.

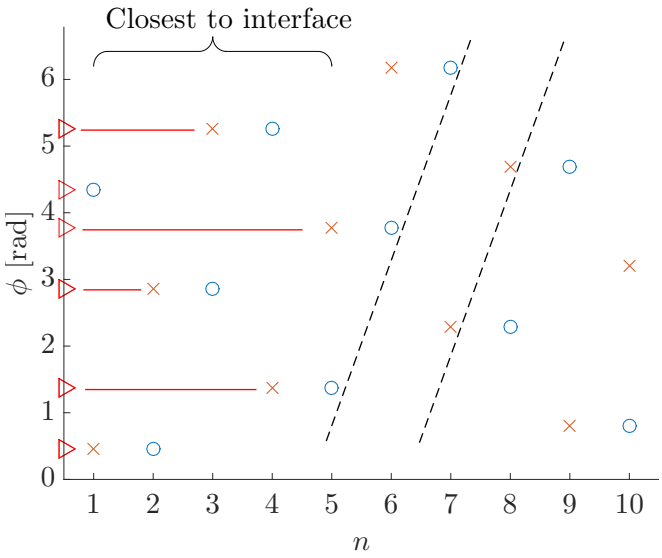

Figure 7.6: The ϕ values where a letter flips as a function of the letter position n in the sequence $\overrightarrow{X}_{N,\phi}$ (or symmetrically at the position $N-n+1$ in $\overleftarrow{X}_{N,\phi}$). The red crosses show the flips from B to A, and vice versa for the blue circles. The red triangles on the left axis indicate the values of ϕ where at least one of the first (last) letters of $\overrightarrow{X}_{N,\phi}$ ($\overleftarrow{X}_{N,\phi}$) flips.

determined by the winding number $w(k_0)$ of the bandgap:

$$w(k_0) = \frac{1}{2\pi}\int_0^{2\pi} \frac{\partial\theta_{\text{cav}}(k_0,\phi)}{\partial\phi} d\phi \tag{7.3}$$

with $\theta_{\text{cav}} = \overrightarrow{\theta}_L + \overleftarrow{\theta}_R$ the sum of the phases of the reflection coefficients at the inner boundaries of $\overrightarrow{X}_{N,\phi}$ and $\overleftarrow{X}_{N,\phi}$ (see Fig. 7.1(b)). The winding number has to be evaluated at a particular k_0, but one obtains the same value for any k_0 in the bandgap. Note that without gain and loss $\overrightarrow{\theta}_L = \overleftarrow{\theta}_R$. The winding number represents the number of times a closed curve (defined by $\theta_{\text{cav}}(k_0,\phi)$ here) travels around a point. This number is also connected with the gap Chern number [103], the characteristic number that links band structure and topology [104].

If we check the interface mode field profile (Fig. 7.4), we observe that it keeps an antisymmetric pattern along a cycle in the bandgap ('AS' region between $\phi \approx 1.4$ and 4.3 rad in Fig. 7.5(a)). For the second cycle ('S' region between $\phi \approx 4.3$ and $1.4 + 2\pi$ rad in Fig. 7.5(a)) the pattern is symmetric. The profile symmetry of the edge mode flips from symmetric to antisymmetric (or vice versa) when the mode begins another cycle/spectral crossing through the bandgap. If the number of cycles is odd but at least three, the profile symmetry still flips between consecutive cycles. However, the single cycle mode that crosses $\phi \approx 4.3$ (as in Fig. 7.5(b)) flips the symmetry 'in the middle'. For example in Fig. 7.5(b), the edge mode is antisymmetric in the 'AS' region below $\phi \approx 4.3$ rad and symmetric in the 'S' region beyond this ϕ value while it is still in the same cycle. This value of ϕ corresponds to a change of the very first letter of $\overrightarrow{X}_{N,\phi}$ from A to B (Fig. 7.6), i.e. a strong change at the core of the resonant interface 'cavity' leading to the

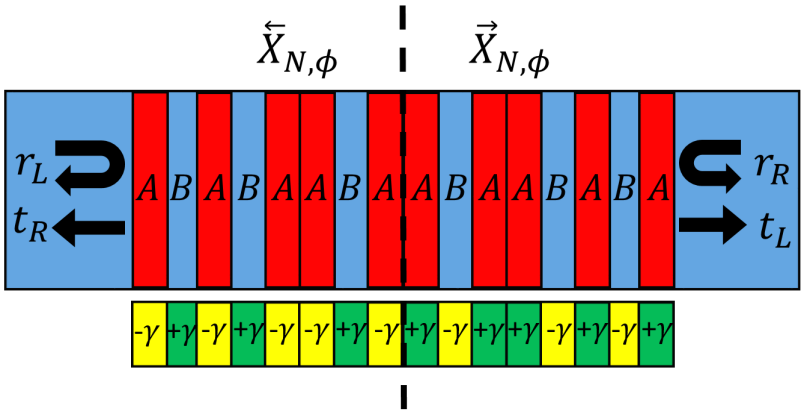

Figure 7.7: Sketch of the TIFS structure $P_{N,\phi}$ with the gain and loss factor γ. All A's on left have gain $(-\gamma)$, all B's on the left have loss $(+\gamma)$, and vice versa for the right side.

possibility of a symmetry switch.

7.3 TIFS with $\mathcal{PT}$ symmetry

Now we introduce gain and loss in a balanced fashion on both sides of the mirror plane. Therefore, in $\overleftarrow{X}_{N,\phi}$ all letters A experience gain $(n_A = 3 - j\gamma)$ and all letters B experience loss $(n_B = 2 + j\gamma)$, with γ the gain/loss factor. For $\overrightarrow{X}_{N,\phi}$ we introduce the complex conjugates ($n_A = 3 + j\gamma$, $n_B = 2 - j\gamma$, see Fig. 7.7). In this way the whole TIFS structure $P_{N,\phi}$ is $\mathcal{PT}$-symmetric, but each part individually is not. As there are more A's than B's, $\overleftarrow{X}_{N,\phi}$ presents more gain than loss (depending on the sign of γ), and vice versa for $\overrightarrow{X}_{N,\phi}$.

Note that the relatively large γ values ($|\gamma| \in [0, 0.5]$) that we explore are connected to the large index contrast $n_B - n_A$ and the limited $N = 50$ of our simulations. More realistic $|\gamma| < 0.005$ could result from a combination of weaker index contrast $|n_B - n_A| \sim 0.1$ and larger $N > 50$.

7.3.1 Global properties

An interesting global transmission pattern arises as the gain/loss value increases. We show T of $P_{N,\phi}$ as a function of k_0 and ϕ for various γ in Fig. 7.8. As we increase γ from Fig. 7.8(a) to (d), saturated transmission peaks (in yellow) appear. However, for even larger γ they subsequently tend to disappear. This pattern indicates the typical merging of two modes at an exceptional point under the action of $\mathcal{PT}$ symmetry (see Chap. 2). Beyond the exceptional points, the transmission peaks disappear as the modes become complex (leading to dark blue zones).

Furthermore, we observe a characteristic feature of $\mathcal{PT}$ symmetry: in general more fundamental modes merge at smaller γ than higher-order modes, because they are easier to 'break' (see also [74]). Indeed, modes at the band edges (the more fundamental ones) are the first to merge (higher transmission zones at band

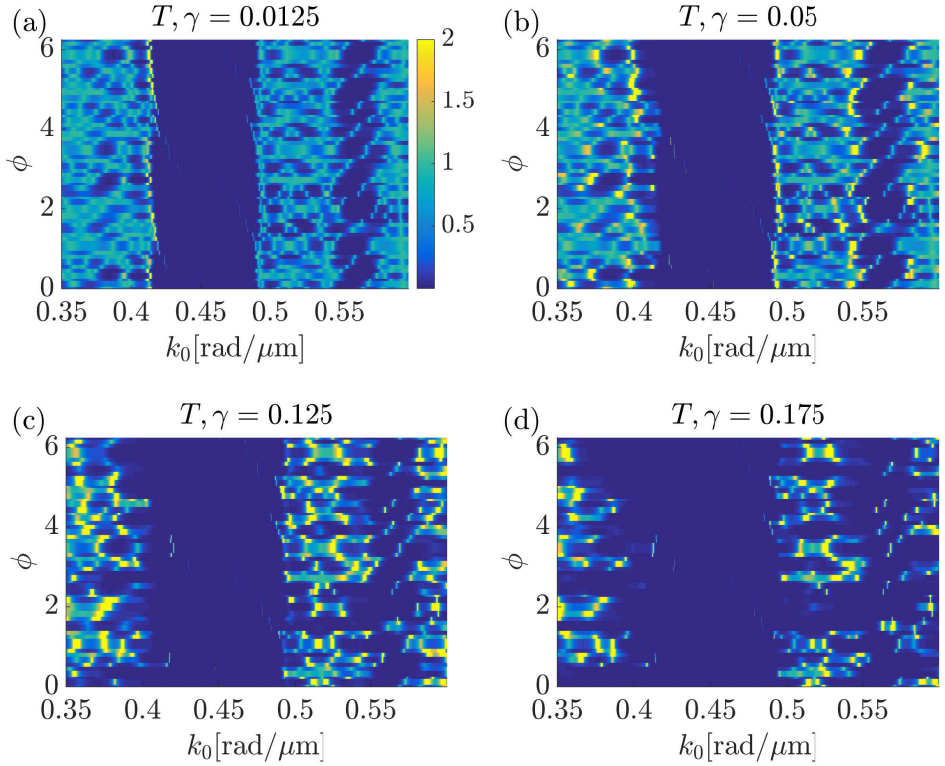

Figure 7.8: Transmission T (saturated to two for clarity) of $P_{N,\phi}$ as a function of k_0 and ϕ with $N = 50$ and varying γ.

edges in Fig. 7.8(a,b)). Afterwards, the pass-band centers (the less fundamental modes) begin to merge at greater γ (Fig. 7.8(c,d)). To illustrate, we show the fields of two band edge modes ($k_0 \approx 0.58$ and 0.42 rad/μm in Fig. 7.3) and two band center modes ($k_0 \approx 0.52$ and 0.36 rad/μm). The band center modes present more 'modulation nodes' than the edge modes, demonstrating a less fundamental pattern.

Finally, at ever higher γ the transmission picture will have fewer features and becomes largely blue: almost all modes are broken, leading to negligible transmission.

Besides this general pattern, the behaviour of the gap defect modes is more erratic: some modes merge at small γ, while others remain in the bandgap at high γ, we discuss these modes in detail in the next section.

7.3.2 Local properties

After this general $\mathcal{PT}$ behaviour of the TIFS structure for varying ϕ, we focus on a few specific geometries (specific ϕ) to distinguish more precise features. We show T, R_L and R_R as a function of k_0 and γ in Fig. 7.9 for specific ϕ values. In these figures, left and right incidence corresponds to $\gamma > 0$ and < 0, respectively (the upper and lower halves of the graphs). Two bandgaps are displayed, indicated by the two horizontal black arrows in Fig. 7.9(a). For certain values of ϕ, an interface mode appears in these bandgaps (denoted by the red arrows in Fig. 7.9(a) around

$k_0 \approx 0.425$ rad/μm and $k_0 \approx 0.56$ rad/μm at $\gamma = 0$).

Most of the time $R_L > R_R$ (more yellow in upper half) due to the presence of more gain on the left side ($\overleftarrow{X}_{N,\phi}$) than on the right side (a consequence of the construction). We also note that, as usual in $\mathcal{PT}$ symmetry, two modes tend to merge with one another at so-called exceptional points: their eigenvalues become complex conjugates and they no longer lead to a transmission peak, and only provide reflection afterwards. Band modes merge with one another in each ϕ configuration (e.g. at the green arrow around $k_0 \approx 0.4$ rad/μm in Fig. 7.9(f)). However, bandgap interface modes tend to merge with modes in the closest band (e.g. at the green arrow around $k_0 \approx 0.4$ rad/μm in Fig. 7.9(d)). Or they merge with spectrally distant modes at large values of γ (e.g. the interfaces modes that begin their trips at the red arrows around $k_0 \approx 0.49$ rad/μm and $k_0 \approx 0.57$ rad/μm at $\gamma = 0$ in Fig. 7.9(e)). Note that we can expect that the system becomes unstable (as in Chap. 6) due to the large gain before the latter two modes merge.

During the merging process, the field profiles of the modes slowly become similar, see an example of an edge mode and a band mode combination in Fig. 7.10. The band mode (red curve, middle), which is initially distributed along the structure, becomes more and more confined at the center (blue curve, bottom), similar to an edge mode profile. The edge mode evolves in the opposite way (red and blue upper curves). In general, a band and edge mode merge at larger γ than two band modes, because their profiles are quite different, and one needs more gain and loss to distort them. Conversely, two merging band modes are in general close (spectrally and with similar profiles), making them easier to match and merge at smaller γ.

Similar to other 1D $\mathcal{PT}$ structures and the structure of Chap. 6, we can observe Anisotropic Transmission Resonances (ATRs) [61] or one-sided invisibility, where $T = 1$ (red lines in Fig. 7.9(d)), and one of the reflections is equal to zero (red lines in Fig. 7.9(c)). These ATRs originate from the peaks of $T = 1$ in the passive system where $R_L = R_R = 0$. Upon introduction of gain/loss, the system distinguishes the left and right reflections, so only one is equal to zero and we detect the typical ATRs. In tight binding approaches e.g. with a limited number of cavities one can obtain analytical expressions for the ATRs as in Chap. 6. Here, however, the analytics become unwieldy with many interfaces, and we resort to numerical transfer matrix approaches, leading to fairly complex patterns of ATRs as a function of ϕ (Fig. 7.9).

In addition, we observe more exotic merging behaviours of the band modes (Fig. 7.11(a,b)) or interface modes (Fig. 7.11(c,d)). Some islands of transmission appear in the bandgap (around $\gamma \approx 0.32$ in Fig. 7.11(e,f)). Furthermore, we find the 'symmetry recovery' phenomenon described in Chap. 5 (denoted by the green arrow around $k_0 = 2.77$ rad/μm in Fig. 7.11(d)): With tailored coupling between four modes, one can achieve that two modes merge initially as γ increases. However, when γ continues to increase, they become real again (inverse exceptional point, around $\gamma = 0.12$), and finally merge with their original '$\mathcal{PT}$-partners' at greater γ. The fact that this appears is not strange, because there are many modes with many coupling constants, but still one needs a relatively delicate coupling balance, so it is uncommon to observe.

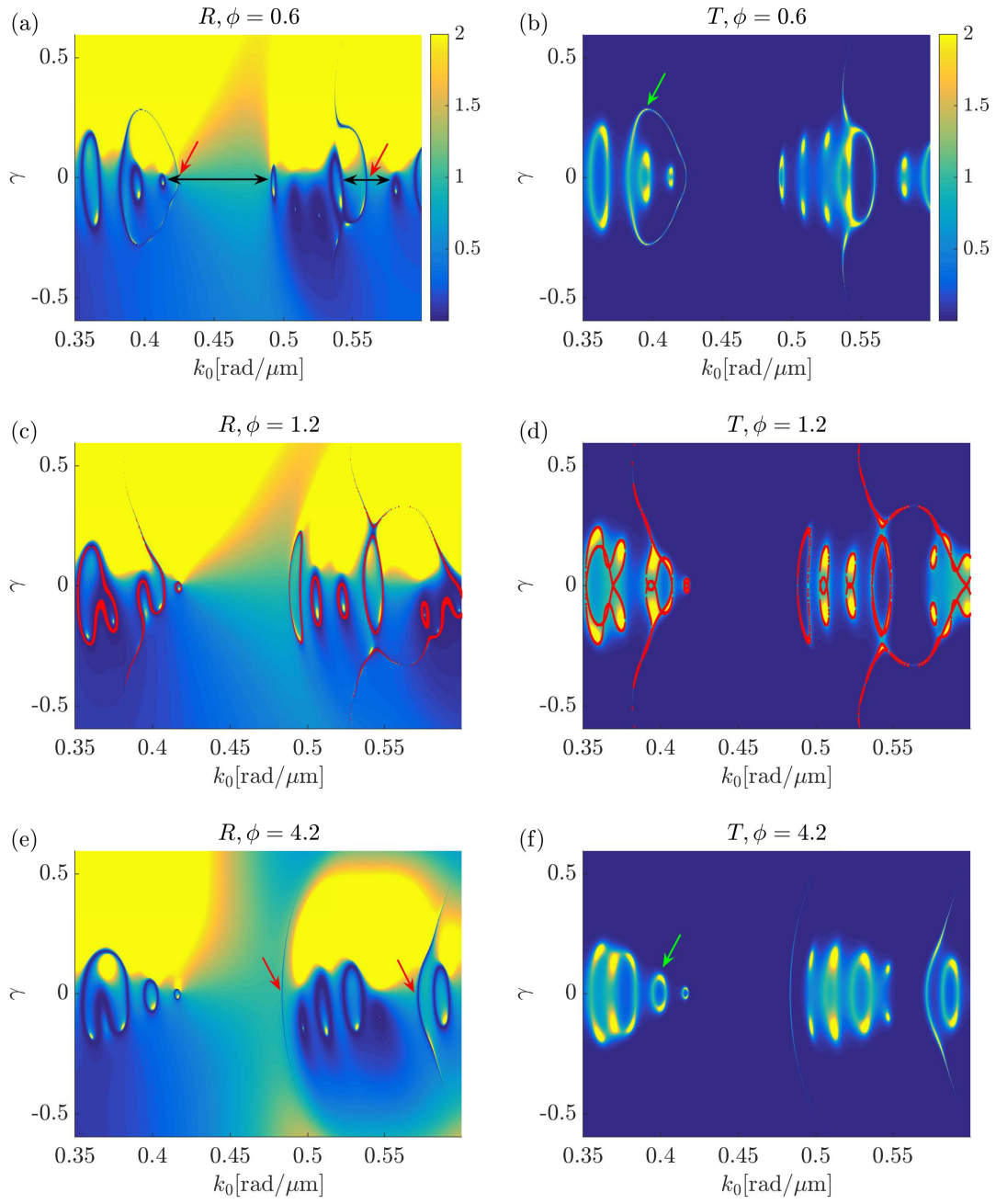

Figure 7.9: Reflection (left column) and transmission (right column) for $P_{N,\phi}$ ($N = 50$) as a function of γ and k_0, and saturated to two. (a,b) For $\phi = 0.6$, (c,d) 1.2 and (e,f) 4.2. $\gamma > 0$ (< 0) is for left (right) incidence. The two black double arrows in (a) indicate the bandgaps. The two red arrows in (a,e) show the interfaces modes in these bandgaps. The green arrow in (b) shows the merging of a band mode and an interface mode, in (f) it indicates two band modes merging. The red lines represent ATRs.

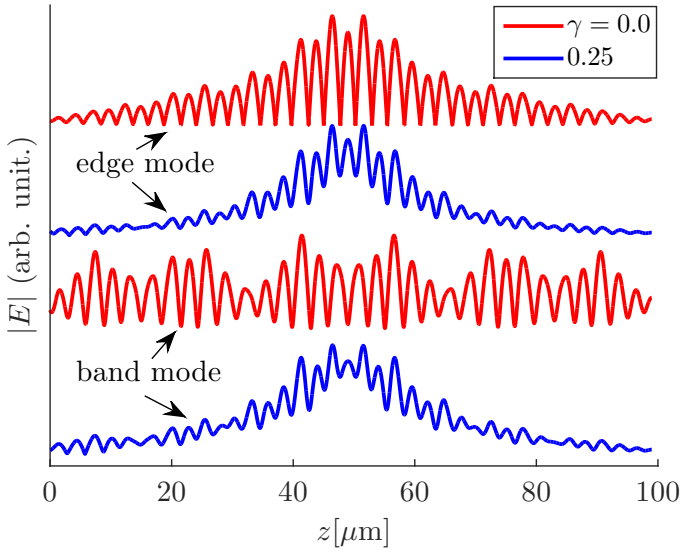

Figure 7.10: Field profiles of an edge mode (two upper curves) and a band mode (two lower curves) that merge together. Red curves: without gain and loss ($\gamma = 0$, around $k_0 \approx 0.42$ and 0.38 rad/μm respectively in Fig. 7.9(a,b)). Blue curves: just before their merging ($\gamma = 0.25$, around $k_0 \approx 0.405$ and 0.39 rad/μm respectively in Fig. 7.9(a,b)).

7.3.3 Laser resonances

Focusing on the merging behaviour of an interface mode, we observe oscillations of the transmission, with peaks of very high intensity indicating lasing effects (yellow arrows in Fig. 7.12(a,b)). These peaks are elegantly described with a Fabry-Perot model (based on Sec. 3.2.1) of a cavity centered at the mirror plane. The phase matching condition of a roundtrip in the cavity (Eq. 7.4) describes the presence and evolution of the modes. A quality factor of the cavity (Eq. 7.5), as dictated by its inner reflections, gives us information on the strengths of the resonances (at $\gamma \neq 0$) and so the intensity:

$$\theta_{\text{cav}} = 2m\pi, m \in \mathbb{Z} \tag{7.4}$$

$$Q = \frac{1}{1 - |\overleftarrow{r}_R||\overrightarrow{r}_L|} \tag{7.5}$$

Eq. 7.4 is indicated by the red dots in Fig. 7.12(c,d). The quality factor Q depends on the amplitudes of the inner reflection coefficients of each part of $P_{N,\phi}$. We show $\log(Q)$ in Fig. 7.12(c,d). By comparing Fig. 7.12(a,b) and Fig. 7.12(c,d) we conclude that the modes are well described by this simple model: the alignment of phase matching (red dots) and high-Q (yellow zones) in (c,d) indeed corresponds with the lasing resonances in (a,b).

By varying the crystal phase ϕ or by choosing different bandgaps, we can observe various merging schemes of the interface mode. In Fig. 7.12(a), the variation of k_0 as a function of γ of the interface mode branch is relatively small, leading to a succession of laser resonances closely spaced in frequency. In contrast, in Fig.

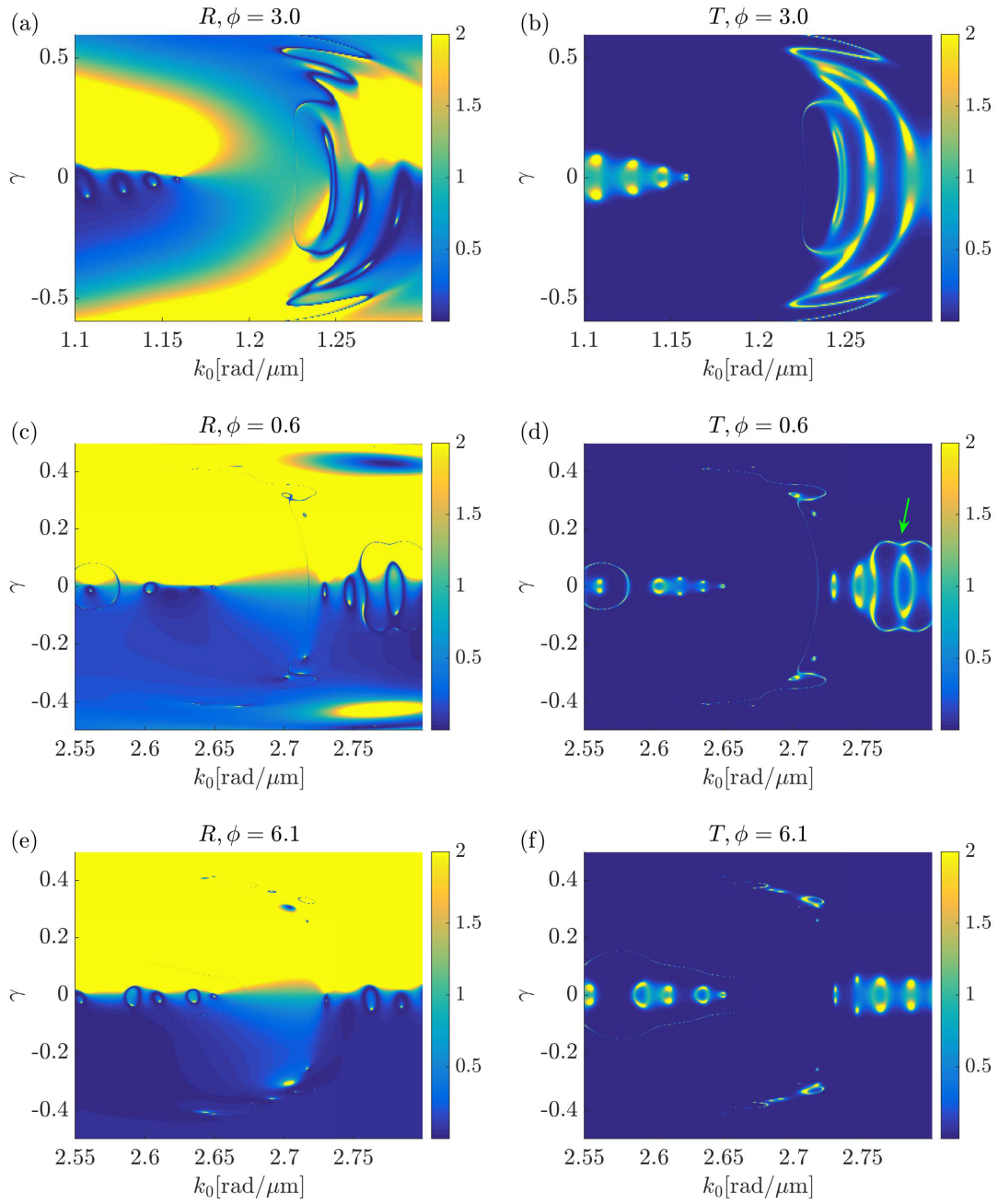

Figure 7.11: Reflection (left column) and transmission (right column) for $P_{N,\phi}$ ($N = 50$) as a function of γ and k_0, saturated to two. (a,b) For $\phi = 3.0$, (c,d) 0.6 and (e,f) 6.1 rad. $\gamma > 0$ (< 0) is for left (right) incidence. The green arrow (d) denotes a symmetry recovery phenomenon.

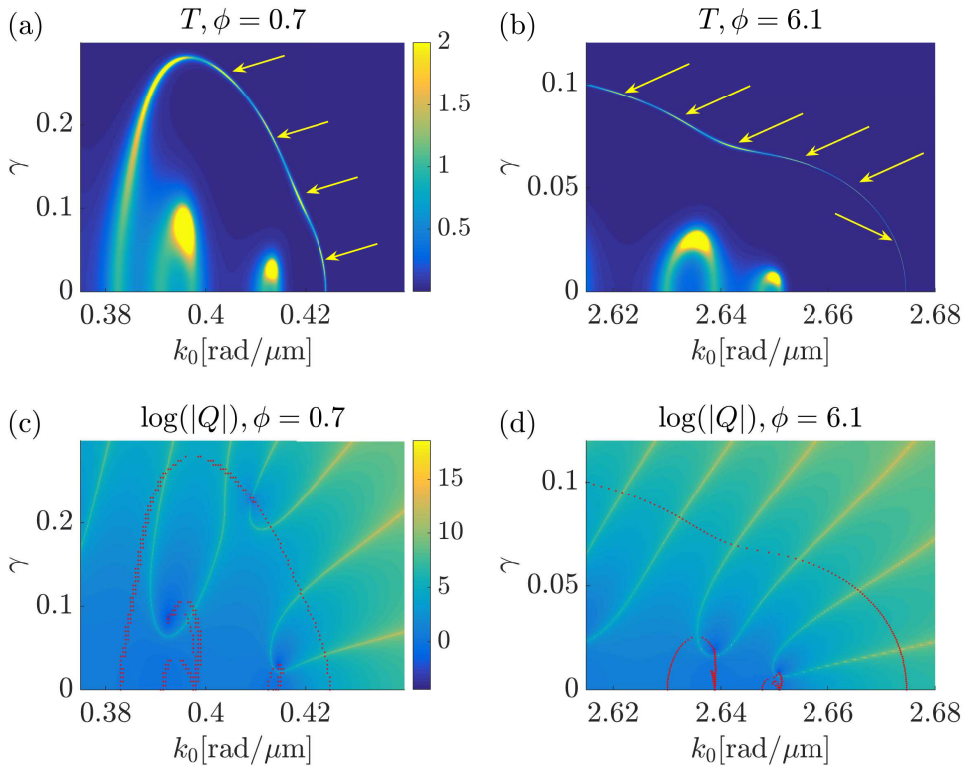

Figure 7.12: (a,b) Transmission (saturated to two) of $P_{N,\phi}$ ($N = 50$) as a function of γ and k_0 via rigorous transfer matrix calculation. (c,d) Fabry-Perot model with the logarithm of Q (Eq. 7.5) for the same structures. The red points represent constructive cavity interference, given by Eq. 7.4.

7.12(b), the variation of k_0 as a function of γ along the branch is relatively large, leading to more spectrally distant resonances. The large number of possible merging scenarios allows us to spectrally spread or tighten the laser resonances, and thus opens the way to laser resonance engineering. Furthermore, we can expect to take advantage of the field profile difference between band and interface modes, in order to select which resonances will occur at smaller γ. Indeed, if we put gain and loss only in the layers close to the interface, we will reach the exceptional points of the interface modes at smaller γ than for the band modes. Thus the interface mode should lase at smaller γ and will not be perturbed by the band modes.

7.4 Summary

We study a 1D photonic quasi-crystal with topological features in a $\mathcal{PT}$ symmetry context. We use the scattering characteristics to investigate various properties of this structure, especially the presence of interface modes in the bandgaps. The structural degree of freedom ϕ (i.e. the crystal phase control variable) allows these modes to spectrally cross the bandgap. These cycles are connected with the winding number of the bandgap and the gap Chern number. Spectral jumps occur along these cycles for specific values of ϕ, corresponding to the flipping of a letter in the

crystal sequence. In addition, the symmetry of the gap modes are determined by these cycles and spectral jumps.

By adding gain and loss in a $\mathcal{PT}$-symmetric fashion, we observe a set of complex behaviours that is not in simple correspondence with the passive case. Mostly, mode pairs merge at exceptional points under the action of $\mathcal{PT}$ symmetry. This merging feature gives rise to high transmission peaks and even laser resonances. When γ is beyond these exceptional points, the modes become complex and the transmission fades out. In a general pattern, we observe that the side modes of a band merge together at lower γ than the less fundamental ones at the band center. We also observe a symmetry recovery phenomenon, a complex merging scheme involving four band modes and described extensively in Chap. 5. The interface modes created in the bandgaps merge with nearby band modes, and present very high transmission at laser-like resonances. The spectral dispersion of these laser resonances can be controlled by the various involved parameters. In addition, we observe anisotropic transmission resonances (presented in Chap. 6) where the transmission is unity and one of the reflections is equal to zero. The mix of order and disorder of the present system thus gives a useful basis for exploring how a variety of $\mathcal{PT}$ symmetry related effects are interrelated.

In future work, one can study the stability of this system with time-domain simulations to figure out what can be feasible in experimental setups. One can also try to add non-linearity to potentially obtain non-reciprocal transmission for the ATRs. However, this will be a complex system with many parameters to examine.

8

Conclusion and outlook

Throughout this work we studied and exploited the potential of mode control offered by $\mathcal{PT}$ symmetry in various fundamental structures and configurations. Tunability and a positive role for losses are crucial elements for the design of more efficient and novel photonic components, strengthening $\mathcal{PT}$ symmetry as a promising paradigm. In the following, we propose a concise summary of this work and discuss further opportunities.

First, we considered the switching capability of a finite $\mathcal{PT}$-symmetric diffraction grating under illumination. In the Littrow case, the structure supports two Bloch modes that interfere at the end of the grating and excite the two transmission diffraction orders. By adding gain and loss, these two modes merge at an exceptional point. Before this point, we can control the interferometric operation with gain and loss to excite the desired transmission diffraction order. Beyond this point, as the modes become complex, the incident light cannot couple to them and is entirely reflected. In between, laser-like resonances can be achieved for the mode that experiences gain. In the perpendicular incidence case, only one Bloch mode is available and it does not allow for a passive dual-mode interference scenario. Nevertheless a new mode pops up to merge with the first one when gain and loss is increased. Interference between the various transmission diffraction orders is restored until the exceptional point. Subsequently, we vary the period of the imaginary part independently of the real part. This configuration mixes previously uncoupled modes and gives a different symmetry breaking picture showing elements of the two previous cases. It demonstrates that the various possible patterns of gain and loss gives us a greater control to tailor the modes.

Afterwards, we investigated more in detail the exceptional points and the two $\mathcal{PT}$ phases. In the simplest four-mode linear structure, by analysing the mode merging properties, we discover the symmetry recovery effect. This phenomenon

exhibits two distinct unbroken $\mathcal{PT}$ phases separated by a broken one that is delimited by an exceptional point and an 'anti'-exceptional point. The fine tuning of the coupling constants allows for two previously uncoupled modes to merge (symmetry breaking) before splitting (symmetry recovery) and merge with their initial partners (final broken phase). This effect also happens in more complicated structures with multiple modes.

Subsequently we focus on unidirectional invisibility or anisotropic transmission resonances (ATRs), where transmission is unity and reflection is zero from one side only. With two cavities coupled to a waveguide, we demonstrate that the ATR bandwidth can be easily tuned from narrow to broadband by varying the length between the cavities. Moreover, we address other effects such as lasing states, exceptional points and stability. This structure offers more degrees of freedom than previously reported structures with ATRs and is suspected to be more easily implemented experimentally. Moreover, a four-cavity structure displays ATR schemes with a new level of complexity with numerous degrees of freedom, which offers possibilities for 'ATR engineering'.

Finally we mix $\mathcal{PT}$ symmetry and topology in a 1D quasi-periodic structure. In the passive case, the structure exhibits topological interface modes in the bandgaps. Topology gives us information about the positions of these bandgaps via the gap labelling theorem. The behaviours of the interface modes under the variation of a structural degree of freedom is defined by the winding number, which is also linked to the gap Chern number of the bandgap. By adding gain and loss in a $\mathcal{PT}$-symmetric fashion, we introduce a tool to manipulate these interface modes. The huge number of modes, bandgaps and degrees of freedom makes this structure rich of opportunities. The ATRs display a more complex pattern than ever. Symmetry recovery is observed between band modes. The interface modes merge with band modes and exhibit laser resonances along their merging branches. These branches can be controlled so the frequency dispersion of the laser resonances becomes tunable. The mix of order and disorder of the present system thus gives a useful basis for exploring how a variety of $\mathcal{PT}$ symmetry related effects are interrelated.

Further work can examine more realistic gain and loss models. Gain is a complicated feature that can evidence saturation or non-uniformity due to charge carrier dynamics. Loss is far easier to produce as an inherent component of materials, but its intensity is usually fixed by the geometry and materials and is hard to tune. A perfect balance between gain and loss is complex, thus we need to address $\mathcal{PT}$ effects with an imperfect distribution of gain and loss.

In Chap. 6 the ATRs can be broadband, but the effect is stronger close the cavity frequency. Multi-mode cavities could be investigated to extend the reach of this effect, leading e.g. into the field of ring resonator cavities.

The stability analysis with time domain simulations performed in Chap. 6 should be done for the topological structure of Chap. 7. The stability limit of a $\mathcal{PT}$ system is often defined by the exceptional points. By playing with the gain/loss pattern we can choose the modes that are the most likely to merge first. In this way we can tailor the effects to observe in the stable region.

Bragg gratings with non-linearity have demonstrated robust ATRs with non-reciprocal transmission. We can also consider non-linearity in our 1D structures to potentially obtain real non-reciprocal transmission for the ATRs. However, with

the increasing number of degrees of freedom, these systems become challenging to investigate.

To conclude, $\mathcal{PT}$ symmetry may not be the complete solution to design cheap, fast and compact photonic devices, because of the complexity to obtain perfect gain and loss. However it can change our mindset about inherent loss, which can be a useful property and not an unwanted feature. Throughout this thesis, we demonstrate the surprising tuning opportunities of $\mathcal{PT}$ symmetry in multi-modal designs. This mode control by the previously neglected complex part of the refractive index is fundamentally exciting for the development of future photonic devices.

Bibliography

[1] L. Razzari and R. Morandotti, "Optics: Gain and loss mixed in the same cauldron," *Nature*, vol. 488, no. 7410, pp. 163–164, 2012.

[2] H. Ramezani, T. Kottos, R. El-Ganainy, and D. N. Christodoulides, "Unidirectional nonlinear PT-symmetric optical structures," *Phys. Rev. A*, vol. 82, p. 043803, 2010.

[3] C. M. Bender and S. Boettcher, "Real spectra in non-hermitian hamiltonians having PT symmetry," *Phys. Rev. Lett.*, vol. 80, no. 24, pp. 5243–5246, 1998.

[4] R. El-Ganainy, K. G. Makris, D. N. Christodoulides, and Z. H. Musslimani, "Theory of coupled optical PT-symmetric structures," *Opt. Lett.*, vol. 32, no. 17, pp. 2632–2634, 2007.

[5] T. Kottos, "Optical physics: Broken symmetry makes light work," *Nat. Phys.*, vol. 6, no. 3, pp. 166–167, 2010.

[6] A. Lupu, H. Benisty, and A. Degiron, "Switching using PT symmetry in plasmonic systems: positive role of the losses," *Opt. Express*, vol. 21, no. 18, pp. 21651–21668, 2013.

[7] A. Guo, G. J. Salamo, D. Duchesne, R. Morandotti, M. Volatier-Ravat, V. Aimez, G. A. Siviloglou, and D. N. Christodoulides, "Observation of PT-Symmetry breaking in complex optical potentials," *Phys. Rev. Lett.*, vol. 103, p. 093902, 2009.

[8] N. X. A. Rivolta and B. Maes, "Symmetry recovery for coupled photonic modes with transversal pt symmetry," *Opt. Lett.*, vol. 40, no. 16, pp. 3922–3925, 2015.

[9] C. E. Ruter, K. G. Makris, R. El-Ganainy, D. N. Christodoulides, M. Segev, and D. Kip, "Observation of parity-time symmetry in optics," *Nat. Phys.*, vol. 6, no. 3, pp. 192–195, 2010.

[10] S. Klaiman, U. Günther, and N. Moiseyev, "Visualization of branch points in PT-symmetric waveguides," *Phys. Rev. Lett.*, vol. 101, p. 080402, 2008.

[11] J. Čtyroký, V. Kuzmiak, and S. Eyderman, "Waveguide structures with antisymmetric gain/loss profile," *Opt. Express*, vol. 18, no. 21, pp. 21585–21593, 2010.

[12] S. V. Suchkov, S. V. Dmitriev, B. A. Malomed, and Y. S. Kivshar, "Wave scattering on a domain wall in a chain of PT-symmetric couplers," *Phys. Rev. A*, vol. 85, p. 033825, 2012.

[13] C. Huang, F. Ye, and X. Chen, "Mode pairs in PT-symmetric multimode waveguides," *Phys. Rev. A*, vol. 90, no. 4, p. 043833, 2014.

[14] N. X. A. Rivolta and B. Maes, "Diffractive switching by interference in a tailored PT-symmetric grating," *J. Opt. Soc. Am. B*, vol. 32, no. 7, pp. 1330–1337, 2015.

[15] S. Phang, A. Vukovic, H. Susanto, T. M. Benson, and P. Sewell, "Ultrafast optical switching using parity time symmetric bragg gratings," *J. Opt. Soc. Am. B*, vol. 30, no. 11, pp. 2984–2991, 2013.

[16] H. Benisty, A. Degiron, A. Lupu, A. D. Lustrac, S. Chénais, S. Forget, M. Besbes, G. Barbillon, A. Bruyant, S. Blaize, and G. Lérondel, "Implementation of PT symmetric devices using plasmonics: principle and applications," *Opt. Express*, vol. 19, no. 19, pp. 18004–18019, 2011.

[17] M. Kulishov, J. Laniel, N. Bélanger, J. Azaña, and D. Plant, "Nonreciprocal waveguide bragg gratings," *Opt. Express*, vol. 13, no. 8, pp. 3068–3078, 2005.

[18] M. Kulishov and B. Kress, "Distributed bragg reflector structures based on PT-symmetric coupling with lowest possible lasing threshold," *Opt. Express*, vol. 21, no. 19, pp. 22327–22337, 2013.

[19] M. Kulishov and B. Kress, "Free space diffraction on active gratings with balanced phase and gain/loss modulations," *Opt. Express*, vol. 20, no. 28, pp. 29319–29328, 2012.

[20] L. Feng, Z. J. Wong, R.-M. Ma, Y. Wang, and X. Zhang, "Single-mode laser by parity-time symmetry breaking," *Science*, vol. 346, no. 6212, pp. 972–975, 2014.

[21] B. Peng, S. K. Özdemir, F. Lei, F. Monifi, M. Gianfreda, G. L. Long, S. Fan, F. Nori, C. M. Bender, and L. Yang, "Parity-time-symmetric whispering-gallery microcavities," *Nat. Phys.*, vol. 10, no. 5, pp. 394–398, 2014.

[22] B. Peng, S. K. Özdemir, S. Rotter, H. Yilmaz, M. Liertzer, F. Monifi, C. M. Bender, F. Nori, and L. Yang, "Loss-induced suppression and revival of lasing," *Science*, vol. 346, no. 6207, pp. 328–332, 2014.

[23] M. Brandstetter, M. Liertzer, C. Deutsch, P. Klang, J. Schöberl, H. E. Türeci, G. Strasser, K. Unterrainer, and S. Rotter, "Reversing the pump dependence of a laser at an exceptional point," *Nat. Commun.*, vol. 5, p. 4034, 2014.

[24] H. Ramezani, D. N. Christodoulides, V. Kovanis, I. Vitebskiy, and T. Kottos, "PT-symmetric talbot effects," *Phys. Rev. Lett.*, vol. 109, no. 3, p. 033902, 2012.

[25] A. Regensburger, C. Bersch, M.-A. Miri, G. Onishchukov, D. N. Christodoulides, and U. Peschel, "Parity-time synthetic photonic lattices," *Nature*, vol. 488, no. 7410, pp. 167–171, 2012.

[26] K. G. Makris, R. El-Ganainy, D. N. Christodoulides, and Z. H. Musslimani, "PT -symmetric optical lattices," *Phys. Rev. A*, vol. 81, p. 063807, 2010.

[27] M. C. Zheng, D. N. Christodoulides, R. Fleischmann, and T. Kottos, "PT optical lattices and universality in beam dynamics," *Phys. Rev. A*, vol. 82, no. 1, p. 010103, 2010.

[28] K. G. Makris, R. El-Ganainy, D. N. Christodoulides, and Z. H. Musslimani, "Beam dynamics in PT symmetric optical lattices," *Phys. Rev. Lett.*, vol. 100, p. 103904, 2008.

[29] R. Uzdin and N. Moiseyev, "Scattering from a waveguide by cycling a non-hermitian degeneracy," *Phys. Rev. A*, vol. 85, p. 031804, 2012.

[30] S. Phang, A. Vukovic, S. C. Creagh, P. D. Sewell, G. Gradoni, and T. M. Benson, "Localized single frequency lasing states in a finite parity-time symmetric resonator chain," *Scientific Reports*, vol. 6, p. 20499, 2016.

[31] Y. D. Chong, L. Ge, and A. D. Stone, "PT-symmetry breaking and laser-absorber modes in optical scattering systems," *Phys. Rev. Lett.*, vol. 106, p. 093902, 2011.

[32] S. Savoia, G. Castaldi, V. Galdi, A. Alù, and N. Engheta, "Tunneling of obliquely incident waves through PT-symmetric epsilon-near-zero bilayers," *Phys. Rev. B*, vol. 89, no. 8, p. 085105, 2014.

[33] G. Castaldi, S. Savoia, V. Galdi, A. Alù, and N. Engheta, "PT metamaterials via complex-coordinate transformation optics," *Phys. Rev. Lett.*, vol. 110, p. 173901, 2013.

[34] C. He, M.-H. Lu, X. Heng, L. Feng, and Y.-F. Chen, "Parity-time electromagnetic diodes in a two-dimensional nonreciprocal photonic crystal," *Phys. Rev. B*, vol. 83, p. 075117, 2011.

[35] A. E. Miroshnichenko, B. A. Malomed, and Y. S. Kivshar, "Nonlinearly PT-symmetric systems: Spontaneous symmetry breaking and transmission resonances," *Phys. Rev. A*, vol. 84, p. 012123, 2011.

[36] S. Longhi, "PT -symmetric laser absorber," *Phys. Rev. A*, vol. 82, p. 031801, 2010.

[37] M. Liertzer, L. Ge, A. Cerjan, A. D. Stone, H. E. Türeci, and S. Rotter, "Pump-induced exceptional points in lasers," *Phys. Rev. Lett.*, vol. 108, p. 173901, 2012.

[38] B. Zhu, R. Lu, and S. Chen, "Interplay between fano resonance and PT symmetry in non-hermitian discrete systems," *Phys. Rev. A*, vol. 91, no. 4, p. 042131, 2015.

[39] *http://camfr.sourceforge.net/.*

[40] N. X. A. Rivolta and B. Maes, "Side-coupled resonators with parity-time symmetry for broadband unidirectional invisibility," *Phys. Rev. A*, vol. 94, no. 5, p. 053854, 2016.

[41] C. Cohen-Tannoudji, B. Diu, and F. Laloë, *Mécanique Quantique*, vol. 1. 1973.

[42] I. Prigogine, *From Being to Becoming: Time and Complexity in the Physical Sciences.* Freeman, 1980.

[43] C. A. Chatzidimitriou-Dreismann, "On the complex-sclaing treatment of ionic transport in fluids," *Phys. Chem.*, vol. 94, pp. 234–242, 1990.

[44] S. A. R. I. Prigogine, *Resonances, instability, and irreversibility.* Wiley, 1997.

[45] N. Moiseyev, *Non-Hermitian Quantum Mechanics.* Cambridge University Press, 2011.

[46] C. M. Bender, "Making sense of non-hermitian hamiltonians," *Reports on Progress in Physics*, vol. 70, no. 6, p. 947, 2007.

[47] B. E. A. Saleh and M. C. Teich, *Fundamentals of Photonics.* Wiley, 2007.

[48] T. Kottos and A. Aceves, "Synthetic structures with parity-time symmetry," in *Contemporary Optoelectronics: Materials, Metamaterials and Device Applications*, pp. 147–162, 2015.

[49] L. He, S. Ozdemir, and L. Yang, "Whispering gallery microcavity lasers," *Laser and Photonics Reviews*, vol. 7, no. 1, pp. 60–82, 2013.

[50] H. Hodaei, M.-A. Miri, M. Heinrich, D. N. Christodoulides, and M. Khajavikhan, "Parity-time-symmetric microring lasers," *Science*, vol. 346, no. 6212, p. 975, 2014.

[51] S. Longhi, D. Gatti, and G. D. Valle, "Robust light transport in non-hermitian photonic lattices," *Scientific Reports*, vol. 5, p. 13376, 2015.

[52] S. Maier, *Plasmonics Fundamentals and Applications.* Springer Science, 2007.

[53] J. D. Jackson, *Classical Electrodynamics.* John Wiley & Sons, Inc., 1999.

[54] A. Zangwill, *Modern Electrodynamics.* Cambridge University Press, 2012.

[55] H. A. Haus, *Waves and Fields in Optoelectronics.* Prentice-Hall, 1984.

[56] S. Fan, W. Suh, and J. D. Joannopoulos, "Temporal coupled-mode theory for the fano resonance in optical resonators," *J. Opt. Soc. Am. A*, vol. 20, no. 3, pp. 569–572, 2003.

[57] B. Luk'yanchuk, N. I. Zheludev, S. A. Maier, N. J. Halas, P. Nordlander, H. Giessen, and C. T. Chong, "The fano resonance in plasmonic nanostructures and metamaterials," *Nature Materials*, vol. 9, no. 9, pp. 707–715, 2010.

[58] Z. Fang, S. Thongrattanasiri, A. Schlather, Z. Liu, L. Ma, Y. Wang, P. M. Ajayan, P. Nordlander, N. J. Halas, and F. J. Garcia de Abajo, "Gated tunability and hybridization of localized plasmons in nanostructured graphene," *ACS Nano*, vol. 7, no. 3, pp. 2388–2395, 2013.

[59] L. Verslegers, Z. Yu, P. B. Catrysse, and S. Fan, "Temporal coupled-mode theory for resonant apertures," *Journal of Optical Society America B*, vol. 27, no. 10, p. 1947, 2010.

[60] P. Bienstman, *Rigorous and efficient modelling of wavelength scale photonic components*. PhD thesis, Ghent University, 2001.

[61] L. Ge, Y. D. Chong, and A. D. Stone, "Conservation relations and anisotropic transmission resonances in one-dimensional $\mathcal{PT}$-symmetric photonic heterostructures," *Phys. Rev. A*, vol. 85, no. 2, p. 023802, 2012.

[62] P. Ambichl, K. G. Makris, L. Ge, Y. D. Chong, A. D. Stone, and S. Rotter, "Breaking of pt symmetry in bounded and unbounded scattering systems," *Phys. Rev. X*, vol. 3, no. 4, p. 041030, 2013.

[63] L. Dal Negro, *Optics of aperiodic structures - fundamentals and device applications*. Pan Stanford, 2013.

[64] B. Maes, *Modeling of nonlinear nanophotonic components based on photonic crystals*. PhD thesis, Ghent University, 2005.

[65] P. Yeh, *Optical waves in layered media*. Wiley, 1988.

[66] J. Joannopoulos, S. Johnson, J. Winn, and R. Meade, *Photonic Crystals: Molding the flow of light*. Princeton University Press, 2008.

[67] T. Clausnitzer, T. Kämpfe, E.-B. Kley, A. Tünnermann, U. Peschel, A. V. Tishchenko, and O. Parriaux, "An intelligible explanation of highly-efficient diffraction in deep dielectric rectangular transmission gratings," *Opt. Express*, vol. 13, no. 26, pp. 10448–10456, 2005.

[68] *http://www.comsol.com/*.

[69] S.-P. Gorza, D. Taillaert, R. Baets, B. Maes, P. Emplit, and M. Haelterman, "Experimental characterization of optical-gap solitons in a one-dimensional photonic crystal made of a corrugated semiconductor planar waveguide," *Phys. Rev. B*, vol. 74, no. 23, p. 235327, 2006.

[70] E. K. Keshmarzi, R. N. Tait, and P. Berini, "Near infrared amplified spontaneous emission in a dye-doped polymeric waveguide for active plasmonic applications," *Opt. Express*, vol. 22, no. 10, pp. 12452–12460, 2014.

[71] A. Kenyon, "Recent developments in rare-earth doped materials for optoelectronics," *Progress in Quantum Electronics*, vol. 26, no. 4-5, pp. 225–284, 2002.

[72] M. Körbl, A. Gröning, H. Schweizer, and J. L. Gentner, "Gain spectra of coupled InGaAsP/InP quantum wells measured with a segmented contact traveling wave device," *Journal of Applied Physics*, vol. 92, no. 5, pp. 2942–2944, 2002.

[73] X. Jiang, Q. Li, and C. M. Soukoulis, "Symmetry between absorption and amplification in disordered media," *Phys. Rev. B*, vol. 59, no. 14, pp. 9007–9010, 1999.

[74] H. Benisty, A. Lupu, and A. Degiron, "Transverse periodic pt symmetry for modal demultiplexing in optical waveguides," *Phys. Rev. A*, vol. 91, no. 5, p. 053825, 2015.

[75] Z. Lin, H. Ramezani, T. Eichelkraut, T. Kottos, H. Cao, and D. N. Christodoulides, "Unidirectional invisibility induced by PT-symmetric periodic structures," *Phys. Rev. Lett.*, vol. 106, p. 213901, 2011.

[76] Y. Huang, G. Veronis, and C. Min, "Unidirectional reflectionless propagation in plasmonic waveguide-cavity systems at exceptional points," *Opt. Express*, vol. 23, no. 23, pp. 29882–29895, 2015.

[77] J. Li, R. Yu, C. Ding, and Y. Wu, "PT-symmetry-induced evolution of sharp asymmetric line shapes and high-sensitivity refractive index sensors in a three-cavity array," *Phys. Rev. A*, vol. 93, no. 2, p. 023814, 2016.

[78] B. Maes, P. Bienstman, and R. Baets, "Switching in coupled nonlinear photonic-crystal resonators," *J. Opt. Soc. Am. B*, vol. 22, no. 8, pp. 1778–1784, 2005.

[79] B. Maes, M. Soljacic, J. D. Joannopoulos, P. Bienstman, R. Baets, S.-P. Gorza, and M. Haelterman, "Switching through symmetry breaking in coupled nonlinear micro-cavities," *Opt. Express*, vol. 14, no. 22, pp. 10678–10683, 2006.

[80] D. G. Rabus, *Ring Resonators: Theory and Modeling.* Springer, 2007.

[81] A. Miroshnichenko, S. Flach, and Y. Kivshar, "Fano resonances in nanoscale structures," *Rev. Mod. Phys.*, vol. 82, no. 3, pp. 2257–2298, 2010.

[82] B. Maes, M. Fiers, and P. Bienstman, "Self-pulsing and chaos in short chains of coupled nonlinear microcavities," *Phys. Rev. A*, vol. 80, no. 3, p. 033805, 2009.

[83] M. Z. Hasan and C. L. Kane, "Colloquium," *Rev. Mod. Phys.*, vol. 82, no. 4, pp. 3045–3067, 2010.

[84] L. Lu, J. D. Joannopoulos, and M. Soljacic, "Topological photonics," *Nat. Phot.*, vol. 8, no. 11, pp. 821–829, 2014.

[85] D. Tanese, E. Gurevich, F. Baboux, T. Jacqmin, A. Lemaitre, E. Galopin, I. Sagnes, A. Amo, J. Bloch, and E. Akkermans, "Fractal energy spectrum of a polariton gas in a fibonacci quasiperiodic potential," *Phys. Rev. Lett.*, vol. 112, no. 14, p. 146404, 2014.

[86] Y. E. Kraus, Y. Lahini, Z. Ringel, M. Verbin, and O. Zilberberg, "Topological states and adiabatic pumping in quasicrystals," *Phys. Rev. Lett.*, vol. 109, p. 106402, 2012.

[87] M. Verbin, O. Zilberberg, Y. E. Kraus, Y. Lahini, and Y. Silberberg, "Observation of topological phase transitions in photonic quasicrystals," *Phys. Rev. Lett.*, vol. 110, no. 7, p. 076403, 2013.

[88] M. Verbin, O. Zilberberg, Y. Lahini, Y. E. Kraus, and Y. Silberberg, "Topological pumping over a photonic fibonacci quasicrystal," *Phys. Rev. B*, vol. 91, no. 6, p. 064201, 2015.

[89] A. Blanco-Redondo, I. Andonegui, M. J. Collins, G. Harari, Y. Lumer, M. C. Rechtsman, B. J. Eggleton, and M. Segev, "Topological optical waveguiding in silicon and the transition between topological and trivial defect states," *Phys. Rev. Lett.*, vol. 116, no. 16, p. 163901, 2016.

[90] L.-J. Lang, X. Cai, and S. Chen, "Edge states and topological phases in one-dimensional optical superlattices," *Phys. Rev. Lett.*, vol. 108, no. 22, p. 220401, 2012.

[91] H. Zhao, S. Longhi, and L. Feng, "Robust light state by quantum phase transition in non-hermitian optical materials," *Scientific Reports*, vol. 5, p. 17022, 2015.

[92] K. Esaki, M. Sato, K. Hasebe, and M. Kohmoto, "Edge states and topological phases in non-hermitian systems," *Phys. Rev. B*, vol. 84, p. 205128, 2011.

[93] A. K. Harter, T. E. Lee, and Y. N. Joglekar, "PT-breaking threshold in spatially asymmetric aubry-andré and harper models: Hidden symmetry and topological states," *Phys. Rev. A*, vol. 93, p. 062101, 2016.

[94] H. Schomerus, "Topologically protected midgap states in complex photonic lattices," *Opt. Lett.*, vol. 38, no. 11, pp. 1912–1914, 2013.

[95] T. E. Lee, "Anomalous edge state in a non-hermitian lattice," *Phys. Rev. Lett.*, vol. 116, p. 133903, 2016.

[96] F. Baboux, E. Levy, A. Lemaitre, C. Gomez, E. Galopin, L. Le Gratiet, I. Sagnes, A. Amo, J. Bloch, and E. Akkermans, "Measuring topological invariants from generalized edge states in polaritonic quasicrystals," *Phys. Rev. B*, vol. 95, no. 16, p. 161114, 2017.

[97] E. Levy, A. Barak, A. Fisher, and E. Akkermans, "Topological properties of fibonacci quasicrystals : A scattering analysis of chern numbers," *arXiv:1509.04028*, 2015.

[98] N. X. A. Rivolta, H. Benisty, and B. Maes, "Topological edge modes with $\mathcal{PT}$ symmetry in a quasiperiodic structure," *Phys. Rev. A*, vol. 96, no. 2, p. 023864, 2017.

[99] X. Fu, Y. Liu, P. Zhou, and W. Sritrakool, "Perfect self-similarity of energy spectra and gap-labeling properties in one-dimensional fibonacci-class quasilattices," *Phys. Rev. B*, vol. 55, no. 5, pp. 2882–2889, 1997.

[100] A. Jazaeri and I. I. Satija, "Localization transition in incommensurate non-hermitian systems," *Phys. Rev. E*, vol. 63, no. 3, p. 036222, 2001.

[101] J. Bellissard, B. Iochum, E. Scoppola, and D. Testard, "Spectral properties of one dimensional quasi-crystals," *Commun. Math. Phys.*, vol. 125, no. 3, pp. 527–543, 1989.

[102] Y. Liu, X. Fu, W. Deng, and S. Wang, "Gap-labeling properties of the energy spectrum for one-dimensional fibonacci quasilattices," *Phys. Rev. B*, vol. 46, no. 14, pp. 9216–9219, 1992.

[103] A. V. Poshakinskiy, A. N. Poddubny, and M. Hafezi, "Phase spectroscopy of topological invariants in photonic crystals," *Phys. Rev. A*, vol. 91, no. 4, p. 043830, 2015.

[104] S. A. Skirlo, L. Lu, Y. Igarashi, Q. Yan, J. Joannopoulos, and M. Soljačić, "Experimental observation of large chern numbers in photonic crystals," *Phys. Rev. Lett.*, vol. 115, no. 25, p. 253901, 2015.